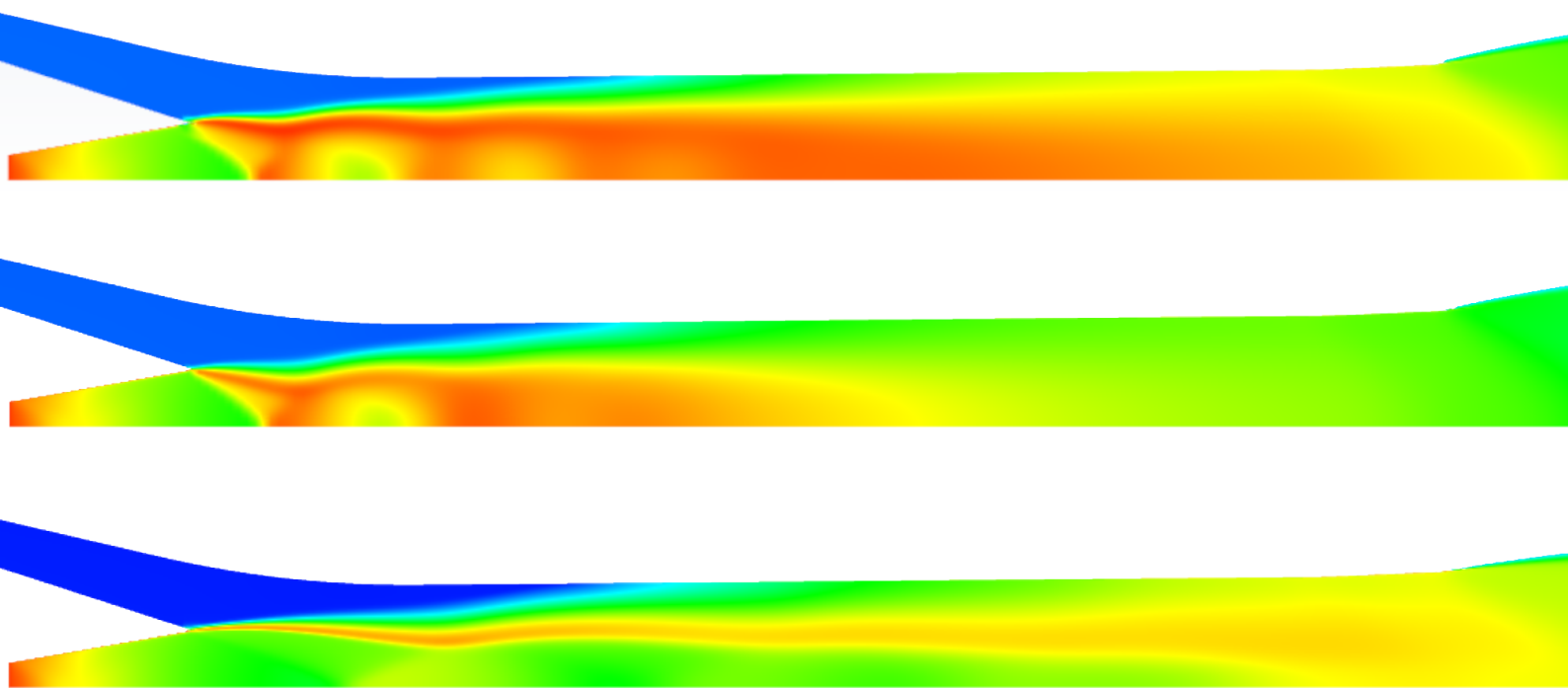


# Preliminary design of a rocket-based combined cycle engine for application aboard Mk-II *Aurora* suborbital spaceplane

Michał Grendysz  
Department of Space Engineering  
Faculty of Aerospace Engineering





# Preliminary design of a rocket-based combined cycle engine for application aboard Mk-II Aurora suborbital spaceplane

by

Michał Grendysz

to obtain the degree of Master of Science  
at the Delft University of Technology,  
to be defended publicly on Wednesday, 8<sup>th</sup> September 2021 at 9:00 AM.

Student number: 5165032  
Project duration: 8<sup>th</sup> December 2020 – 8<sup>th</sup> September 2021  
Thesis committee: A. Cervone TU Delft, chair  
R. Noomen TU Delft, examiner  
B.V.S. Jyoti TU Delft, supervisor  
V.R. Huijsman Dawn Aerospace, supervisor

*This thesis is confidential and cannot be made public until 8<sup>th</sup> September 2023.*

An electronic version of this thesis is available at <http://repository.tudelft.nl/>.



# Preface

*All models are wrong, but some are useful*

George E. P. Box

The following thesis is the result of the modelling and designing effort done in collaboration with Dawn Aerospace. It was a part of large-scale activities, which in the future will lead to achieving the goal of sustainable and inexpensive space launches.

I would like to express my gratitude to all people who have helped me finish this work. Firstly, I want to thank my girlfriend, my parents and my sister, who have all helped me keep my sanity through the long months of struggle during lockdowns caused by the pandemic. Secondly, my supervisors, Ralph and Jyoti, who have frequently advised me about how to solve the encountered problems and guided me through the process. Finally, all the people without whom I would not ever get interested in space engineering, especially the Almukantarat Astronomy Club that introduced me to astronomy and astronautics.

Michał Grendysz  
Delft, August 2021



# Abstract

The rocket-based combined cycle (RBCC) engines are a hybrid between rocket and air-breathing propulsion. They can offer performance gains when compared to traditional rocket engines. At the same time, they are relatively simple in design. Therefore, they generally do not require long development times or large funds so they could be an attractive alternative to rocket-only propulsion.

This thesis presents research on RBCC engines with the main goal to investigate possible use of this type of engine aboard the Mk-II *Aurora* suborbital spaceplane that is being developed by Dawn Aerospace. The main criterion used in the assessment was the impact of implementing the engine on spaceplane's performance compared to current rocket-only propulsion.

In this study a RBCC engine was designed based around the parameters of the core rocket motor. During the initial phase, the engine was optimized for performance using a developed and validated quasi-1D model. This design was then analysed using CFD methods to verify results of the early simulation. Later on the quasi-1D model was used to simulate engine operation in multiple flight conditions. Finally, the trajectory was optimised and compared with the trajectory of a rocket-propelled spaceplane to investigate the final performance gains. It was concluded that only a modified version with added compressor could possibly match or outperform rocket-only propulsion but only if its design does not add more than the threshold mass and drag to the existing spaceplane design.



# Contents

<b>1</b>	<b>Introduction</b>	<b>1</b>
1.1	Background information . . . . .	1
1.2	Literature review in the field of RBCC engines . . . . .	3
1.2.1	History of research . . . . .	3
1.2.2	Current understanding of RBCC engine's operation . . . . .	4
1.2.3	Expected RBCC performance . . . . .	4
1.3	Problem definition . . . . .	5
1.3.1	Research objective . . . . .	5
1.3.2	Research questions . . . . .	5
1.4	Methodology and report layout . . . . .	6
<b>2</b>	<b>Quasi-1D model of an RBCC engine</b>	<b>7</b>
2.1	Validation model description . . . . .	7
2.1.1	Nomenclature and assumptions . . . . .	8
2.1.2	Chemical equilibrium calculations. . . . .	9
2.1.3	Flow equations for the afterburner . . . . .	10
2.2	Validation model results . . . . .	13
2.2.1	Combustion efficiency function . . . . .	14
2.2.2	Total temperature predictions comparison . . . . .	16
2.2.3	Total pressure comparison. . . . .	16
2.3	Development model description. . . . .	18
2.3.1	Overall simulation logic . . . . .	19
2.3.2	Inlet calculations . . . . .	20
2.3.3	Chemical equilibrium calculations. . . . .	21
2.3.4	Nozzle calculations . . . . .	23
2.4	Development model results . . . . .	24
2.4.1	Afterburner size and core rocket nozzle expansion ratio . . . . .	24
2.4.2	Inlet size . . . . .	26
2.4.3	Final design results. . . . .	27
2.4.4	Shielded Primary Injection results. . . . .	29
<b>3</b>	<b>CFD model of a chosen design</b>	<b>31</b>
3.1	Combustion model . . . . .	31
3.1.1	Chosen model description . . . . .	31
3.1.2	Test runs setup . . . . .	31
3.1.3	Test runs results . . . . .	33
3.2	Geometry and mesh . . . . .	37
3.3	Simulated cases matrix. . . . .	39
3.4	Results . . . . .	40
3.4.1	Take-off conditions. . . . .	40
3.4.2	Afterburner temperature distribution . . . . .	41
3.4.3	Inlet behaviour . . . . .	42
3.4.4	Shielded Primary Injection. . . . .	44
3.4.5	Comparison with quasi-1D model . . . . .	45
3.4.6	Conclusion . . . . .	49

---

<b>4</b>	<b>Trajectory optimisation</b>	<b>51</b>
4.1	Assumptions and implementation . . . . .	51
4.1.1	Trajectory profile . . . . .	51
4.1.2	Climb phase. . . . .	52
4.1.3	Pitch-up manoeuvre . . . . .	53
4.1.4	Coast phase . . . . .	54
4.1.5	Propulsion look-up table. . . . .	54
4.2	Results . . . . .	55
4.2.1	Trajectory. . . . .	55
4.2.2	Specific impulse . . . . .	56
<b>5</b>	<b>Alternative RBCC design</b>	<b>59</b>
5.1	Design selection . . . . .	59
5.2	Alternative design performance . . . . .	60
5.3	Drag and mass estimation . . . . .	61
5.4	Trajectory results . . . . .	63
5.4.1	Trajectory. . . . .	63
5.4.2	Specific impulse . . . . .	64
<b>6</b>	<b>Conclusions</b>	<b>67</b>
6.1	Quasi-1D model. . . . .	67
6.2	Final RBCC configuration . . . . .	67
6.2.1	Design parameters . . . . .	67
6.2.2	Inlet and compressor assembly design . . . . .	68
6.2.3	Shielded Primary Injection. . . . .	68
6.3	RBCC implementation influence on Mk-II <i>Aurora</i> . . . . .	68
6.4	Recommended future work . . . . .	69

# List of Figures

1.1	Comparison of size: visible 2 <sup>nd</sup> and 3 <sup>rd</sup> (planned) generation of the Dawn Aerospace's spaceplane . . . . .	2
1.2	Mission profile of Mk-II <i>Aurora</i> suborbital spaceplane . . . . .	2
1.3	General layout of an RBCC engine utilizing the simultaneous mixing and combustion principle . . . . .	3
1.4	Plots of approximate specific impulse against free stream Mach number of different propulsion cycles . . . . .	5
2.1	Schematic of the experimental setup used by Masuya et al. [15] . . . . .	7
2.2	Plot of static and total air pressure against oxidizer to fuel ratio of the core rocket for the validation case . . . . .	8
2.3	General schematic of an RBCC engine with used annotations of sections . . . . .	9
2.4	Plot of experimental data of wall pressure along the afterburner axis from Masuya et al. [15] for different afterburner lengths compared with approximations used in the model . . . . .	11
2.5	Illustration of the Rayleigh flow equations implementation in the afterburner simulation . . . . .	13
2.6	Combustion efficiency function plotted against $\frac{L}{a_5}$ for different oxidizer-fuel ratios of the core rocket engine . . . . .	15
2.7	Combustion efficiency function plotted against oxidizer-fuel ratio of the core rocket engine for $\frac{L}{a_5} = 10.4$ . . . . .	15
2.8	Plot of total temperature at the afterburner exit against the oxidizer-fuel ratio of the core rocket engine . . . . .	16
2.9	Plot of total pressure at the afterburner exit against the oxidizer-fuel ratio of the core rocket engine for the 1040 mm long afterburner . . . . .	17
2.10	Plot of total pressure at the afterburner exit against the afterburner length . . . . .	17
2.11	Plot of parameters of the Mk-II <i>Aurora</i> rocket engine exhaust relative to design operation against oxidizer to fuel ratio, calculated using Rocket Propulsion Analysis program [21] . . . . .	18
2.12	Block diagram of the development model implementation . . . . .	19
2.13	Inlet pressure recovery as presented by Olds and Bradford [18] . . . . .	21
2.14	Plot of natural logarithm of carbon dioxide equilibrium constant against temperature . . . . .	22
2.15	Plot of specific impulse multiplier (compared to rocket-only propulsion) against expansion ratio of the core rocket nozzle for different afterburner diameters at static sea level conditions . . . . .	24
2.16	Plot of specific impulse multiplier (compared to rocket-only propulsion) against Mach number of the free stream for different expansion ratios of the core rocket nozzle at sea level conditions . . . . .	25
2.17	Plot of specific impulse multiplier (compared to rocket-only propulsion) against inlet frontal area for different free stream Mach numbers at sea level conditions . . . . .	26
2.18	Plot of specific impulse multiplier (compared to rocket-only propulsion) against inlet frontal area for different free stream Mach numbers and oxidizer-fuel ratios of the core rocket at 5 km altitude . . . . .	27
2.19	Plot of specific impulse multiplier (compared to rocket-only propulsion) against Mach number of the free stream for different altitudes with the core rocket operating at $\frac{O}{F} = 6.5$ . . . . .	28
2.20	Plot of specific impulse multiplier (compared to rocket-only propulsion) against Mach number of the free stream for different altitudes with the core rocket operating at $\frac{O}{F} = 4.5$ . . . . .	28
2.21	Plot of specific impulse multiplier (compared to rocket-only propulsion) against mass flow rate of additional fuel injected in the afterburner at sea level conditions for different free stream Mach numbers . . . . .	29

2.22	Plot of specific impulse multiplier (compared to rocket-only propulsion) against mass flow rate of additional fuel injected in the afterburner at 5 km of altitude for different free stream Mach numbers and oxidizer to fuel ratios of the core rocket . . . . .	30
2.23	Plot of specific impulse multiplier (compared to rocket-only propulsion) against mass flow rate of additional fuel injected in the afterburner at 10 km of altitude for different free stream Mach numbers and oxidizer to fuel ratios of the core rocket . . . . .	30
3.1	Detailed view of the nozzle in the mesh used for test runs of the combustion model . . . . .	31
3.2	Overall view of the mesh used for test runs of the combustion model . . . . .	32
3.3	Plot of value of $Y^+$ on the nozzle wall against position along the axis for an exemplary rocket-only case . . . . .	33
3.4	Bar graph of relative differences between nozzle exit parameters calculated by Rocket Propulsion Analysis Program [21] and by CFD test run for oxidizer to fuel ratio of 6.5 . . . . .	33
3.5	Bar graph of relative differences between nozzle exit parameters calculated by Rocket Propulsion Analysis Program [21] and by CFD test run for oxidizer to fuel ratio of 4.5 . . . . .	34
3.6	Mach number contours of the rocket-only case with $\frac{O}{F} = 6.5$ . . . . .	34
3.7	Mach number contours of the rocket-only case with $\frac{O}{F} = 4.5$ . . . . .	35
3.8	Molecular hydrogen mass fraction contours of the rocket-only case with $\frac{O}{F} = 6.5$ . . . . .	35
3.9	Molecular hydrogen mass fraction contours of the rocket-only case with $\frac{O}{F} = 4.5$ . . . . .	36
3.10	Static temperature contours of the rocket-only case with $\frac{O}{F} = 6.5$ . . . . .	36
3.11	Static temperature contours of the rocket-only case with $\frac{O}{F} = 4.5$ . . . . .	36
3.12	Mesh used for simulating RBCC cases . . . . .	37
3.13	Zoomed-in view of the geometry used for simulating RBCC cases . . . . .	37
3.14	Mesh used for simulating RBCC cases — detailed view of the inlet . . . . .	38
3.15	Mesh used for simulating RBCC cases — detailed view of the mixing point . . . . .	38
3.16	Mesh used for simulating RBCC cases — detailed view of the RBCC nozzle . . . . .	38
3.17	Plot of value of $Y^+$ on the RBCC engine's walls against position along the axis for an exemplary case . . . . .	39
3.18	Control surfaces used for convergence checks . . . . .	40
3.19	Mach number contours for static sea level conditions . . . . .	41
3.20	Molecular hydrogen mass fraction contours for static sea level conditions . . . . .	41
3.21	Static temperature contours for static sea level conditions . . . . .	42
3.22	Static temperature contours for $M_\infty = 1.6$ and altitude of 5 km . . . . .	42
3.23	Static temperature contours for $M_\infty = 2.4$ and altitude of 5 km . . . . .	42
3.24	Inlet Mach number contours for $M_\infty = 2.4$ and altitude of 5 km . . . . .	43
3.25	Inlet Mach number contours for $M_\infty = 2.4$ and altitude of 5 km with shielded primary injection active . . . . .	43
3.26	Inlet Mach number contours for $M_\infty = 0.8$ and altitude of 5 km . . . . .	43
3.27	Inlet Mach number contours for $M_\infty = 1.6$ and altitude of 5 km . . . . .	44
3.28	Molecular hydrogen mass fraction contours for $M_\infty = 2.4$ and altitude of 5 km with shielded primary injection active . . . . .	44
3.29	Static temperature contours for $M_\infty = 2.4$ and altitude of 5 km with shielded primary injection active . . . . .	45
3.30	Bar graph of relative errors in estimation of afterburner exit total temperature by the quasi-1D model . . . . .	46
3.31	Bar graph of relative errors in estimation of afterburner exit total pressure by the quasi-1D model . . . . .	46
3.32	Bar graph of relative errors in estimation of thrust and specific impulse by the quasi-1D model . . . . .	47
3.33	Plot of thrust multiplier (compared to rocket-only propulsion) against free stream Mach number at 5 km of altitude for different models and oxidizer to fuel ratios of the core rocket . . . . .	48
3.34	Plot of specific impulse multiplier (compared to rocket-only propulsion) against free stream Mach number at 5 km of altitude for different models and oxidizer to fuel ratios of the core rocket . . . . .	48

---

4.1	General trajectory considered in the trajectory optimiser . . . . .	52
4.2	Forces acting on the spaceplane during the climb phase . . . . .	52
4.3	Forces acting on the spaceplane during the pitch-up manoeuvre . . . . .	53
4.4	Forces acting on the spaceplane during the coast phase . . . . .	54
4.5	Plot of a look-up table of maximal specific impulse multiplier (compared to rocket-only propulsion) against atmospheric pressure for different free stream Mach numbers . . . . .	55
4.6	Atmospheric part of the optimal trajectories for rocket-only and RBCC propulsion (dots represent the burnout point) . . . . .	56
4.7	Plot of specific impulse against altitude along the optimal trajectories for rocket-only and RBCC propulsion . . . . .	57
4.8	Plot of specific impulse against airspeed along the optimal trajectories for rocket-only and RBCC propulsion . . . . .	57
5.1	Plot of specific impulse multiplier (compared to rocket-only propulsion) against expansion ratio of the core rocket nozzle for different afterburner sizes and oxidizer to fuel ratios . . . . .	60
5.2	Plot of a look-up table of maximal specific impulse multiplier (compared to rocket-only propulsion) against atmospheric pressure for different free stream Mach numbers — RBCC with a compressor . . . . .	61
5.3	Atmospheric part of the optimal trajectories for rocket-only and RBCC propulsion with compressor (dots represent the burnout point) . . . . .	63
5.4	Plot of specific impulse against altitude along the optimal trajectories for rocket-only and RBCC propulsion with compressor . . . . .	64
5.5	Plot of specific impulse against airspeed along the optimal trajectories for rocket-only and RBCC propulsion with compressor . . . . .	65



# List of Tables

2.1	Parameters of the core rocket engine exhaust calculated using Rocket Propulsion Analysis program . . . . .	8
2.2	Correlation coefficients of experimental data on wall pressure distribution in the afterburner from Masuya et al. [15] and approximation used in the model . . . . .	12
2.3	Parameters of the final RBCC design . . . . .	27
3.1	Case matrix for the CFD model . . . . .	40
3.2	List of cases with numbering . . . . .	45
5.1	Parameters of the RBCC design with compressor . . . . .	60
5.2	Mass and drag increase for different considered cases . . . . .	63
6.1	Parameters of the RBCC design with compressor . . . . .	68



# List of Symbols and Abbreviations

## Symbols

$\alpha$	bypass ratio of the RBCC engine
$\gamma$	isentropic exponent
$\Delta A_{wet}$	added wetted area
$\Delta C_D$	increase in drag coefficient
$\Delta H^0$	difference in enthalpy compared to the reference state
$\Delta S^0$	difference in entropy compared to the reference state
$\eta_c$	combustion efficiency
$\eta_n$	nozzle efficiency
$\theta$	climb angle
$\rho$	density
$\sigma_y$	yield strength
$A$	cross-section area
$a$	local speed of sound
$a^*$	critical sonic velocity
$c^*$	characteristic velocity
$C_p$	constant pressure specific heat
$d$	diameter of the cross-section
$\vec{D}$	drag force
$\vec{F}_g$	gravity force
$g_0$	standard acceleration due to gravity
$h$	molar enthalpy of species/altitude of the vehicle
$h_f$	heat of formation of species
$I_{sp}$	specific impulse
$K_p$	equilibrium constant
$L$	length of the afterburner
$\vec{L}$	lift force
$M$	Mach number
$m$	mass
$\dot{m}$	mass flow rate
$n$	molar flow rate of species
$\frac{O}{F}$	oxidizer to fuel ratio
$p$	pressure
$R$	specific gas constant
$T$	temperature
$t$	time/thickness
$\vec{T}$	thrust
$v$	velocity
$W$	molar mass of species
$x$	position along the axis of the afterburner
$Y$	mass fraction of species

## Subscripts

0	total (stagnation) parameter of the flow
$\infty$	free stream parameter
<i>air</i>	inlet air parameter
<i>des</i>	design parameter
<i>r</i>	rocket exhaust parameter
<i>ref</i>	reference parameter

**Abbreviations**

CFD	computational fluid dynamics
COTS	commercial off-the-shelf
e.g.	<i>exempli gratia</i> (for example)
etc.	<i>et cetera</i> (and the rest)
R&D	research and development
RBCC	rocket-based combined cycle
RPA	Rocket Propulsion Analysis
SMC	simultaneous mixing and combustion
SPI	shielded primary injection

# Introduction

The following thesis is the result of the modelling and designing process that has been conducted in cooperation with Dawn Aerospace. This research is a part of larger-scale R&D activities that are carried out in order to develop an innovative space launcher. Next sections describe background of the research, as well as provide context of the existing literature, define the problem and introduce how the research was conducted.

## 1.1. Background information

Ever since the first space flights, cost and preparation time of the space launch were the main constraints for the industry. Currently, most space hardware is designed in a way to ensure its reliability while time constraints are less important leading to very long technology advancement times in this field. This is starting to change due to the decreasing cost per kilogram to orbit, as stated by Jones [13]. However, while this trend confirms that the costs of space launch can be cut by other means, all current launch vehicles still have very small payload mass fractions as they utilize all-rocket propulsion and a typical vertically launched configuration. Additionally, they are subject to a lot of operational constraints, such as the need of closing large sections of airspace during launch. Therefore, only the entirely new approach will allow for a true breakthrough.

Flaherty et al. [10] claimed that such a breakthrough can be achieved by applying airbreathing propulsion to a horizontally launched vehicle. This configuration is supposed to not only offer much lower propellant mass fractions (as low as 65% compared to circa 90% for all-rocket propulsion, according to Escher et al. [8]) but also allow for a flexible aircraft-like operation. This idea is not new and has been considered for example by Siebenhaar and Bulman [24], however, to this day none of those concepts managed to actually reach operational readiness.

A reusable horizontal take-off, horizontal landing launch vehicle is currently being developed by Dawn Aerospace, which is based in the Netherlands and New Zealand. Its mission is to bring down costs of space launch by means of flexible and frequent flights. The design of a suborbital spaceplane Mk-II *Aurora* is a step in this process. This reflects the overall philosophy of the company, which is to make small steps at the time by setting ambitious but realistic goals.

The current design of Mk-II *Aurora* considers an all-rocket single-stage suborbital spaceplane (as presented in figure 1.1). The mission profile of this vehicle is presented in figure 1.2. The task executed during such a mission is to reach space and provide valuable microgravity time. The main advantage compared to typical sounding rockets is the return to launch site characteristic, allowing for reduction of operational activities (as the vehicle does not need to be retrieved), easy merging with air traffic and being ready to launch again after only refuelling. All those features could make space flight similar to air travel, which currently is a day-to-day activity.

Despite all those innovative characteristics, the propulsion system of Mk-II *Aurora* is still very traditional, yielding low technical risks and a short development time but also limited performance (specific impulse at sea level of around 240 s). That is why a switch to air-breathing propulsion is a promising concept, which could add even more operational advantages for the designed spaceplane.

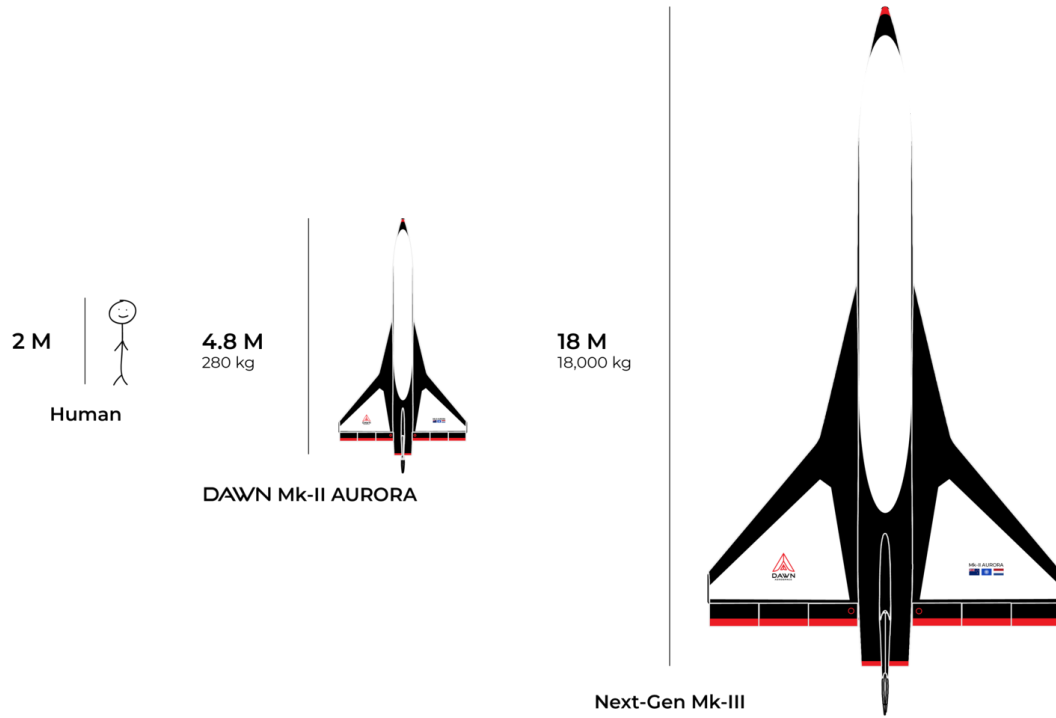


Figure 1.1: Comparison of size: visible 2<sup>nd</sup> and 3<sup>rd</sup> (planned) generation of the Dawn Aerospace’s spaceplane, [6]

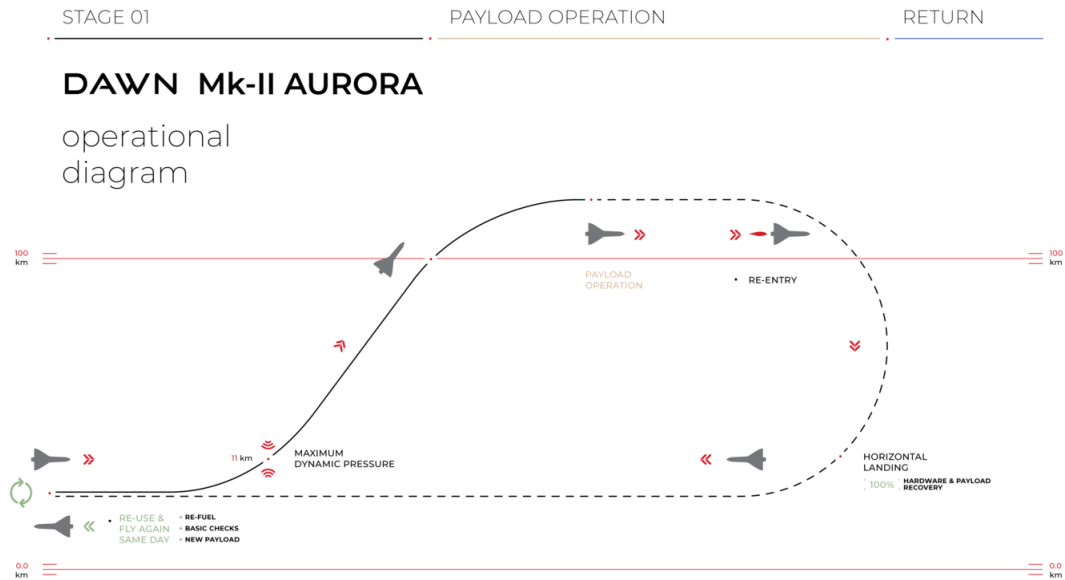


Figure 1.2: Mission profile of Mk-II Aurora suborbital spaceplane, [6]

## 1.2. Literature review in the field of RBCC engines

Out of many options for air-breathing propulsion, the rocket-based combined cycle (RBCC) concept was found to be the most promising. The general layout of an RBCC engine is presented in figure 1.3. The main idea, as presented by Daines and Segal [5], is to use the atmospheric air as oxidizer in the secondary combustor, which is located downstream of the core rocket engine's nozzle. In such a configuration, the amount of development time needed might be cut significantly because the current Mk-II *Aurora* propulsion can be used as a core rocket engine.

Based on the conducted literature study and considering the requirements set up by Dawn Aerospace, design space has been reduced to only include the simultaneous mixing and combustion (SMC) afterburning scheme. It means that the fuel for the secondary combustor is to be supplied by the plume of the core rocket engine and no fuel injectors are present downstream from its nozzle.

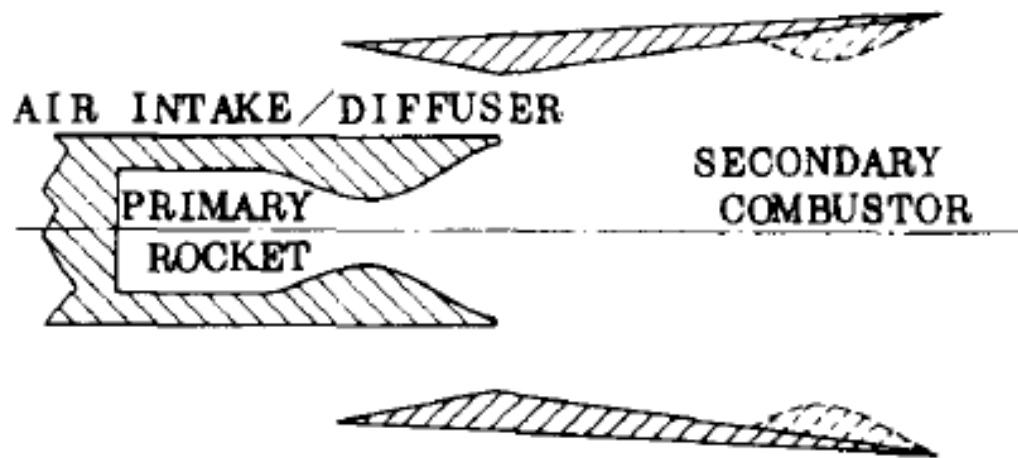


Figure 1.3: General layout of an RBCC engine utilizing the simultaneous mixing and combustion principle, [15]

One of the greatest advantages of RBCC engines, which lead to choosing this configuration, is that they can operate in practically all airspeed regimes — from subsonic to supersonic or even hypersonic, as well as at all altitudes, including vacuum of space. In all of those conditions, according to literature such as the paper by Daines and Segal [5], the system should be able to provide some level of augmentation to the core rocket thrust, just at different levels. Therefore, it can raise the average  $I_{sp}$  of the propulsion system thus increasing  $\Delta v$  of the vehicle. This, in turn, can be traded for larger payload mass, higher apogee of the trajectory or downscaling the whole vehicle.

### 1.2.1. History of research

According to Etele et al. [9], the first concepts of air entrainment into rocket engines (similar to RBCC) are dated back to 1940s and a figure of Theodore von Kármán. This shows that even in the days when rocket technology was still maturing, many people were aware of its shortcomings when it comes to atmospheric flight. However, as pointed out by Shi et al. [23], it wasn't until 1960s when air augmentation became a topic of more thorough research. Some stagnation was observed after this initial period probably due to RBCC being only a favourable propulsion system for space launchers and not for aircraft. Additionally, adopting this concept required radical changes in trajectory design and general operations with net gains (performance minus additional mass and drag) still uncertain.

Stagnation remained until 1990s and 2000s when the second wave of interest in RBCC engines sparked, this time also in other countries such as China and Japan. This progress continues now and with the current boom of space launches more and more papers are published lately.

### 1.2.2. Current understanding of RBCC engine's operation

A comprehensive overview of RBCC engines is presented by Daines and Segal [5]. In this paper they are described as airbreathing engines that have a rocket engine in their core. The main mechanism of augmentation during atmospheric part of the flight in such an engine is afterburning in a combustor behind rocket engine's nozzle using atmospheric air, which enters the engine in what is called a secondary stream in contrast to the primary rocket stream. Due to that, the augmentation system is relatively simple with no moving parts and almost completely separate from the core rocket engine, except for coupled control of the main combustion chamber and the afterburner.

RBCC engines can operate in different modes, which, as presented by Yang et al. [31] and Xue et al. [30], are divided according to the Mach number of the free air stream. The engine may be controlled in a way to switch the mode at the certain Mach number instantaneously or the switch can occur naturally over the range of Mach numbers (a hybrid approach is also possible).

Typically, the first mode of operation of the RBCC engine is the rocket-ejector, which is a mode of operation associated with Mach numbers 0–2 or 0–3 (according to Daines and Segal [5]). In this mode the core rocket engine is the main source of thrust and the secondary combustion is limited.

When the ram effect of the incoming air is sufficient to compress it significantly, typically between Mach numbers 2–3 according to Daines and Segal [5], the engine can enter the ramjet or rocket-ramjet mode. It means that the afterburner is the main source of thrust and the primary rocket is either completely shut down (in the pure ramjet mode) or being throttled down serves as a flameholder (in the rocket-ramjet mode), according to Xue et al. [30]. The flameholding role of the rocket plume is at the cost of specific impulse but provided additional heat ensures no blown off of the flame can occur and therefore increases reliability.

When the vehicle reaches the hypersonic regime (Mach 5–7, according to Daines and Segal [5]), a switch to scramjet or rocket-scramjet mode can happen. As a consequence, the flow in the afterburner will be supersonic and so will be the combustion itself. This mode is of little interest to the study though as Mk-II *Aurora* does not reach hypersonic speeds.

Once the air density drops below threshold for effective scramjet or ramjet operation, the RBCC engine can continue working in the rocket-only mode. According to Daines and Segal [5], even in this mode the afterburner can prove useful if designed correctly as the additional afterburner nozzle increases area ratio preventing or reducing typical effect of underexpansion in the upper atmosphere. However, what should be kept in mind is that such a nozzle will never be as effective as a dedicated bell nozzle with the same area ratio.

### 1.2.3. Expected RBCC performance

It is worth to mention the order of magnitude of performance gains compared to traditional rocket engines. Some initial conclusions could be drawn from direct specific impulses comparison of propulsion cycles used in RBCC engines. This is presented in figure 1.4. The plot generalises specific impulses of engines in 2 groups — one that uses hydrogen as fuel and the other that uses hydrocarbons with the first one having better performance in all cycles. For the Mk-II *Aurora* case change of propellant was out of question so focus should be on the hydrocarbon part of the plot.

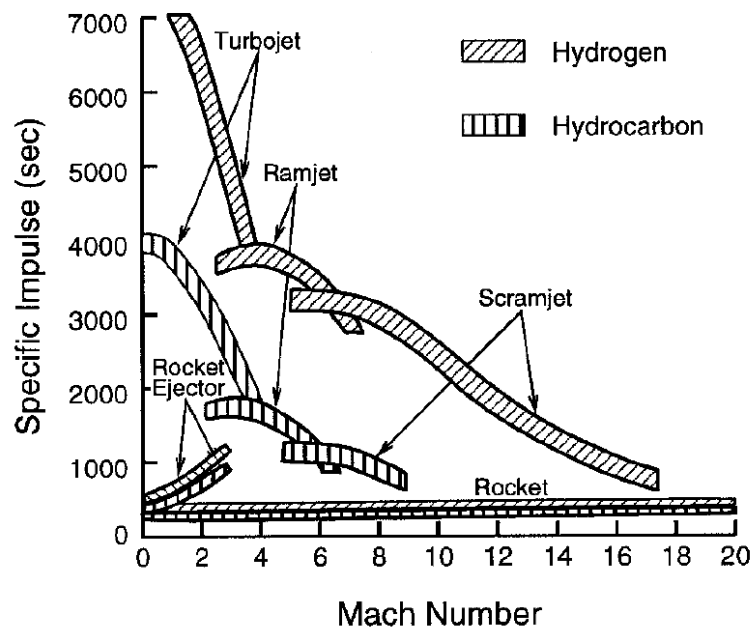


Figure 1.4: Plots of approximate specific impulse against free stream Mach number of different propulsion cycles, [5]

Performance gains from employing the RBCC concept on a spaceplane are clearly visible. This is the evidence which led to the conclusion that if the afterburner does not add a lot of drag and mass, the overall gain of  $\Delta v$  would be substantial (with take-off mass staying the same).

### 1.3. Problem definition

With the provided information from literature and background details about the Mk-II *Aurora* project, it is clear that the RBCC engine could be a good fit for the new version of the vehicle. However, further investigation had to be conducted to confirm this, therefore the following research objective and research questions were formulated.

#### 1.3.1. Research objective

“To provide a preliminary design of a RBCC engine utilizing the SMC principle for Mk-II *Aurora* in order to better the vehicle’s performance by means of predicting the engine’s operation and characteristics through analytical and numerical analysis”.

#### 1.3.2. Research questions

”How will the implementation of the RBCC concept utilizing the SMC principle to the new design of the propulsion system of Mk-II *Aurora* influence the vehicle’s performance?”

The following sub-questions needed to be answered in order to answer this main question:

1. How can the RBCC engine utilizing the SMC principle be designed in order to provide effective thrust augmentation across operational flight Mach numbers and altitudes?
  - 1.1. What are the general dimensions and shape of the secondary combustor that allow for effective operation?
  - 1.2. What are the basic parameters of the inlet and the nozzle for this combustor?
  - 1.3. Is variable geometry required for any part of the engine?
  - 1.4. Can the shielded primary injection (SPI) concept be successfully implemented?
  - 1.5. What is the influence of using the SPI concept on the engine operation (efficiency and operability)?

2. How will the designed RBCC engine, once integrated on the Mk-II *Aurora*, increase the vehicle's  $\Delta v$ ?
  - 2.1. What is the actual achievable range of thrust and specific impulse (as a function of Mach number and altitude)?
  - 2.2. What is the expected mass and drag increase of Mk-II *Aurora* with the RBCC engine?

## 1.4. Methodology and report layout

The given research objective was achieved by means of systematic and thorough analysis of design options using methods adequate to early stages of the design. Firstly, a quasi-1D model of an RBCC engine was developed to understand the relevant parameters, as well as to choose the most promising configuration for further analysis. This process is described in chapter 2.

The chosen design was then further analysed using CFD models in order to verify the results obtained earlier. Those simulations also allowed for the assessment of the chosen design in greater detail at different flight conditions. The entire methodology and results of this stage of the research is presented in chapter 3.

Lastly, a detailed analysis of how the RBCC engine would influence the vehicle's performance was conducted. This stage included optimising the trajectory for both rocket-only and RBCC propulsion and comparison of achieved apogees. Chapter 4 presents the process and results in detail.

As an addition, chapter 5 describes an alternative RBCC engine configuration, which, according to conducted analysis, should yield better performance than the initially chosen design.

## Quasi-1D model of an RBCC engine

The following sections present the assumptions, used methods and results of a quasi-1D RBCC engine model. It was created to evaluate different potential designs and choose cases for the CFD verification.

### 2.1. Validation model description

Development of this quasi-1D model was started by simulating cases studied experimentally by Masuya et al. [15]. The setup used in this research is presented in figure 2.1. As visible, it is a simple RBCC combustor utilizing the SMC principle.

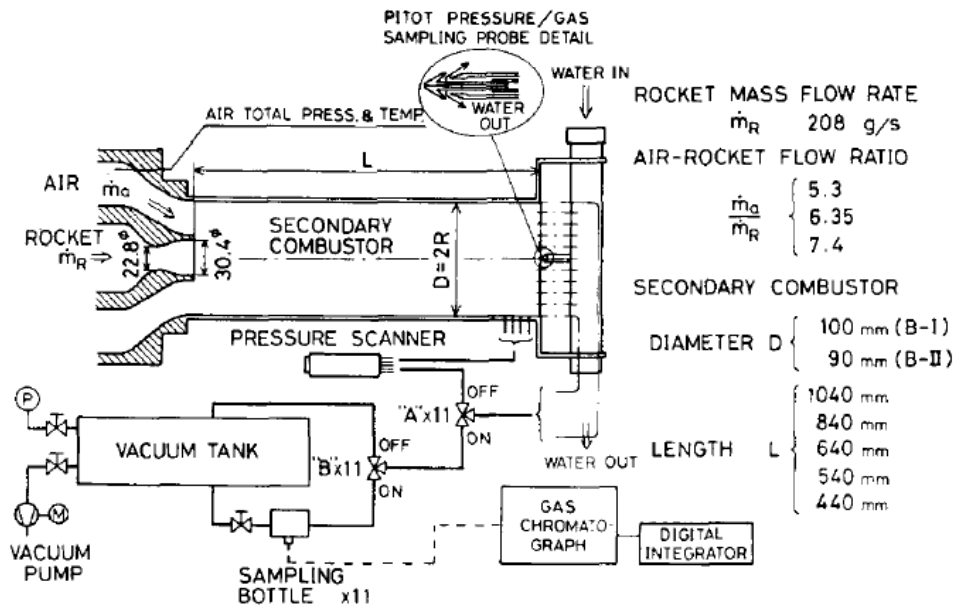


Figure 2.1: Schematic of the experimental setup used by Masuya et al. [15]

The study by Masuya et al. [15] was focused on predicting and measuring pressure at the end of the combustor, where the flow should be choked. This was ensured by adjusting inlet air parameters to the changing oxidizer to fuel ratio of the core rocket. For the purpose of the simulation, those parameters were read from the plot provided in the paper and used as input data. The static and total pressure of the inlet air is plotted in figure 2.2. It is also mentioned in the study that air was supplied from the pressurised tank that was stored in room temperature. Therefore, 295.15 K was taken as total temperature of the inlet air ( $T_{0air}$ ). This assumes that the effect of tank cooling during its discharge was negligible due to short durations of test firings.

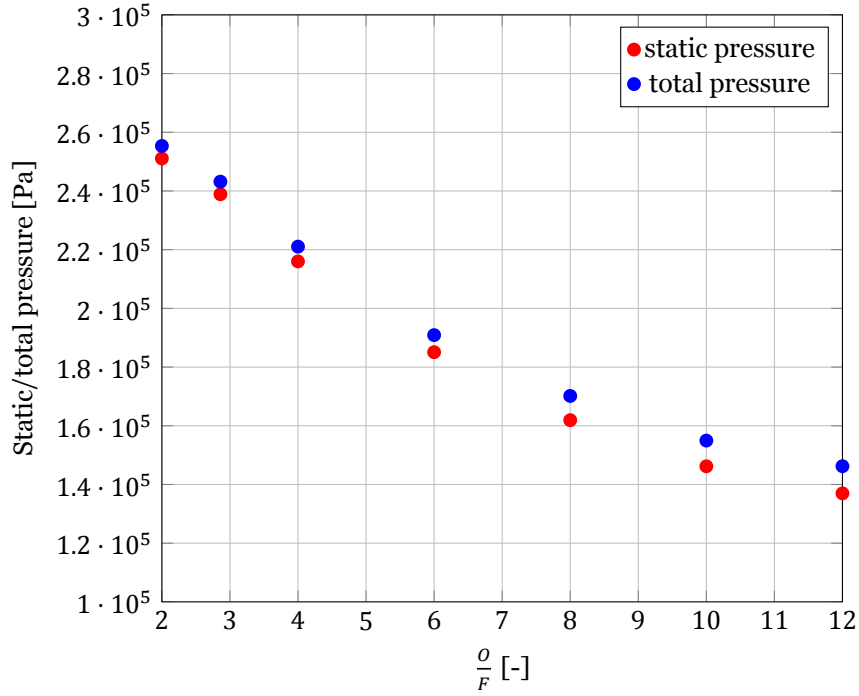


Figure 2.2: Plot of static and total air pressure against oxidizer to fuel ratio of the core rocket for the validation case

The core rocket engine of the RBCC combustor from the study by Masuya et al. [15] used a hydrogen-oxygen mixture as propellant with different oxidizer to fuel ratios. Mass flow rate, however, stayed constant regardless of those changes. Knowing that and the dimensions of the nozzle, it was possible to simulate operation of this rocket engine using Rocket Propulsion Analysis program [21] and use the results as input data for the simulation. They are presented in table 2.1.

Table 2.1: Parameters of the core rocket engine exhaust calculated using Rocket Propulsion Analysis program [21]

$\frac{O}{F}$ [-]	Total temperature $T_{0r}$ [K]	Total pressure $p_{0r}$ [bar]	Isentropic exponent $\gamma_r$ [-]	Constant pressure specific heat $C_{pr}$ [ $\frac{J}{kgK}$ ]	Nozzle exit Mach number $M_{2r}$ [-]
2	1797.4	11.5	1.328	5567	2.00
4	2874.8	12.0	1.222	4341	1.93
6	3273.2	11.2	1.132	3632	1.90
8	3329.7	10.3	1.113	3119	1.90
10	3273.5	10.2	1.116	2764	1.90
12	3187.0	9.1	1.122	2510	1.90

### 2.1.1. Nomenclature and assumptions

The method used for simulating RBCC engine operation can be classified as quasi-1D, as mentioned before. This means that at any given section flow parameters (velocity, pressure, temperature etc.) are assumed to be uniform but they can change throughout the engine along with the area of the cross-section. Appropriate equations were used to model how flow parameters are changing between different sections.

Summary of other assumptions made in the following sections is provided below:

- all gases considered behave according to the ideal gas law,
- constant pressure specific heat and standard enthalpy of different gases can be accurately calculated using polynomials from the *NIST Chemistry WebBook* [17],

- constant pressure specific heat per unit mass of the gas mixture can be calculated as a mass-weighted average of specific heat of its components,
- flow in the afterburner reaches chemical equilibrium after mixing,
- only water vapour, molecular oxygen and molecular hydrogen take part in the reaction in the afterburner,
- mass, momentum and energy of the flow is preserved in the afterburner — no heat losses or wall friction is taken into account.

Figure 2.3 shows the overall schematic of an RBCC engine with annotations of important sections that were used in the simulation. The same notations are used throughout all chapters. In order, those cross-sections are: 1 — inlet, 2 — inlet throat, 3 — throat of the core rocket engine, 4 — beginning of the afterburner (to avoid ambiguity, 4 will be used for air parameters and 4r for rocket exhaust parameters in this section), 5 — the end of the afterburner, 6 — RBCC engine nozzle exit.

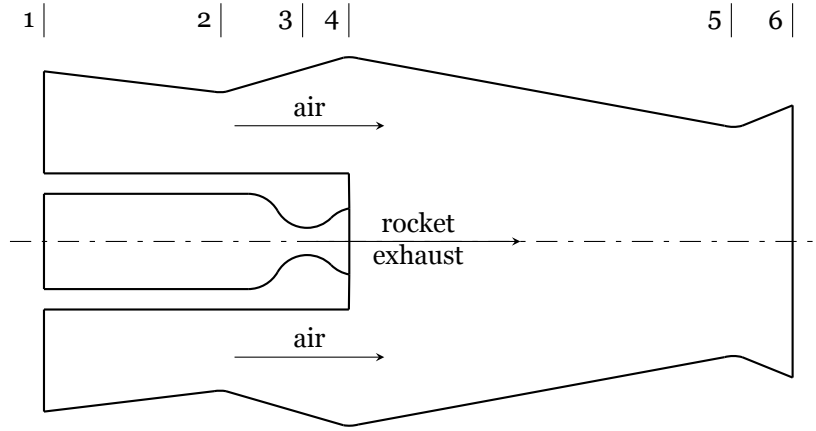
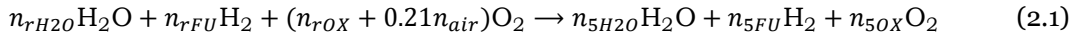


Figure 2.3: General schematic of an RBCC engine with used annotations of sections

### 2.1.2. Chemical equilibrium calculations

The simulation of chemical reactions within the afterburner was one of the key aspects in order to get accurate results. A decision was made to use chemical equilibrium model as it is relatively simple thus allowing for quick calculations. It does not, however, take into account chemical mixing, it is therefore assumed that the mixture is perfectly homogeneous. This problem is addressed in section 2.2.

It is assumed that the following reaction is taking place in the afterburner:



It is assumed that nitrogen and argon, which are other notable elements in air composition, do not react within the afterburner but they are taken into account while calculating properties of the exhaust. This is done by including their constant pressure specific heat contribution in calculating the weighted average specific heat of the mixture. This approach is deemed as a good approximation. Similarly, hydroxyl radical and atomic oxygen and hydrogen were skipped as products of the reaction as their fractions within the exhaust gases are usually insignificant. This was confirmed by analysing Rocket Propulsion Analysis program [21] results for the core rocket engine. Even for oxidizer-rich cases ( $\frac{O}{F} = 12$ ) mass fractions of hydroxyl radical and atomic oxygen are at least an order of magnitude lower than that of molecular oxygen and make up together less than 8% of the total mass of the mixture. This is the same for fuel-rich cases and the ratio between atomic and molecular hydrogen.

Molar flow rates of water, hydrogen and oxygen within the rocket engine exhaust were simply calculated based on the oxidizer to fuel ratio and the total mass flow rate. To simplify those calculations, it is assumed that the combustion is complete and any excess of fuel or oxidizer is passed to the afterburner. In reality the reaction will never consume all fuel or oxidizer. However, since chemical equilibrium calculations are conducted for the afterburner anyway, this should not influence the results much.

The last important value was the molar flow rate of the air, which could be simply calculated from the given mass flow rate of the air. Now, 3 equations could be formulated to be able to find molar flow rates of oxygen, hydrogen and water within the RBCC engine exhaust:

$$\begin{cases} 2n_{rH_2O} + 2n_{rFU} = 2n_{5H_2O} + 2n_{5FU} \\ n_{rH_2O} + 2(n_{rOX} + 0.21n_{air}) = n_{5H_2O} + 2n_{5OX} \\ K_p(T_5) = \frac{n_{5H_2O}}{n_{5FU}\sqrt{n_{5OX}}} \left( \frac{p_5[\text{bar}]}{n_{5H_2O} + n_{5FU} + n_{5OX}} \right)^{-\frac{1}{2}} \end{cases} \quad (2.2)$$

First two equations concern conservation of the number of oxygen and hydrogen atoms within the flow. The last one is an equilibrium equation that describes dissociation of water into hydrogen and oxygen.  $K_p$  is the equilibrium constant for this reaction, which was taken from the NIST-JANAF Thermochemical Tables [4]. This constant depends on temperature  $T_5$  while pressure  $p_5$  is also present in the equation. This implies that the simulation needs to be iterative with initial guesses of those values checked against the results after every iteration.

### 2.1.3. Flow equations for the afterburner

The afterburner in the case of an RBCC engine is a mixer of two flows with different parameters. Because the SMC principle is used, the heat released from the chemical reactions also needs to be taken into account. To simulate those effects, an approach similar to the one presented by Koupriyanov and Etele [14] was adopted. In this approach the conservation of mass, momentum and energy equations were used and solved to find pressure  $p_5$ , temperature  $T_5$  and Mach number  $M_5$  at the end of the afterburner. In this section these 3 equations, taken directly from the study by Koupriyanov and Etele [14], will be described in detail.

The mass conservation equation is written as follows:

$$\dot{m}_r(1 + \alpha) = p_5 A_5 \sqrt{\frac{\gamma_5}{R_5 T_5 \left(1 + \frac{\gamma_5 - 1}{2} M_5^2\right)}} M_5 \sqrt{1 + \frac{\gamma_5 - 1}{2} M_5^2} \quad (2.3)$$

In this equation the left-hand side represents the mass flowing into the afterburner.  $\dot{m}_r$  is the mass flow rate of the rocket engine while  $\alpha$  is the bypass ratio, which is the ratio of the air mass flow rate to  $\dot{m}_r$ . This side is known for each calculated case thanks to the data provided in the paper by Masuya et al. [15]. The right hand side describes the mass flow rate that is flowing out of the afterburner. Apart from the unknowns mentioned earlier, it contains  $A_5$  — cross-section area,  $\gamma_5$  — isentropic exponent of the afterburner exhaust and  $R_5$  — specific gas constant of the afterburner exhaust.

It is worth repeating here that gas properties of the exhaust were calculated based on its composition, which was known from chemical equilibrium calculations. The specific gas constant  $R_5$  in this case could be calculated by dividing the universal gas constant by mean molar mass. Constant pressure specific heat  $C_{p5}$ , on the other hand, was a weighted average of specific heats of gases that the exhaust consisted. Finally, the isentropic exponent could be approximated using the formula:  $\gamma_5 = \frac{C_{p5}}{C_{p5} - R_5}$ , which is true for ideal gases.

The next equation to discuss is the momentum conservation:

$$M_5^2 = \frac{1}{\gamma_5} \left( \frac{\dot{m}_r a_r^*}{p_5 A_5} (\alpha \sqrt{\theta} \Gamma \chi_4 + \chi_{4r}) - F_{p,x} - 1 \right) \quad (2.4)$$

This equation is dimensionless because it was simplified by reducing common terms (divided by  $p_5 A_5$ ). Apart from variables mentioned earlier it contains  $a_r^*$ , which is the critical sonic velocity of the rocket exhaust, which is calculated as follows:

$$a_r^* = \sqrt{2 \frac{\gamma_r - 1}{\gamma_r + 1} C_{pr} T_{0r}} \quad (2.5)$$

The following symbols are used to simplify the notation:

$$\theta = \frac{C_{pair}T_{0air}}{C_{pr}T_{0r}} \quad (2.6)$$

$$\Gamma = \sqrt{\frac{(\gamma_{air} - 1)(\gamma_r + 1)}{(\gamma_{air} + 1)(\gamma_r - 1)}} \quad (2.7)$$

$$\chi_4 = \frac{M_4 + \frac{1}{\gamma_{air}M_4}}{\sqrt{\frac{2}{\gamma_{air}+1} + \left(\frac{\gamma_{air}-1}{\gamma_{air}+1}\right)M_4^2}} \quad (2.8)$$

$$\chi_{4r} = \frac{M_{4r} + \frac{1}{\gamma_r M_{4r}}}{\sqrt{\frac{2}{\gamma_r+1} + \left(\frac{\gamma_r-1}{\gamma_r+1}\right)M_{4r}^2}} \quad (2.9)$$

In those expressions  $C_{pair}$  is the constant pressure specific heat of the air (assumed equal to  $1250 \frac{\text{J}}{\text{kg K}}$ , which is a realistic value according to the paper by Wong and Embleton [29]),  $\gamma_{air}$  is the isentropic exponent of the air (assumed equal to 1.4) and  $M_4$  is the Mach number of the air when entering the afterburner. The last value was determined based on the static and total pressure ratio (see figure 2.2).

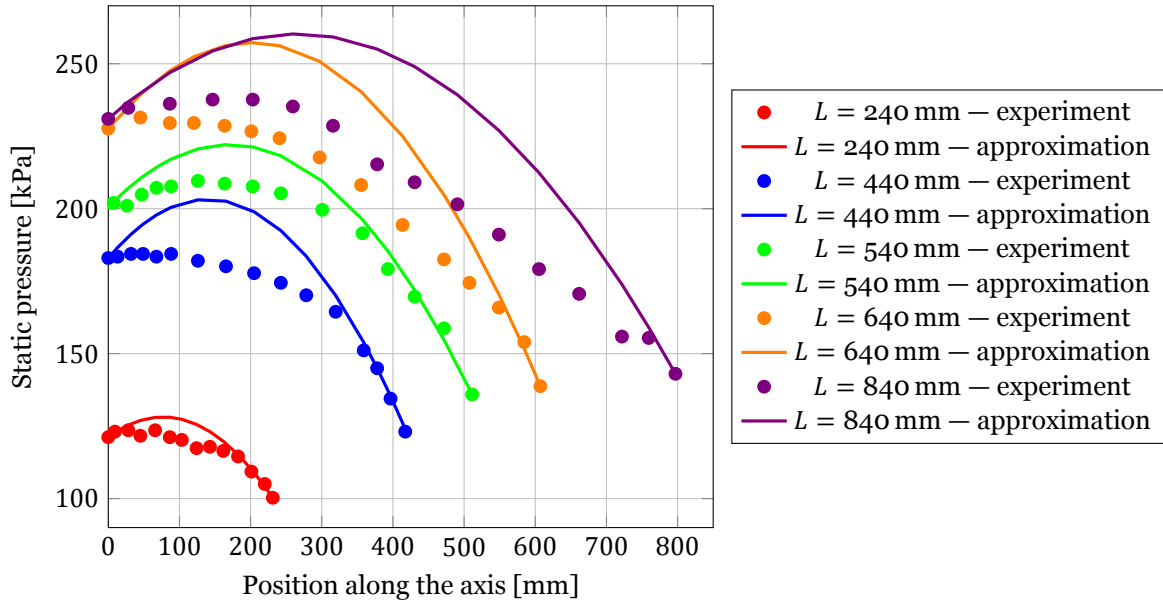


Figure 2.4: Plot of experimental data of wall pressure along the afterburner axis from Masuya et al. [15] for different afterburner lengths compared with approximations used in the model

The last important expression is the one below, which represents dimensionless pressure force acting on the wall of the afterburner:

$$F_{p,x} = \frac{1}{p_5 A_5} \int_0^L p_w(x) d\vec{A} \quad (2.10)$$

$p_w(x)$  in this equation is the wall pressure function that was integrated throughout the whole afterburner over its walls. Only the axial component of this force was taken into account. This integral is to simulate the effect of a changing cross-section area (for a constant cross-section of the afterburner it is equal to 0). The wall pressure function was approximated as a 2<sup>nd</sup> degree polynomial. Its coefficients were chosen to match the boundary conditions (guess of pressure  $p_5$  and pressure of the air

coming into the afterburner  $p_4$ ) and to have the maximum at one third of the combustor length. This approximation was deemed suitable after analysing wall pressure distributions measured by Masuya et al. [15], which are presented in figure 2.4. Along with those, presented are approximations used in the model. As can be seen, this fit overpredicts pressure in the middle of the afterburner but reflects the trend, which was confirmed by the analysis of correlation coefficients, presented in table 2.2. Generally, achieved fit is acceptable given that the simplicity of the function was a priority in order to make the model computationally cheap.

Table 2.2: Correlation coefficients of experimental data on wall pressure distribution in the afterburner from Masuya et al. [15] and approximation used in the model

Case	Correlation coefficient
$L = 240$ mm	0.9516
$L = 440$ mm	0.9642
$L = 540$ mm	0.9872
$L = 640$ mm	0.9603
$L = 840$ mm	0.9243

The last conservation equation to discuss is the energy equation:

$$\sum_k n_k h_k(T_5) + \frac{1}{2} \gamma_5 \dot{m}_r (1 + \alpha) R_5 T_5 M_5^2 = \dot{m}_r \left( C_{pr} T_{0r} (\alpha \theta + 1) + \sum_k \frac{Y_k}{W_k} h_{f,k} - T_{ref} (\alpha C_{pair} + C_{pr}) \right) \quad (2.11)$$

The left-hand side of this equation represents the total enthalpy flowing out of the afterburner. The first component is the sum of molar enthalpies  $h_k$  of species within the exhaust, which are dependent on temperature, multiplied by respective molar flow rates. The molar enthalpies of species have been approximated using polynomials from the NIST Chemistry WebBook [17]. The second component is the kinetic energy of the flow.

The right-hand side represents enthalpy flowing into the afterburner. Here  $h_{f,k}$  is the heat of formation of species in the core rocket engine exhaust (in the validation case there is only a non-zero term for water),  $Y_k$  is the mass fraction of those species within the exhaust and  $W_k$  is their molar mass.  $T_{ref}$  is the temperature of the reference state, which in this case was 298.15 K.

Equations 2.3, 2.4 and 2.11 form a closed system with 3 unknowns so it is possible to solve them. Unfortunately, results from an early implementation showed large discrepancies with experimental data from Masuya et al. [15]. Those issues were tracked down to a lack of thermal choking modelling. This phenomenon occurs frequently in the subsonic combustion or otherwise called rocket-ramjet mode, which was the subject of this study. It involves increasing the Mach number of the flow solely due to heat addition. This means that despite low Mach numbers in the afterburner, the flow may become sonic at its exit. Parallel to that, both total and static pressure decrease.

A simple yet effective model of this phenomenon is the Rayleigh flow. Equations describing it have been used in the simulation. The method how Rayleigh flow has been incorporated into the model is presented in figure 2.5.

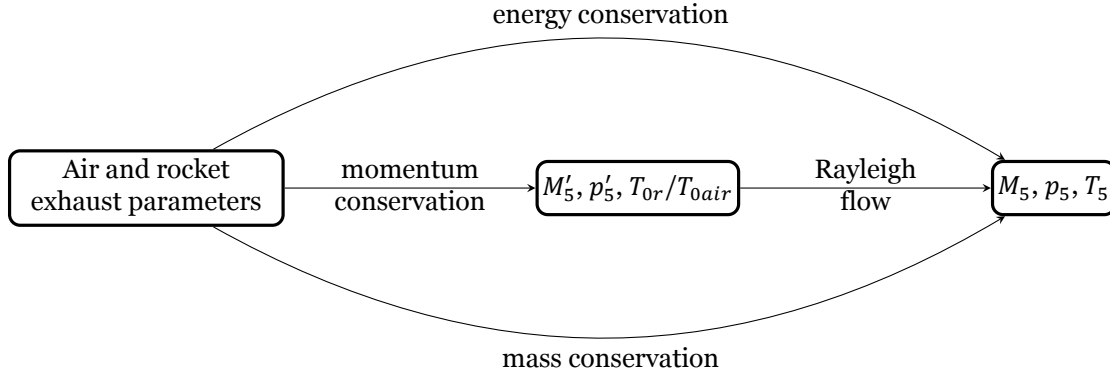


Figure 2.5: Illustration of the Rayleigh flow equations implementation in the afterburner simulation

The method involves creating a fictitious state of the flow in which it already has uniform Mach number and pressure calculated based on the momentum equation but no heat was yet exchanged. Naturally, this means that one part of the flow has the total temperature of the air  $T_{0air}$  and the other the total temperature of the rocket exhaust  $T_{0r}$ . This state can be then connected to the final Mach number and pressure through the following equations:

$$\frac{T_5 \left(1 + \frac{\gamma_5 - 1}{2} M_{5air}^2\right)}{T_{0air}} = \left(\frac{1 + \gamma_5 M_5'^2}{1 + \gamma_5 M_{5air}^2}\right)^2 \left(\frac{M_{5air}}{M_5'}\right)^2 \frac{1 + \frac{\gamma_5 - 1}{2} M_{5air}^2}{1 + \frac{\gamma_5 - 1}{2} M_5'^2} \quad (2.12)$$

$$\frac{T_5 \left(1 + \frac{\gamma_5 - 1}{2} M_{5r}^2\right)}{T_{0r}} = \left(\frac{1 + \gamma_5 M_5'^2}{1 + \gamma_5 M_{5r}^2}\right)^2 \left(\frac{M_{5r}}{M_5'}\right)^2 \frac{1 + \frac{\gamma_5 - 1}{2} M_{5r}^2}{1 + \frac{\gamma_5 - 1}{2} M_5'^2} \quad (2.13)$$

$$p_5 = p_5' \frac{1 + \gamma_5 M_5'^2}{1 + \gamma_5 M_5^2} \quad (2.14)$$

$$M_5 = \frac{\alpha \dot{m}_r M_{5air} + \dot{m}_r M_{5r}}{\dot{m}_r (1 + \alpha)} \quad (2.15)$$

Equations 2.12, 2.13 and 2.14 are integrated Rayleigh flow equations directly applied to the flow at hand. Typically, heat from the rocket exhaust will reject heat and the air will absorb it. Meaning that, in the case of subsonic flow, Mach number  $M_{5air}$  will be higher than  $M_5'$  while  $M_{5r}$  will be lower. To solve this discrepancy, the final Mach number at the end of the ejector is calculated as weighted average based on mass flow rates as in equation 2.15.

Equations 2.3, 2.4, 2.11 together with 2.12, 2.13, 2.14 and 2.15 form a closed system with  $T_5$ ,  $p_5$ ,  $M_5$ ,  $M_5'$ ,  $p_5'$ ,  $M_{5air}$  and  $M_{5r}$  as unknowns. It is important to remember, however, that the momentum equation 2.4 has to be modified to include  $M_5'$  and  $p_5'$  instead of  $M_5$  and  $p_5$ . Those equations, along with the equilibrium chemistry calculation model, were implemented in a quasi-1D model written in MATLAB [16]. This model is used to produce the results described in section 2.2.

## 2.2. Validation model results

The cases that were considered for the simulation were restricted by the validation data available in the study by Masuya et al. [15]. Although a large number of experiments were carried out, direct results for exit pressure were available only for the case of  $\alpha = 5.3$  and combustor B-I (see figure 2.1). The most interesting was the case of the full length combustor ( $L = 1040$  mm) because this is when the streams are supposedly fully mixed so the chemical equilibrium model should be accurate. In terms of the oxidizer-fuel ratio, the following were chosen as test cases: 2, 2.86, 4, 6, 8 and 10. They roughly translate to the experiment points from the study. In the cases that were not available, an interpolation provided by Masuya et al. [15] was used.

In the study it was implied multiple times that the flow at the end of the afterburner was sonic in all cases. The results of the simulation do not reflect this exactly. For all cases Mach numbers between 0.7

and 0.9 were obtained. This is, however, explained by the fact that Mach number of the inlet air was read from the plot of static and total pressure yielding large uncertainties. In fact, a few test runs proved that small changes in this number moved the resulting Mach number considerably. This implies that correct Mach numbers yielding sonic conditions at the exit could be found. However, the algorithm becomes numerically unstable when the inlet Mach number is increased to values very close to this yielding Mach 1 at the exit. Therefore, the results were left as initially obtained and total pressure and temperature were used for comparison.

### 2.2.1. Combustion efficiency function

As mentioned in section 2.1.2, the model does not take into account the influence of mixing on the rate of the reaction. To simulate this influence, a combustion efficiency function was developed in order to better match total pressure results with the experimental data. As per definition the combustion efficiency is calculated as follows:

$$\eta_c = \frac{c^*}{c_{ideal}^*} = \frac{\frac{p_{5real} A_5}{\dot{m}_r(1+\alpha)}}{\frac{p_5 A_5}{\dot{m}_r(1+\alpha)}} = \frac{p_{5real}}{p_5} \quad (2.16)$$

From this equation it is visible that combustion efficiency can be interpreted as a linear modifier of the pressure at the end of the afterburner calculated from the developed model (assuming that the mass flow rate in the real case is the same as in the simulation). As such, it was predicted that combustion efficiency should be dependent on the length of the afterburner with respect to its diameter and the amount of fuel in the rocket exhaust measured by the oxidizer-fuel ratio of the core rocket engine. The latter was used with comparison to the oxidizer-fuel ratio guaranteeing stoichiometric combustion in the afterburner  $\left(\frac{O}{F}\right)_s = 3.008$ . This number is constant for the validation case since the mass flow rate of the core rocket and of the air are constant.

Keeping the above in mind, it was possible to develop a certain function that would take values between 0 and 1 in order to match simulation results and experimental data. Coefficients within this function were chosen arbitrarily to match experimental results.

$$\eta_c = 1 - \frac{0.1088}{\left(\frac{L}{d_5}\right)^{\frac{1}{3}} - 0.973 + 2.0467 \cdot \left(\frac{O}{F} - \left(\frac{O}{F}\right)_s\right)} \quad (2.17)$$

Figures 2.6 and 2.7 show this function plotted against  $\frac{L}{d_5}$  and  $\frac{O}{F}$  respectively, while keeping the other variable constant. As can be seen, the combustion efficiency drops sharply with the decreasing oxidizer-fuel ratio. This is to be expected as more fuel is available at those cases and therefore more of it will be unburned due to non-ideal mixing. Similarly, combustion efficiency drops when the afterburner becomes shorter allowing for less mixing. This effect, however, diminishes when the oxidizer-fuel ratio is increased as for those cases combustion in the afterburner is very limited.

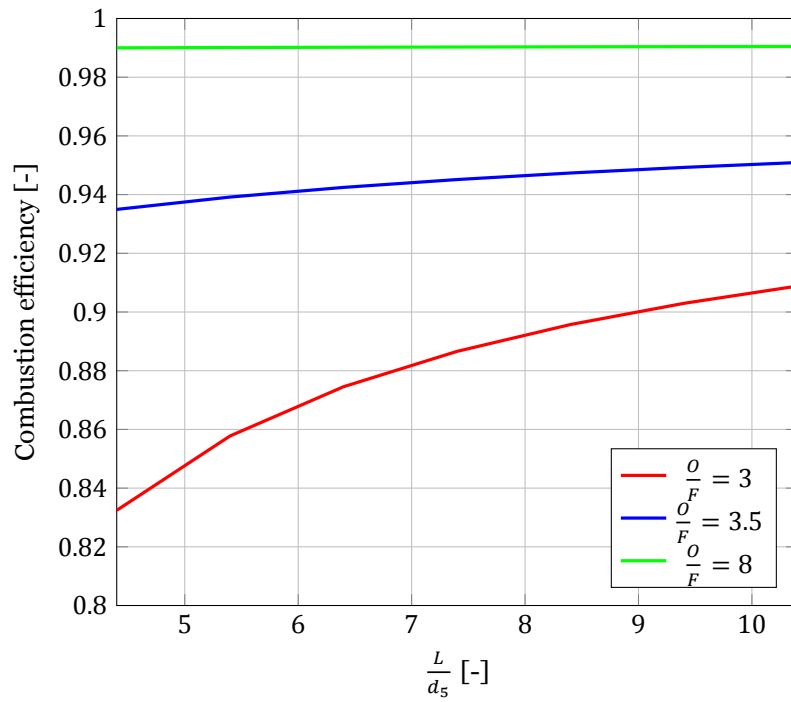


Figure 2.6: Combustion efficiency function plotted against  $\frac{L}{d_5}$  for different oxidizer-fuel ratios of the core rocket engine

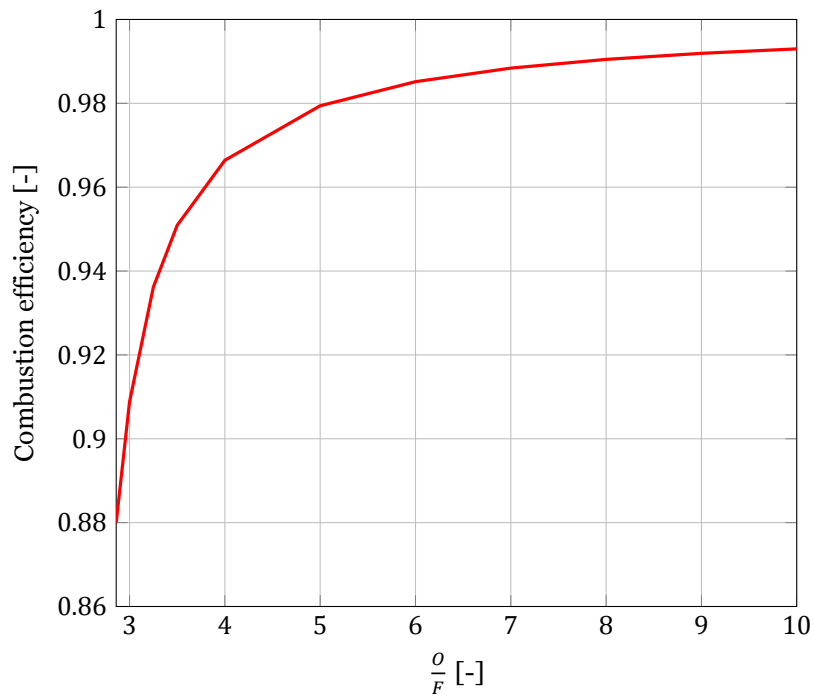


Figure 2.7: Combustion efficiency function plotted against oxidizer-fuel ratio of the core rocket engine for  $\frac{L}{d_5} = 10.4$

### 2.2.2. Total temperature predictions comparison

The study by Masuya et al. [15] was focused on pressure measurements and therefore no experimental data on temperature was available. However, predictions of total temperature at the afterburner exit were published in this paper and are presented along with the simulation results in figure 2.8.

As visible, the predictions agree quite well with each other for the range of oxidizer-fuel ratios from 2 to 6. After that, however, discrepancy is large and the simulation seems to underestimate the temperature. There are several reasons why the developed model might not agree with predictions by Masuya et al. [15] but in this range it is probable that the total temperature and specific heat of the rocket exhaust used in the calculations are different. For the simulation this data was taken from Rocket Propulsion Analysis program [21] (see table 2.1). The authors of the study do not state how this data was obtained. The reason why it is expected that the difference in rocket exhaust parameters is the source of discrepancy is that in this range very limited combustion is taking place in the afterburner. This is due to the lack of fuel to burn so the only major source of heat is the hot rocket exhaust itself. This means that if its temperature and specific heat is inaccurate, then the results tend to differ drastically. Overall, despite the mentioned discrepancy, this data is the evidence that reasonable results can be obtained from the model. The simulation shows the same trends as the predictions of Masuya et al. [15]. For example, the maximum is at the same oxidizer to fuel ratio. Also, agreement was reached in the most interesting range, which is around  $\frac{O}{F} = 4$  (this is where highest specific impulse of the RBCC engine is expected).

To summarise, since this is a comparison of 2 models' results and not a comparison with experiment, it was decided that the detected discrepancy should not disqualify the model as invalid. Additionally, trends that the simulation produces and the fact of good agreement in the range of interest support the conclusion that the presented results can be trusted.

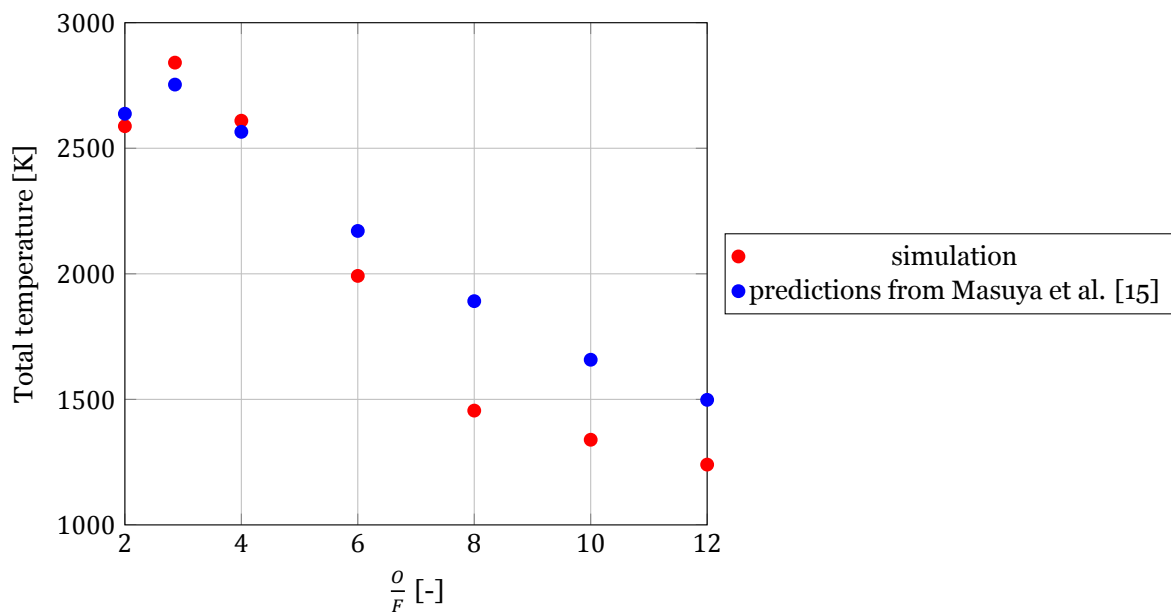


Figure 2.8: Plot of total temperature at the afterburner exit against the oxidizer-fuel ratio of the core rocket engine

### 2.2.3. Total pressure comparison

The total pressure is a good indicator of whether the simulation is accurate enough to proceed with the development model. This is due to 2 reasons. Firstly, because pressure was directly measured in experiments by Masuya et al. [15]. Secondly, because this value reflects the momentum of the flow that can then be transformed into thrust by a nozzle.

As mentioned before, the most interesting was the data for the longest afterburner. This comparison is presented in figure 2.9. As visible, a very good agreement has been achieved proving the accuracy of the model.

Similarly, the introduction of the combustion efficiency into the quasi-1D model resulted in good agreement for the cases of different afterburner lengths. This comparison for 2 different oxidizer-fuel ratios is presented in figure 2.10.

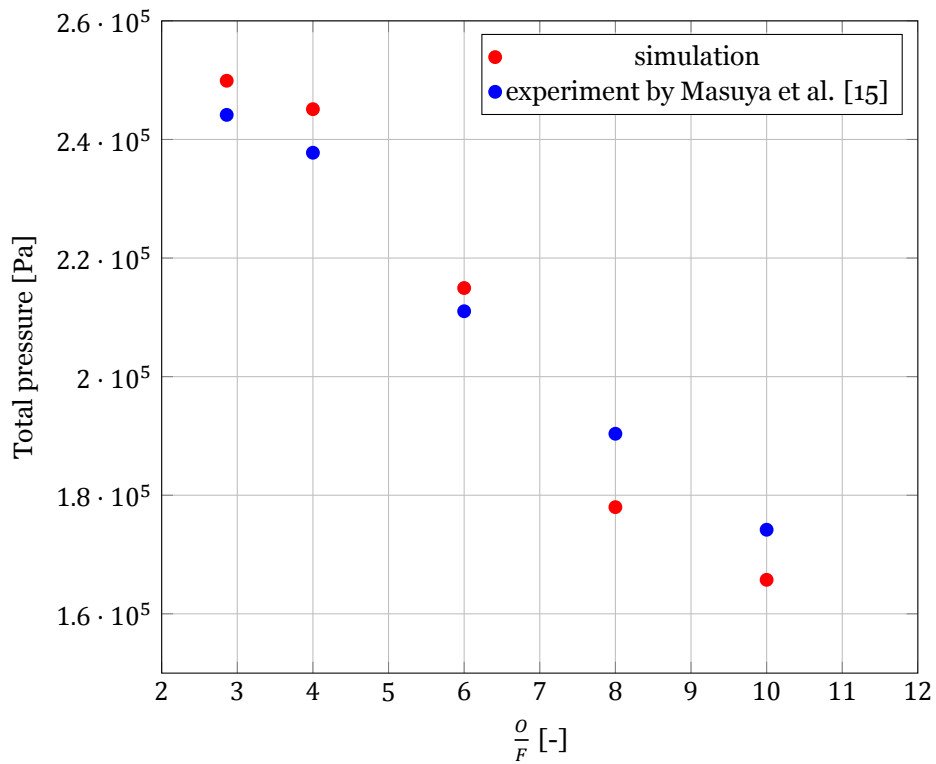


Figure 2.9: Plot of total pressure at the afterburner exit against the oxidizer-fuel ratio of the core rocket engine for the 1040 mm long afterburner

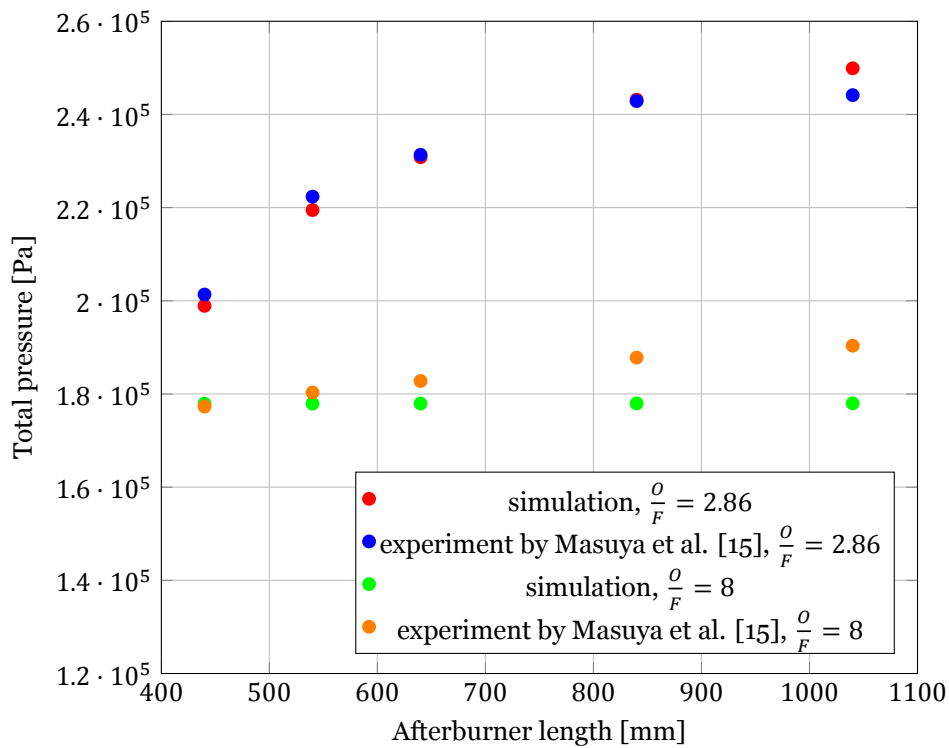


Figure 2.10: Plot of total pressure at the afterburner exit against the afterburner length

### 2.3. Development model description

The development model was created to consider different designs of RBCC engines that could be used with Mk-II *Aurora* engine as their core. This development model was based entirely on the principles of the validation model described in section 2.1. It was done to ensure that its results are also well matched with reality. However, some changes had to be made in order to produce the results for the case of the Mk-II *Aurora* engine and to ensure that the simulation can take into account all flight conditions. Those changes were:

- different rocket engine performance data, produced again using Rocket Propulsion Analysis program [21] and presented in figure 2.11, in this case the total mass flow rate and, as a consequence, total pressure did not stay constant to match how oxidizer-fuel ratio can be changed in the real life engine at full throttle,
- the Mach number at the core rocket engine nozzle exit calculated based on isentropic expansion to be able to change expansion ratio,
- the calculation of the air parameters at the afterburner inlet based on flight conditions and the Standard Atmosphere model [26] (explained in detail in sections 2.3.1 and 2.3.2),
- the change of fuel and oxidizer to kerosene and hydrogen peroxide, therefore also a change of the reaction considered for chemical equilibrium calculations (explained in detail in section 2.3.3).

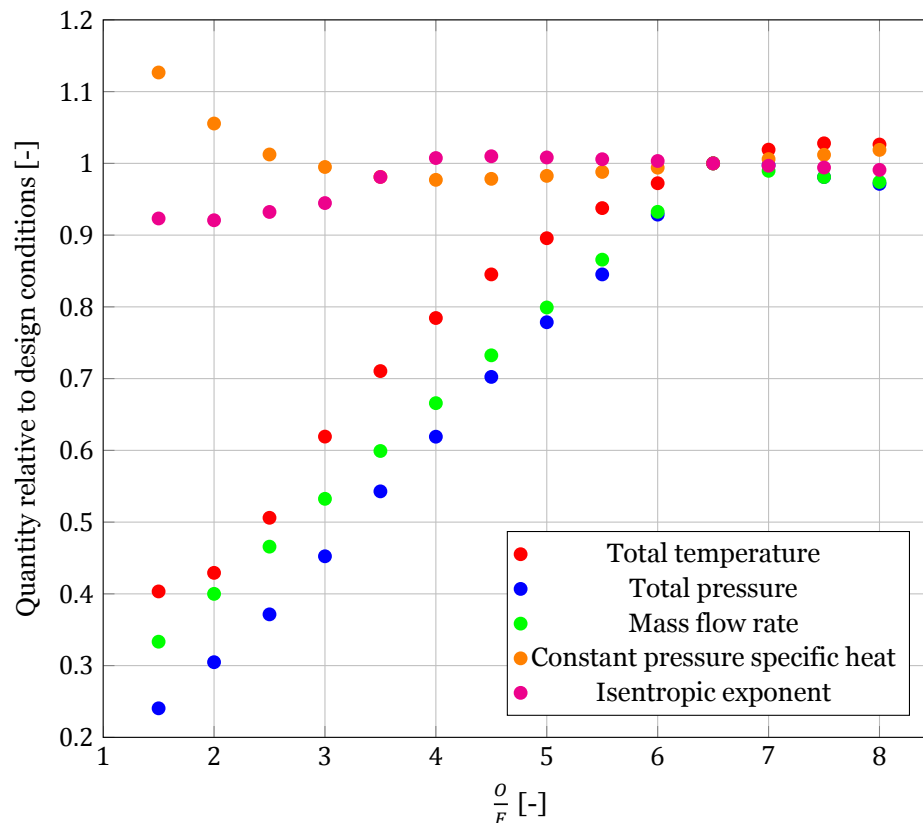


Figure 2.11: Plot of parameters of the Mk-II *Aurora* rocket engine exhaust relative to design operation against oxidizer to fuel ratio, calculated using Rocket Propulsion Analysis program [21]

### 2.3.1. Overall simulation logic

The block diagram explaining the overall simulation scheme is presented in figure 2.12. As visible, there are 2 major operation modes: rocket ejector and rocket-ramjet. The switch between modes is made at the free stream Mach number  $M_\infty = 1$ . This is naturally the lowest Mach number at which the inlet could be started (meaning that the flow would be supersonic at the inlet entry), although that will not be the case for all conditions and designs. Therefore, in the rocket ejector case the flow at the inlet entry is assumed to be subsonic (although may be choked later on) and in the rocket-ramjet case supersonic. Consequently, the mass flow rate of the air in the rocket-ramjet case is always independent on the conditions in the afterburner while in the rocket ejector case it may depend on the afterburner pressure.

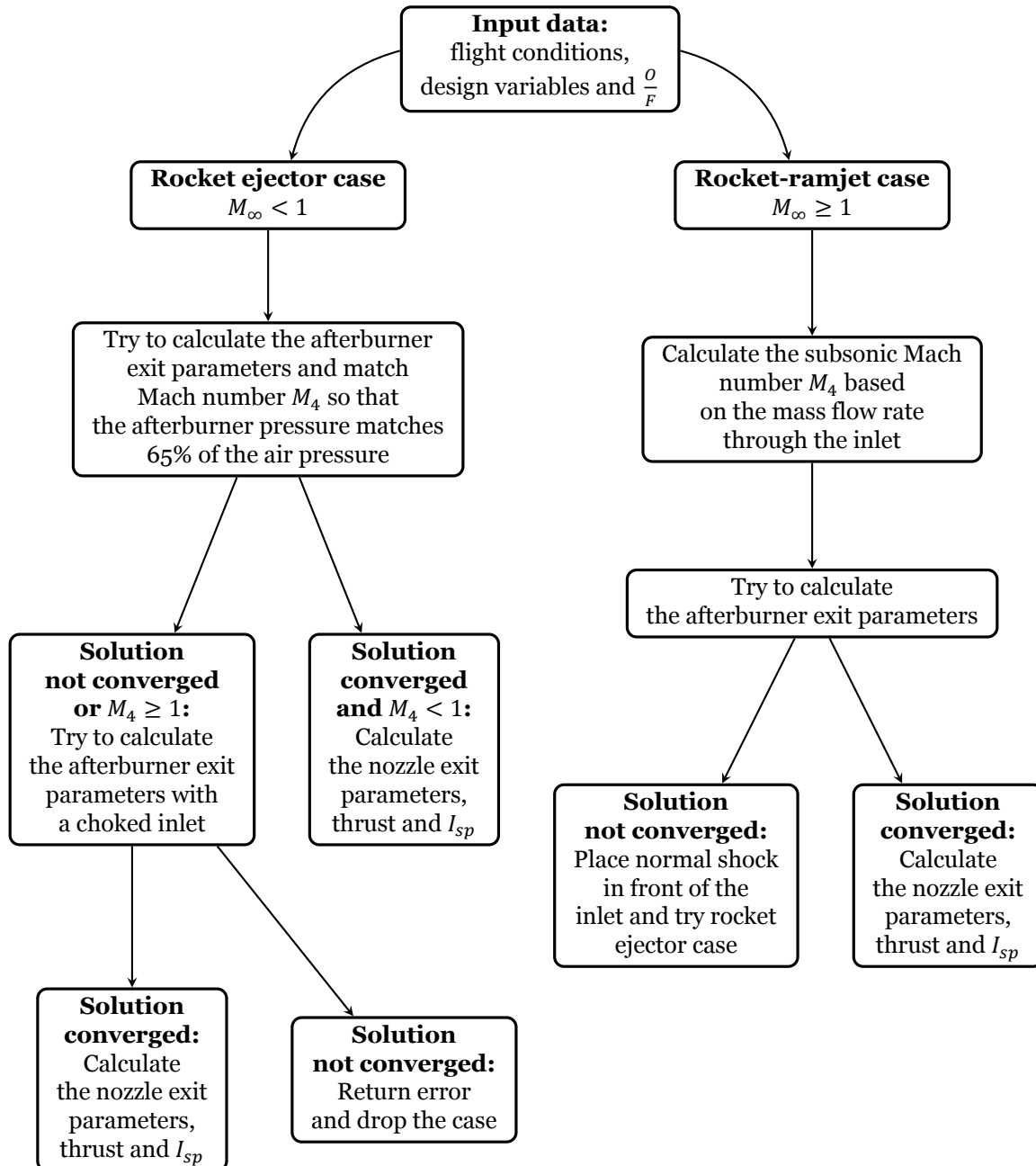


Figure 2.12: Block diagram of the development model implementation

The rocket ejector mode may be realised at 2 different variants: with or without a choked inlet. The first one of those is always tried first. In this case  $M_4$  is a variable and is chosen so that the pressure in the afterburner constitutes 65% of the static pressure of the incoming air. This number was chosen based on early CFD results and is used to simulate the pressure drop within the afterburner. If this solution converges with  $M_4 < 1$  then the calculations are finished (see section 2.3.4). The other option is that the inlet becomes choked. This means that the mass flow rate is now only dependent on air parameters and inlet throat cross-section area  $A_2$ . In this case the flow at the inlet to the afterburner is sonic or supersonic.

It is important to mention that for the rocket ejector mode the equations used do not include Rayleigh flow so thermal choking is not possible. This is done to save computational time as differences in the results with and without Rayleigh flow included were within 1% of each other.

For the rocket-ramjet mode situation is simpler. Mach number at the afterburner inlet  $M_4$  is always subsonic because the flow would go through a number of shock waves ended with a terminal normal shock wave. Mass flow rate is also defined by the inlet entry area. A discharge coefficient of 0.8 is used in this calculation based on early CFD results. If convergence is reached with such conditions then the calculations are finished (see section 2.3.4). If it is not, the inlet is assumed to be unstarted so normal shock is placed in front of the inlet and calculations continue as for the rocket ejector case. This is also reported in the results.

The convergence criteria for all cases are the same and are relatively relaxed due to the model being an early approximation. Considered residuals are:

- assumed static temperature  $T'_5$  within 100 K of calculated temperature  $T_5$ ,
- assumed static pressure  $p'_5$  within 15% of calculated pressure  $p_5$ .

The temperature criterion is defined in absolute terms because validity ranges of different polynomials used for determination of gas properties are multiples of 100 K. The pressure residual, on the other hand, was chosen to be relatively big because pressure dependence on chemical equilibrium calculations is weak so accuracy of the whole method was not heavily impacted. At the same time, it is defined in relative terms because the resulting pressure range is relatively wide (from as low as 0.5 bar to as high as 10 bar).

### 2.3.2. Inlet calculations

For inlet calculations the main component was the pressure recovery scheme as presented in figure 2.13. It was used to calculate the total pressure of the air in all cases except for when the inlet was unstarted. This is because the recovery scheme is the emulation of shock waves that may form in the inlet causing the flow to be non-isentropic.

Apart from calculating total temperature and pressure of the air, it is also important to calculate the Mach number at the inlet to the afterburner  $M_4$  in the choked inlet case and ramjet case. This was done by the means of first calculating mass flow rate. In the choked inlet case this was based on the inlet throat area assuming that the flow has to be sonic there and in the ramjet case on the inlet entry area assuming that the Mach number there is the same as  $M_\infty$ .

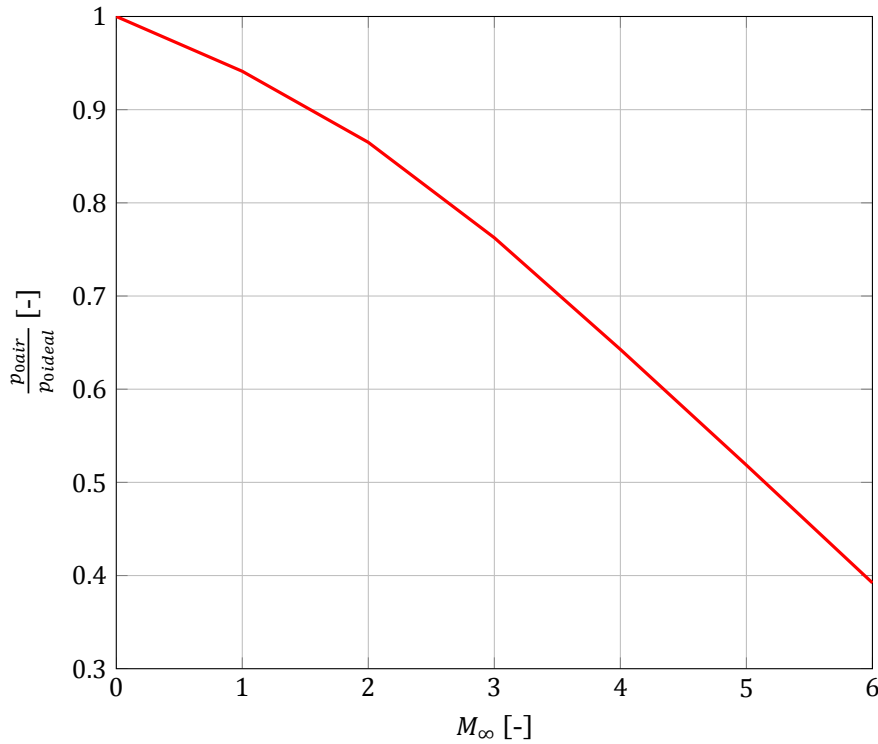


Figure 2.13: Inlet pressure recovery as presented by Olds and Bradford [18]

### 2.3.3. Chemical equilibrium calculations

The change of propellants has an influence on the chemical equilibrium calculations because different reactions had to be considered. However, the method itself remained unchanged.

In the development model the reaction in the rocket engine chamber was different than the one in the afterburner and is presented below:



While  $n_{OX}$  and  $n_{FU}$  are known based on the oxidizer-fuel ratio and the total mass flow rate, the following system of equations is needed to solve for molar flow rates in the rocket engine exhaust:

$$\begin{cases} n_{FU} = n_{CO_2} + n_{CO} \\ 2n_{OX} = n_{H_2O} + 2n_{CO_2} + n_{CO} + 2n_{O_2} \\ 1.953n_{FU} + 2n_{OX} = 2n_{H_2O} + 2n_{H_2} \\ K_{pH_2O}(T_{Or}) = \frac{n_{H_2O}}{n_{H_2}\sqrt{n_{O_2}}} \left( \frac{p_{Or}[\text{bar}]}{n_{H_2O} + n_{H_2} + n_{O_2}} \right)^{-\frac{1}{2}} \\ K_{pCO_2}(T_{Or}) = \frac{n_{CO_2}}{n_{CO}\sqrt{n_{O_2}}} \left( \frac{p_{Or}[\text{bar}]}{n_{CO_2} + n_{CO} + n_{O_2}} \right)^{-\frac{1}{2}} \end{cases} \quad (2.19)$$

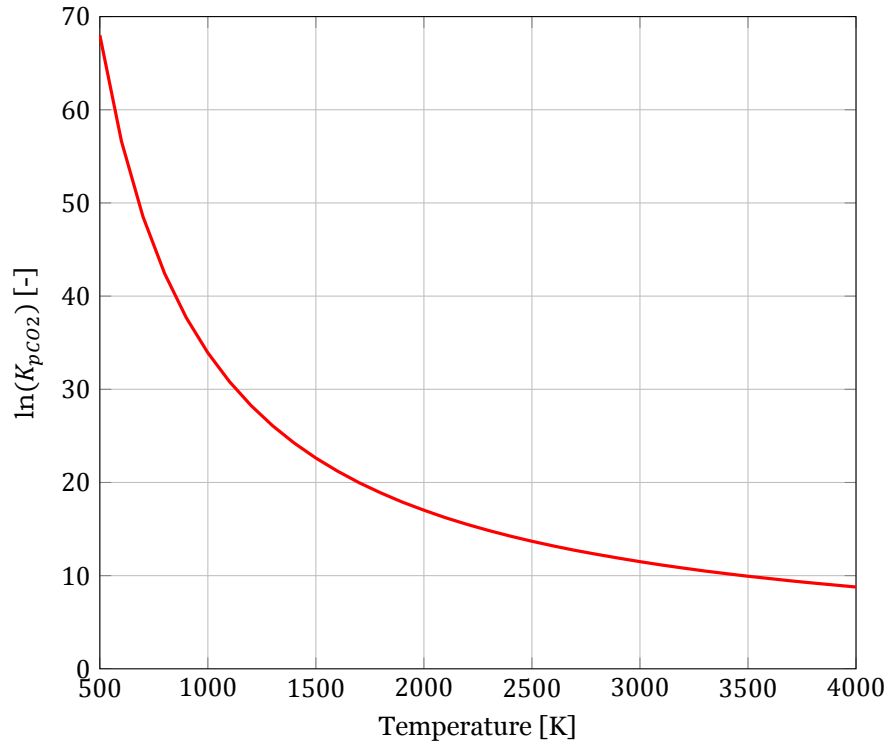


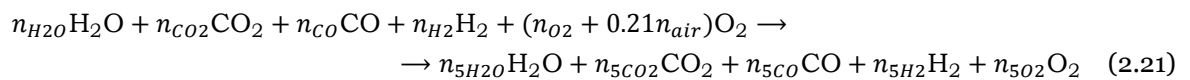
Figure 2.14: Plot of natural logarithm of carbon dioxide equilibrium constant against temperature

Just as in the validation model, the equilibrium constant of water  $K_{pH_2O}$  was taken from NIST-JANAF Thermochemical Tables [4]. Equilibrium constant of carbon dioxide  $K_{pCO_2}$  was not as easily available and had to be calculated from the integrated van't Hoff equation presented below considering the reaction of oxygen and carbon monoxide to form carbon dioxide. In this equation  $R$  is the universal gas constant,  $T$  is temperature,  $\Delta H^0$  is the difference in enthalpy and  $\Delta S^0$  in entropy compared to reference state of 298 K.

$$-RT \ln K_{pCO_2} = (\Delta H^0 - T\Delta S^0)_{CO_2} - \frac{1}{2}(\Delta H^0 - T\Delta S^0)_{O_2} - (\Delta H^0 - T\Delta S^0)_{CO} \quad (2.20)$$

Data used in this calculation was obtained again from NIST-JANAF Thermochemical Tables [4]. The result is presented in figure 2.14.

The reaction in the afterburner is that of products from the core rocket engine and oxygen from the air. Again, nitrogen and argon are assumed to not take part in the reaction entirely.



The system of equations needed to solve for products' molar flow rates is almost the same as the one for the core rocket engine:

$$\begin{cases} n_{CO_2} + n_{CO} = n_{5CO_2} + n_{5CO} \\ n_{H_2O} + 2n_{CO_2} + n_{CO} + 2(n_{O_2} + 0.21n_{air}) = n_{5H_2O} + 2n_{5CO_2} + n_{5CO} + 2n_{5O_2} \\ 2n_{H_2O} + 2n_{H_2} = 2n_{5H_2O} + 2n_{5H_2} \\ K_{pH_2O}(T_5) = \frac{n_{5H_2O}}{n_{5H_2}\sqrt{n_{5O_2}}} \left( \frac{p_5[\text{bar}]}{n_{5H_2O} + n_{5H_2} + n_{5O_2}} \right)^{-\frac{1}{2}} \\ K_{pCO_2}(T_5) = \frac{n_{5CO_2}}{n_{5CO}\sqrt{n_{5O_2}}} \left( \frac{p_5[\text{bar}]}{n_{5CO_2} + n_{5CO} + n_{5O_2}} \right)^{-\frac{1}{2}} \end{cases} \quad (2.22)$$

### 2.3.4. Nozzle calculations

The RBCC nozzle calculations were not a part of the validation model but were necessary to calculate thrust and specific impulse — parameters that mattered for the development model. A simple isentropic flow model was used. This means that the total parameters were calculated based on results for section 5 of the engine. Then, Mach number at section 6 was found based on the area ratio of the nozzle. Finally, static parameters at section 6 were calculated. If the flow at section 5 was subsonic, it was assumed that it is choked there anyway as those results were very close to sonic conditions in all considered cases.

Thrust could be then found using the following expression:

$$T = \eta_c \eta_n (\dot{m}_r (1 + \alpha) M_6 a_6 - \dot{m}_r \alpha M_\infty a_\infty + A_6 (p_6 - p_\infty)) \quad (2.23)$$

In this equation  $a$  with an appropriate subscript annotates the local speed of sound. The expression itself is an expanded version of the general thrust equation and contains a difference between momentum of the exhaust and of the inlet air plus an additional term accounting for a difference in static pressure between the exhaust and the atmosphere. Additionally, two quality factors are taken into account: discussed in section 2.2.1 combustion efficiency  $\eta_c$  and nozzle quality, which was assumed constant  $\eta_n = 0.94$ .

Specific impulse was derived from thrust simply as:

$$I_{sp} = \frac{T}{\dot{m}_r g_0} \quad (2.24)$$

## 2.4. Development model results

The development model was used to conduct a survey of different designs and their behaviour under varying flight conditions. The following sections present the most important results of this survey, which explain why certain design choices have been made. This process, however, was not in any case the optimisation. Proper optimisation of the RBCC engine would have to include trajectory optimisation along with mass and drag estimations. However, at this early stage of design it was deemed suitable to find only a feasible solution and not an optimal one.

It is also worth mentioning here that static geometry of the engine (meaning e.g. no moving nozzle) was highly preferred to reduce mass and complexity of the engine. The only place where moving parts could be considered was the inlet. However, as shown in section 2.4.2, they proved to be unnecessary.

### 2.4.1. Afterburner size and core rocket nozzle expansion ratio

The most important geometric parameters to determine were dimensions of the afterburner and the core rocket nozzle expansion ratio. The length of the afterburner was known prior to conducting the survey as a function of its diameter and had to be chosen so that the ratio of length to diameter was at least 5 to allow effective mixing. This is the conclusion from studies such as the one by Masuya et al. [15], which narrowed the decision to only choosing the diameter or equivalently exit area of the afterburner.

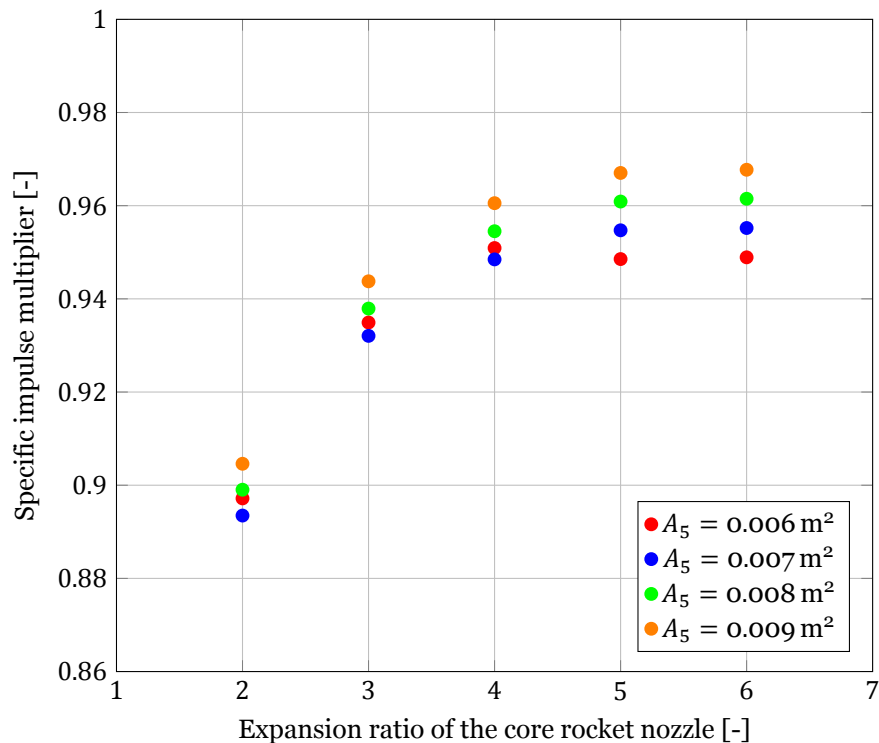


Figure 2.15: Plot of specific impulse multiplier (compared to rocket-only propulsion) against expansion ratio of the core rocket nozzle for different afterburner diameters at static sea level conditions

By running multiple cases at different flight conditions, it has become apparent that take-off condition is by far the most problematic. This is due to two major facts: specific impulse being low at these conditions for practically all designs and pressures in the afterburner being low causing a risk of flow separation in the RBCC nozzle. Both of those facts are of course highly undesirable so take-off conditions were chosen as a design point to counter those issues.

Having the nozzle flow separation issue in mind, all designs considered in this section were fitted with a low expansion ratio RBCC nozzle. This allowed for choosing a higher cross-section area of the afterburner, which, as presented in figure 2.15, is a very important parameter that can increase the performance of the engine. Similar behaviour was observed for higher Mach numbers. From this plot it is apparent that in most cases a bigger afterburner is better. However, this comes at a price of lowering the pressure in the afterburner and possibly causing flow separation. In fact, the design with  $A_5 = 0.009 \text{ m}^2$  may already run into this problem. The chosen criterion of assessing this was taken from a study by Stark [27] and was based on comparing pressure at the nozzle exit with a calculated separation pressure. To account for simulation inaccuracies, an additional margin of 15% was applied to this calculated separation pressure and this value was used as a threshold of separation.

In the end, a decision was made to choose  $A_5 = 0.008 \text{ m}^2$  as it is a safe option that has sufficient thrust at take-off. Figure 2.15 suggests that it should be paired with expansion ratio of around 5 or 6 to achieve best performance. Value of 5 was chosen in this case as a good trade-off between take-off and higher Mach number conditions, as supported by figure 2.16.

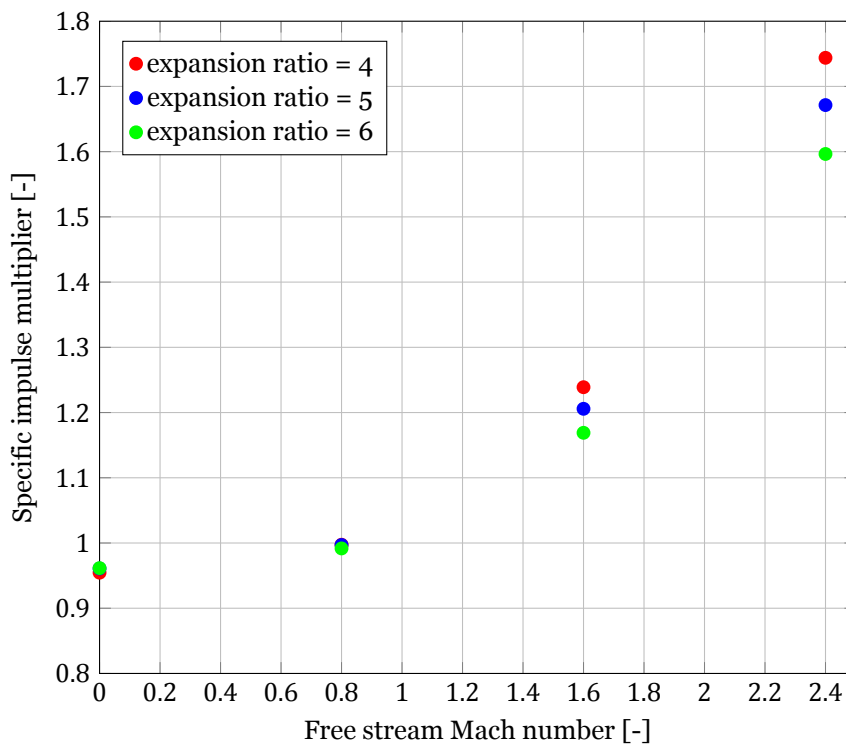


Figure 2.16: Plot of specific impulse multiplier (compared to rocket-only propulsion) against Mach number of the free stream for different expansion ratios of the core rocket nozzle at sea level conditions

### 2.4.2. Inlet size

The previous section considered changing afterburner size and expansion ratio of the core rocket engine while keeping inlet frontal area at a constant value and having the afterburner exactly straight (with no convergence or divergence). However, if one of the inlet cross-section areas, namely  $A_4$ , is changed, this is not necessarily the case and was explored in the survey. In this case only divergent afterburners were considered because convergent geometry suffers from huge performance losses at take-off conditions due to forcing a choke point and, as a consequence, slowing down the flow in the afterburner.

Different inlets were considered, all of them were symmetric with a throat area equal to 70% of the frontal area — a value which was found to be suitable due to a need of facilitating oblique shock wave in front of the inlet. The most important results are presented in figure 2.17. This plot shows a slight dependence of specific impulse on inlet area, positive for low Mach numbers and negative for high Mach numbers. This situation, however, is different when considering altitude of 5 km — see figure 2.18. Especially in the cases when the core rocket operates fuel-rich it is beneficial to have an inlet as large as possible. Therefore, no trade-off needed to be made here and  $A_1 = 0.005 \text{ m}^2$  was chosen to have the largest possible inlet with no convergence of the afterburner. It is worth mentioning, however, that at very large speeds at low altitudes this inlet may run into unstart problems. This has to be avoided in the trajectory design.

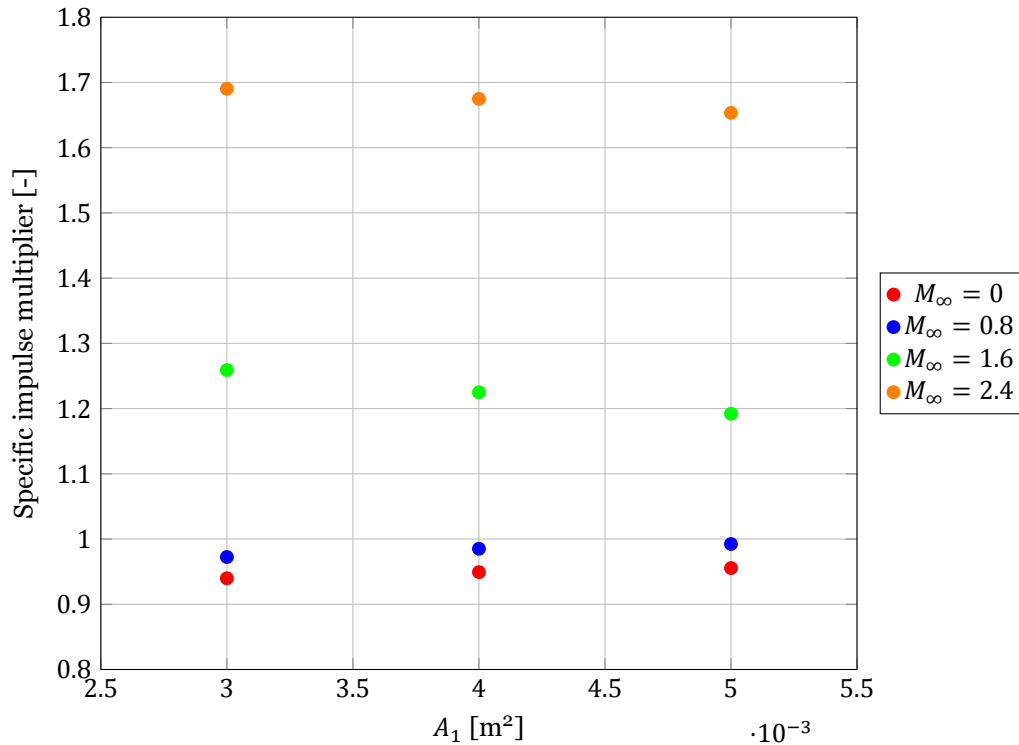


Figure 2.17: Plot of specific impulse multiplier (compared to rocket-only propulsion) against inlet frontal area for different free stream Mach numbers at sea level conditions

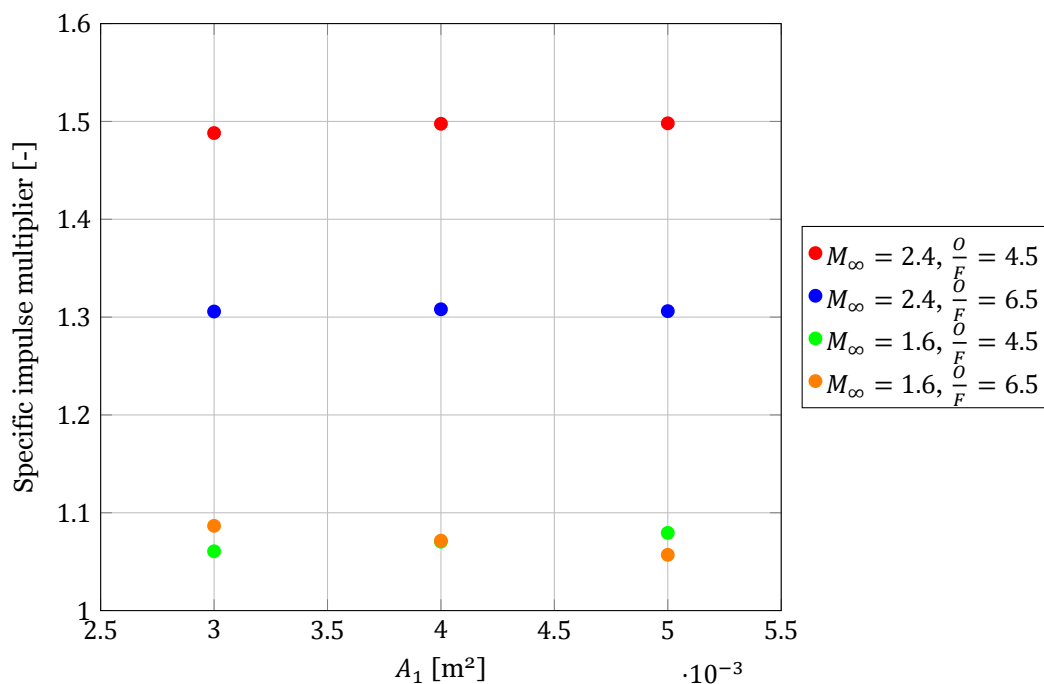


Figure 2.18: Plot of specific impulse multiplier (compared to rocket-only propulsion) against inlet frontal area for different free stream Mach numbers and oxidizer-fuel ratios of the core rocket at 5 km altitude

### 2.4.3. Final design results

The aforementioned design decisions led to choosing one final design for further stages. Its parameters are presented in table 2.3. This engine layout was then thoroughly analysed at different flight conditions to identify interesting cases. Figures 2.19 and 2.20 present major characteristics of this design in a condensed form. They show dependence of performance on Mach number, altitude and oxidizer-fuel ratio of the core rocket.

Table 2.3: Parameters of the final RBCC design

Design parameter	Final design value
$A_1$ [ $\text{m}^2$ ]	0.0050
$A_2$ [ $\text{m}^2$ ]	0.0035
$A_4$ [ $\text{m}^2$ ]	0.0049
$A_5$ [ $\text{m}^2$ ]	0.0080
$A_6$ [ $\text{m}^2$ ]	0.0088
Afterburner length [m]	0.5
Core rocket nozzle expansion ratio	5

A general trend, consistent with what is found in literature, is that RBCC engine performs best at high Mach numbers, increasing specific impulse by as much as twice. However, those gains can only be achieved in a relatively narrow layer of the atmosphere, which is below 10 km (or, alternatively, at much higher speeds). This points towards the optimal trajectory for this kind of engine being relatively flat with a pitch-up manoeuvre at the end. Another fact worth noticing is that optimal engine operation would require switching oxidizer-fuel ratio according to flight conditions. This is because operating the core rocket fuel-rich generally causes worse performance of the engine due to lower pressures in the main combustion chamber. However, if enough air is coming through the inlet, this effect can be balanced by intensive combustion in the afterburner.

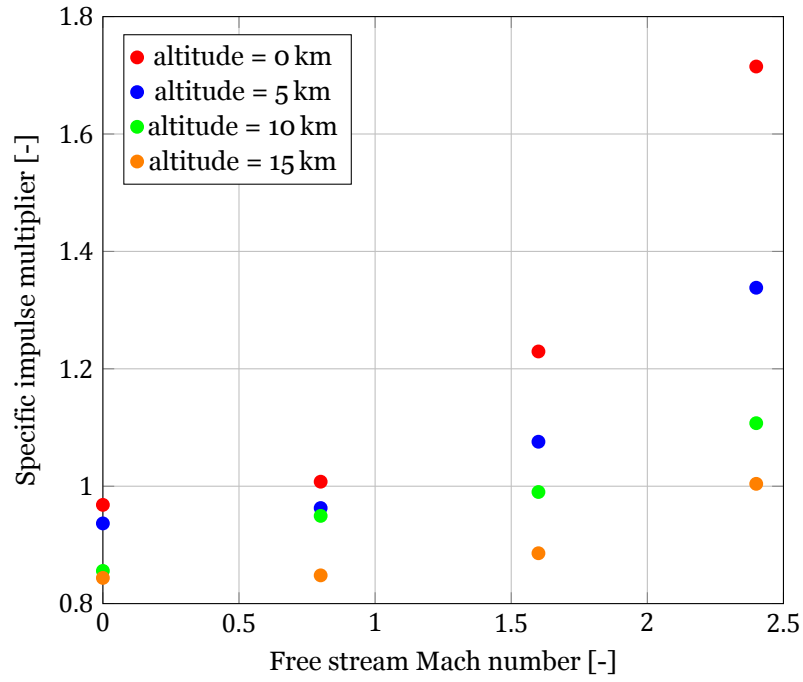


Figure 2.19: Plot of specific impulse multiplier (compared to rocket-only propulsion) against Mach number of the free stream for different altitudes with the core rocket operating at  $\frac{O}{F} = 6.5$

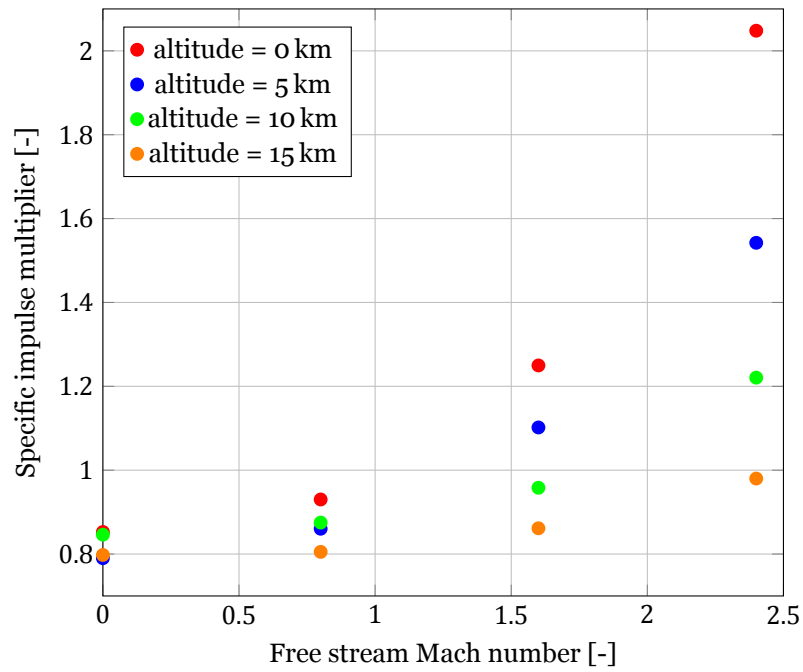


Figure 2.20: Plot of specific impulse multiplier (compared to rocket-only propulsion) against Mach number of the free stream for different altitudes with the core rocket operating at  $\frac{O}{F} = 4.5$

### 2.4.4. Shielded Primary Injection results

The shielded primary injection (SPI) is a concept introduced by Russell et al. [22], which should be able to increase performance of an RBCC engine. The idea is to inject fuel inside the core rocket engine nozzle therefore making the plume more fuel rich. At the same time the injection can be realised relatively close to the mixing plane with the inlet air and due to that create favourable conditions for combustion.

SPI can only increase performance of an RBCC engine in conditions when enough air is entering the afterburner so that added fuel can actually be burned. The clear advantage of this method compared to operating the core rocket engine fuel-rich is that there are no performance losses in the main combustion chamber. This means that total pressure and temperature of the plume stay on the same level, provided that added fuel mass flow rate is relatively small compared to that of the core rocket engine. In the development model code this was the exact method used to emulate SPI. Mass flow rate and chemical composition of the plume were changed while other parameters stayed constant.

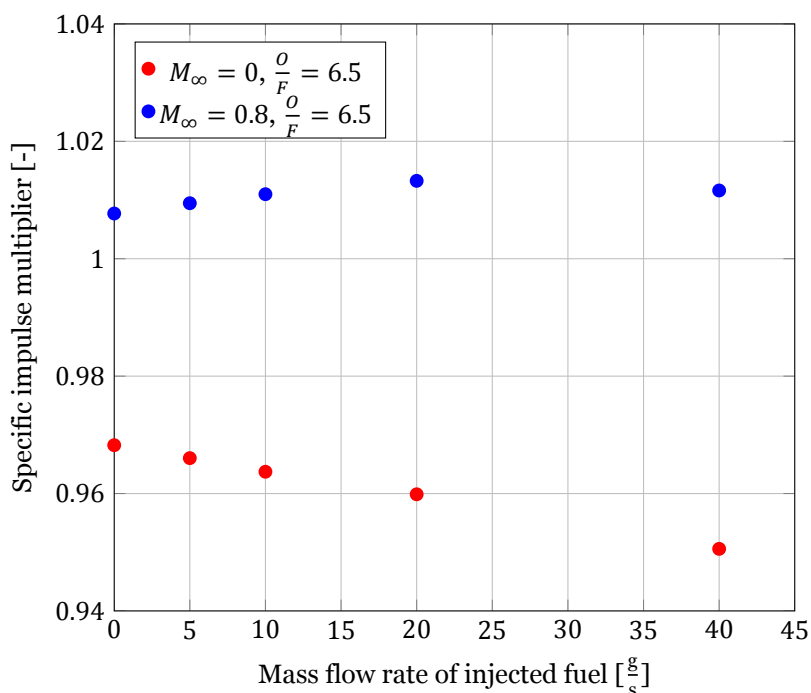


Figure 2.21: Plot of specific impulse multiplier (compared to rocket-only propulsion) against mass flow rate of additional fuel injected in the afterburner at sea level conditions for different free stream Mach numbers

Figures 2.21, 2.22 and 2.23 present results of this simulation at altitudes and Mach numbers that are likely to occur during the initial ascend phase. As visible, in some cases SPI can ensure a significant increase in specific impulse, in others it does not make a difference or causes a decrease. This generally follows the intuitive logic that additional fuel is beneficial only when the mass flow rate of air is sufficient to burn it.

In supersonic cases, SPI was simulated also for fuel-rich cases. However, only for  $M_\infty = 2.4$  this yielded noticeable gains in performance. Worth noticing is also that at 10 km altitude there is a difference in where the maximum specific impulse occurs. For a fuel-rich case this occurs for fuel mass flow rate of  $20 \frac{g}{s}$  while for  $\frac{O}{F} = 6.5$  at  $40 \frac{g}{s}$  (or even higher, outside of sampled region). This reflects the fact that at some point there is not enough air in the afterburner to burn all the combustible species in the rocket plume.

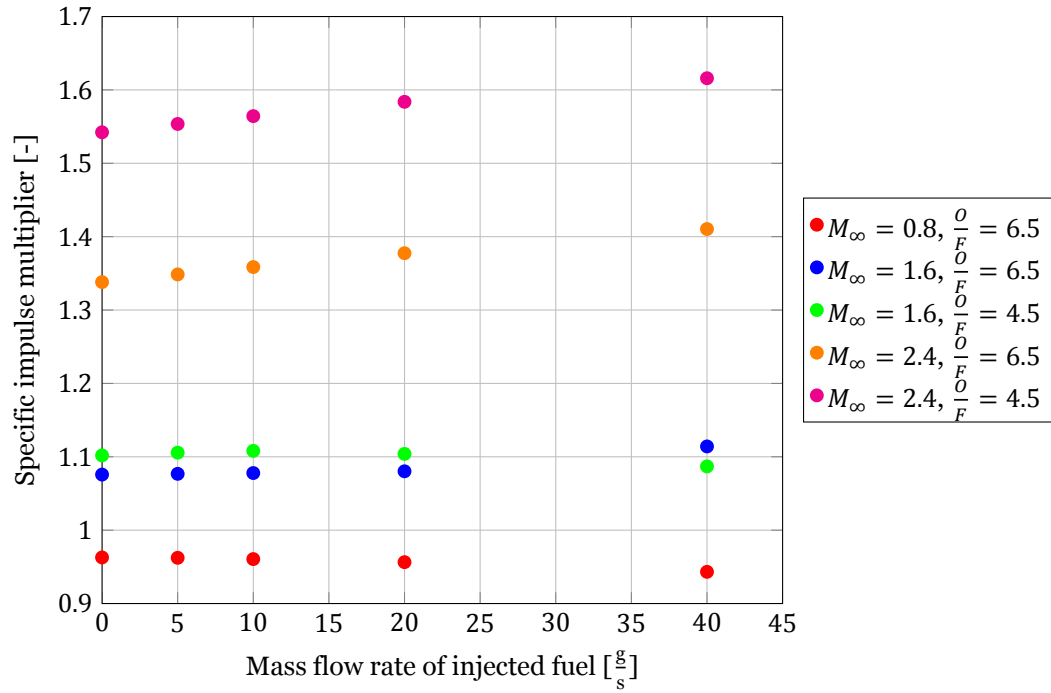


Figure 2.22: Plot of specific impulse multiplier (compared to rocket-only propulsion) against mass flow rate of additional fuel injected in the afterburner at 5 km of altitude for different free stream Mach numbers and oxidizer to fuel ratios of the core rocket

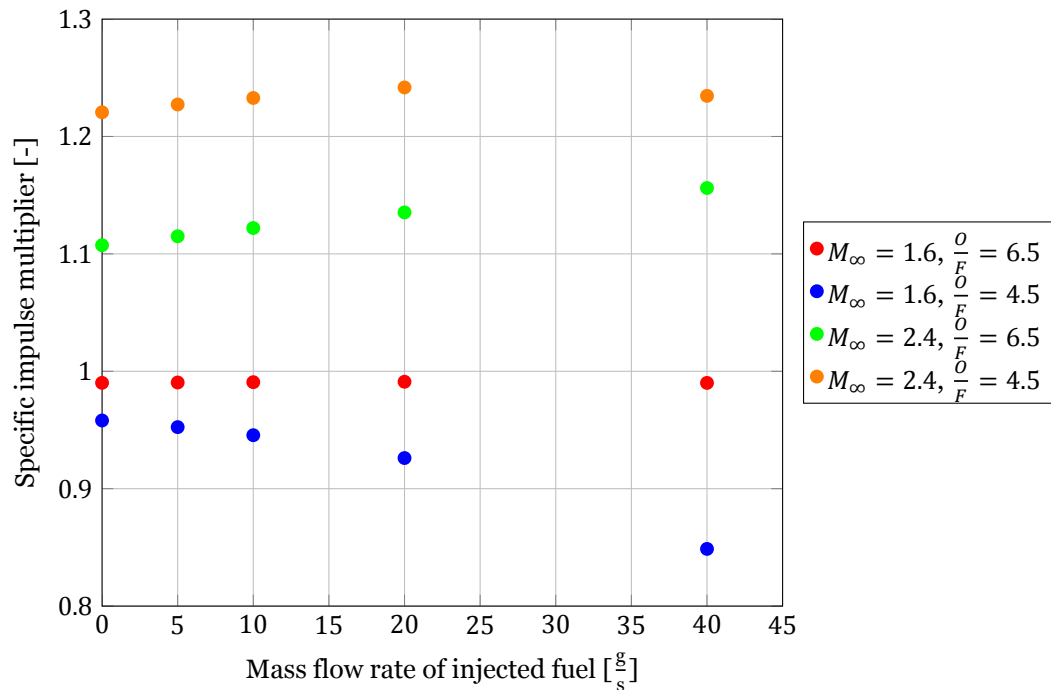


Figure 2.23: Plot of specific impulse multiplier (compared to rocket-only propulsion) against mass flow rate of additional fuel injected in the afterburner at 10 km of altitude for different free stream Mach numbers and oxidizer to fuel ratios of the core rocket

# 3

## CFD model of a chosen design

The following sections present assumptions, methodology and results of CFD modelling of the RBCC engine design identified in section 2.4. The main purpose of this analysis was to verify results of the quasi-1D model.

### 3.1. Combustion model

Undoubtedly, the most challenging part of CFD modelling was finding a right combustion model. In order to be able to simulate all cases correctly it needed to include all major species that can exist in a fuel-rich rocket plume, as well as reactions between those species and the inlet air. Additionally, in order to simulate shielded primary injection (SPI) cases, it needed to include kerosene and its combustion reactions. At the same time, due to the high complexity of CFD methods, it could not include too many reactions or species in order to not make the calculation process too computationally costly.

#### 3.1.1. Chosen model description

The final choice of the combustion model was the RP-2 (Rocket Propellant 2) skeletal model created by Wang et al. [28]. It includes 38 species and 192 reactions between them. This allows for simulating the afterburning of species from the rocket plume, as well as shielded primary injection (SPI). To assess the feasibility of using this model in CFD, a number of simple test cases with only a rocket engine were conducted. For this, and later also for RBCC cases, the model, in a form of a CHEMKIN file, was imported into the Fluent solver [1].

#### 3.1.2. Test runs setup

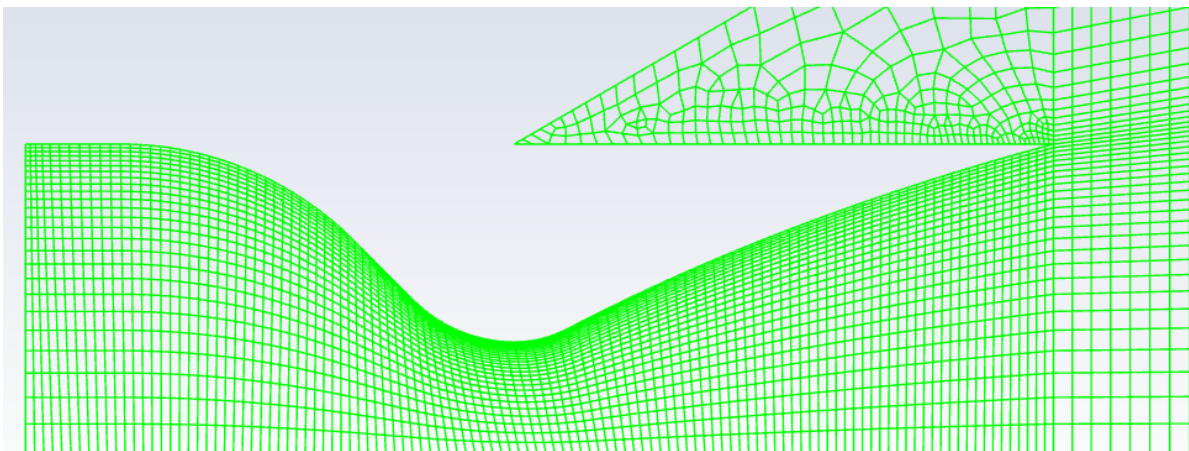


Figure 3.1: Detailed view of the nozzle in the mesh used for test runs of the combustion model

The mesh used for test runs is presented in figures 3.1 and 3.2. It is the most dense in regions where high gradients of flow parameters (such as pressure, temperature and velocity) are expected, that is in the nozzle and right in front of it. Near the nozzle wall even more elements have been used. This was done in order to achieve  $Y^+$  values presented in figure 3.3, which even in the highest peak are adequate for the used turbulence model. Far away from the nozzle axis quality of the mesh could be lowered because no important phenomena were going to happen there.

The boundary conditions that are used are visible in figure 3.2. The nozzle wall is indicated in gray, the pressure outlet used for simulating sea level conditions far from the nozzle exit in red, the axis of symmetry of the flow field in yellow and the pressure inlet that simulates conditions at the inlet of the nozzle in blue. The chemical composition at this pressure inlet was set using information from Rocket Propulsion Analysis Program [21]. It included the following species: molecular hydrogen, carbon monoxide, carbon dioxide, molecular oxygen, hydroxyl radical and water vapour.

The ideal gas law was used for density calculation. The energy equation was enabled to compute the temperature field in the flow. The turbulence model was realizable  $k - \varepsilon$  with the Standard Wall Function, which is a recommended choice for very similar supersonic flows that occur in jet engines as proved by Bulat [3]. A convergence criterion of  $10^{-3}$  was used, which is typical for Fluent calculations.

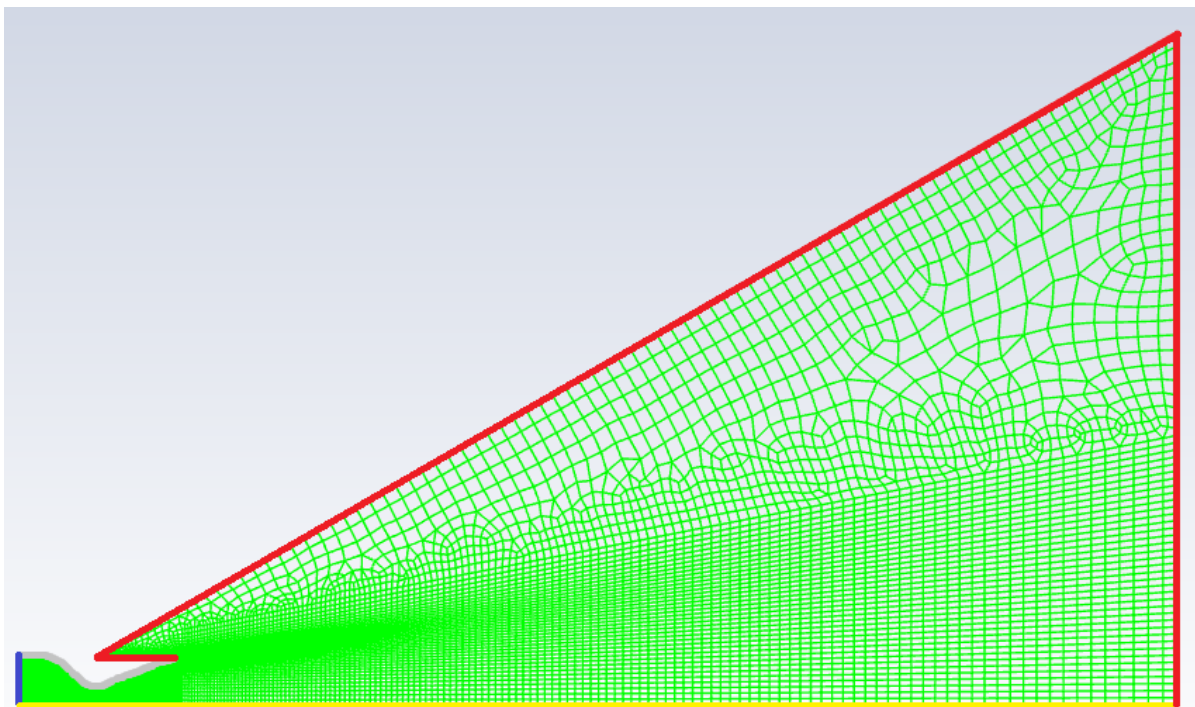


Figure 3.2: Overall view of the mesh used for test runs of the combustion model

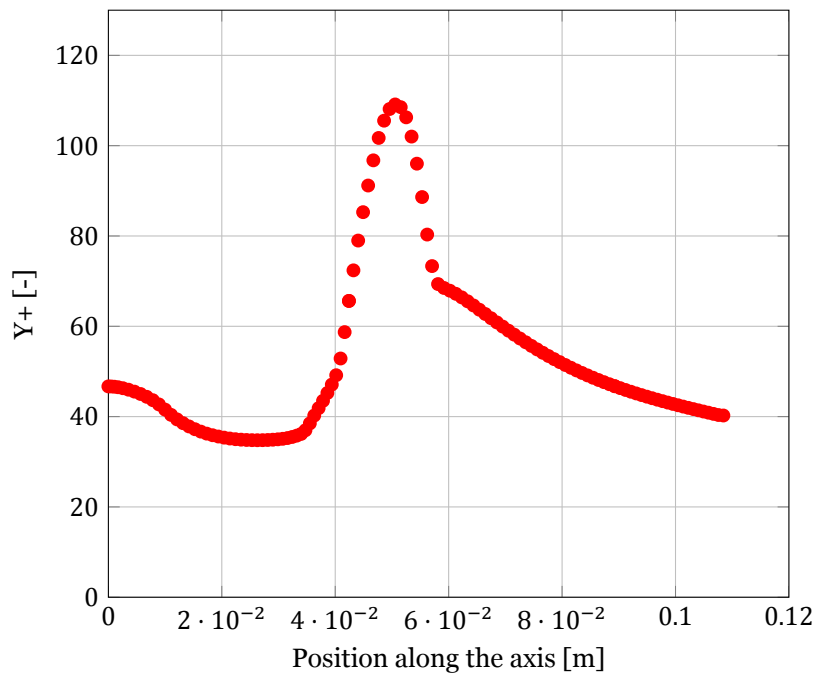


Figure 3.3: Plot of value of  $Y^+$  on the nozzle wall against position along the axis for an exemplary rocket-only case

### 3.1.3. Test runs results

The most important outcome of the test runs is that the solution could converge within reasonable time and number of iterations (around 2000–3000). The obtained solutions also agree sufficiently with results from Rocket Propulsion Analysis Program [21], as presented in figures 3.4 and 3.5. However, the CFD model predicts larger carbon monoxide mass fractions and, as a consequence, smaller carbon dioxide ones. This is explained because the used equilibrium chemistry models in RPA do not take into account mixing effects, only temperature influence on dissociation rates.

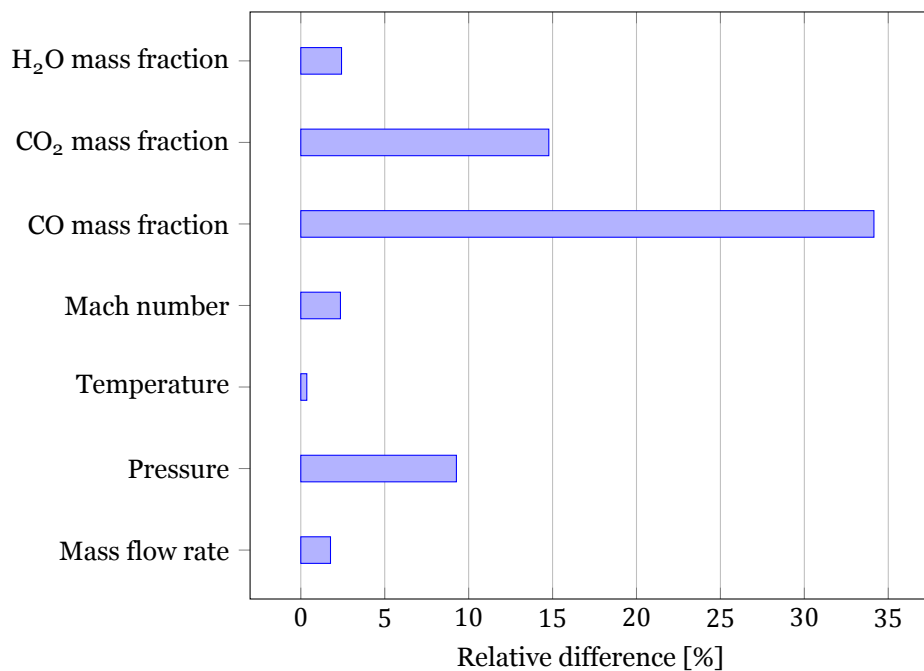


Figure 3.4: Bar graph of relative differences between nozzle exit parameters calculated by Rocket Propulsion Analysis Program [21] and by CFD test run for oxidizer to fuel ratio of 6.5

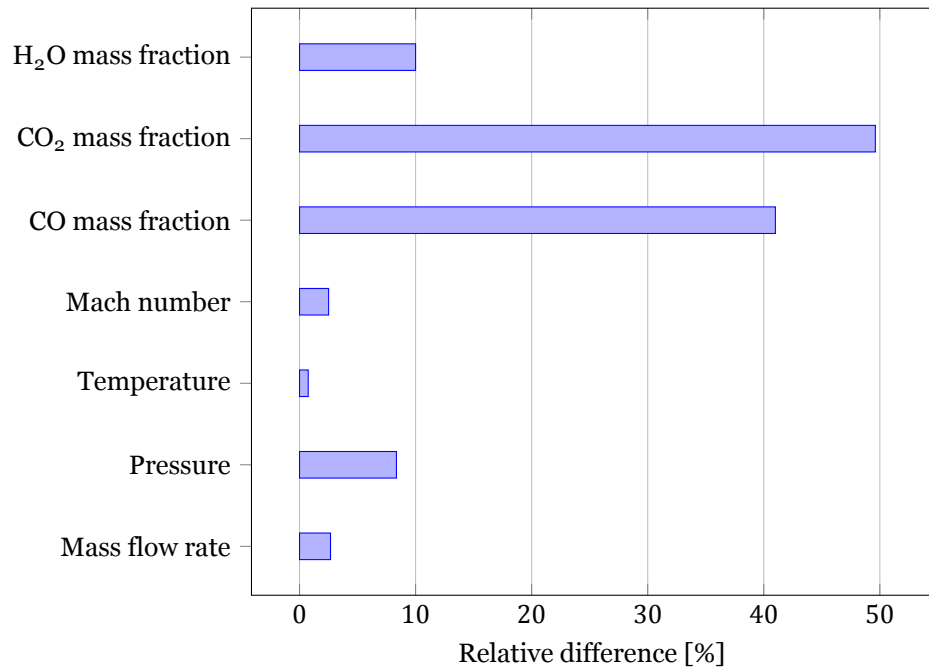


Figure 3.5: Bar graph of relative differences between nozzle exit parameters calculated by Rocket Propulsion Analysis Program [21] and by CFD test run for oxidizer to fuel ratio of 4.5

Qualitative comparison of flow fields also showed agreement with expectations. For example, comparing figures 3.6 and 3.7 reveals that Mach number at the exit of the nozzle is the same for both cases. It is because of the lower total pressure of the exhaust under fuel-rich operation, that in the second case the plume is shorter and the effect of overexpansion is larger than in a typical mode of operation.

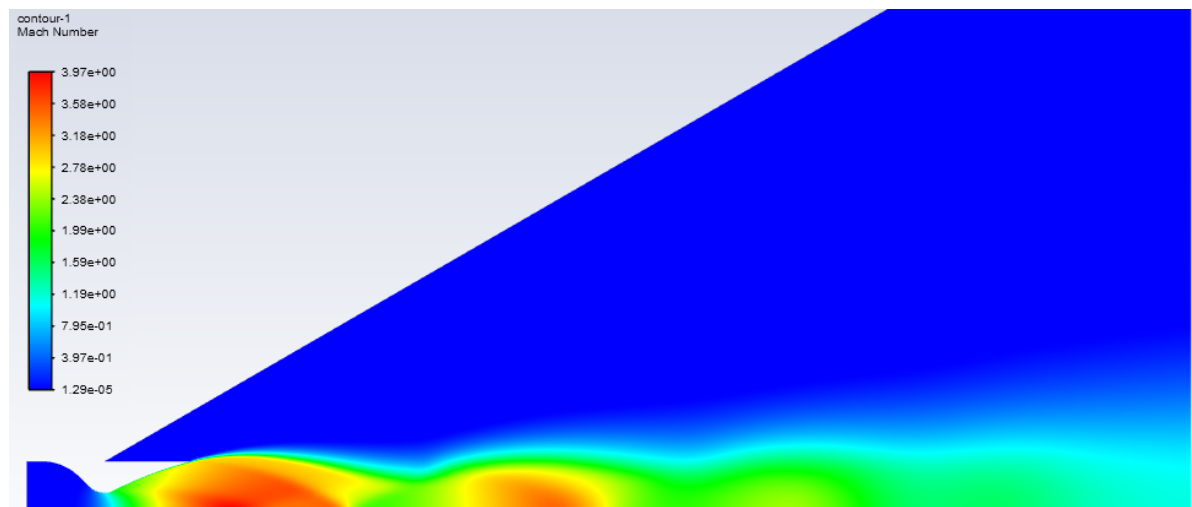


Figure 3.6: Mach number contours of the rocket-only case with  $\frac{O}{F} = 6.5$

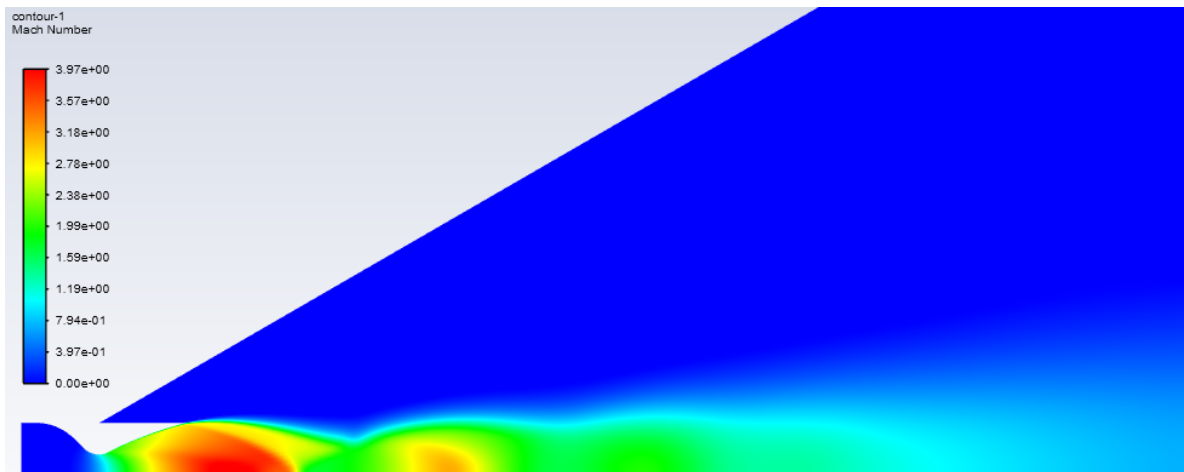


Figure 3.7: Mach number contours of the rocket-only case with  $\frac{O}{F} = 4.5$

Another important outcome of the test runs is a confirmation of the reaction and species transport mechanisms working properly. This can be observed on the contour maps of species mass fraction and static temperature. Comparing figures 3.8 and 3.9 it can be seen that in both cases molecular hydrogen is present in the plume but there is much more of it when the engine is operating fuel-rich. Quantitatively, the mass fraction of molecular hydrogen near the nozzle exit at an oxidizer to fuel ratio of 6.5 is 0.6% and at 4.5 it is 2.09%. In both cases though, mass fraction of hydrogen within the plume is dropping to nearly 0% at some point behind the nozzle. This is where the reaction zone reaches the axis of the flow field. It can be confirmed when looking at temperature contours (figures 3.10 and 3.11). There is a spike in static temperature correlating with a drop in hydrogen mass fraction.

Worth noting is also the fact that despite a lower total temperature of the rocket engine plume initially in the fuel-rich case, it actually reaches higher temperatures near the end of the flow field. This is, of course, a result of the afterburning reaction, which is much more intensive in the fuel-rich case.

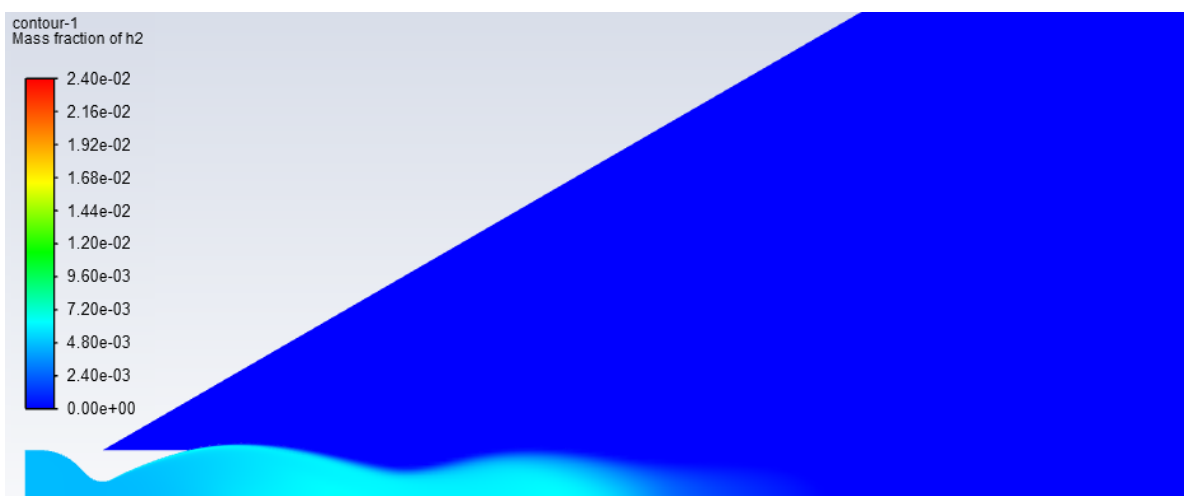


Figure 3.8: Molecular hydrogen mass fraction contours of the rocket-only case with  $\frac{O}{F} = 6.5$

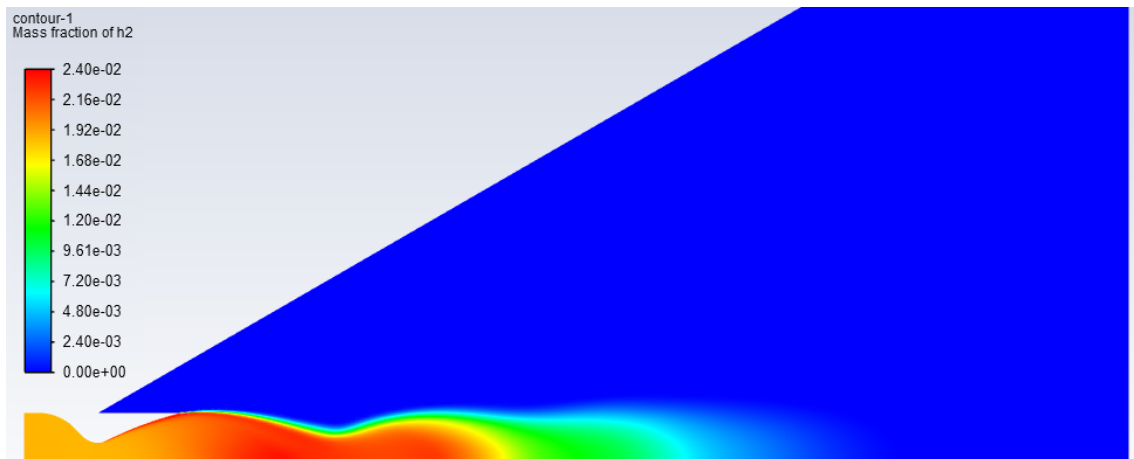


Figure 3.9: Molecular hydrogen mass fraction contours of the rocket-only case with  $\frac{O}{F} = 4.5$

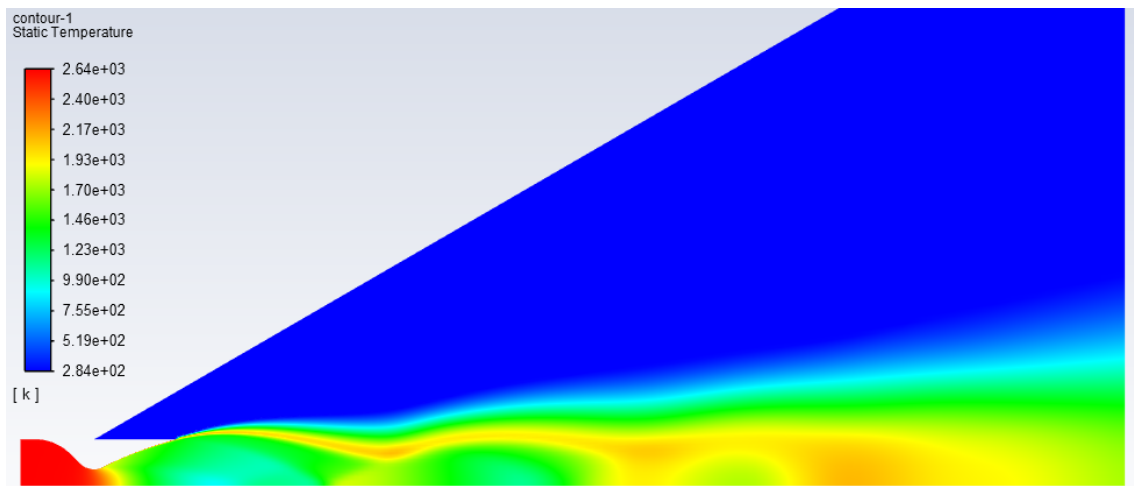


Figure 3.10: Static temperature contours of the rocket-only case with  $\frac{O}{F} = 6.5$

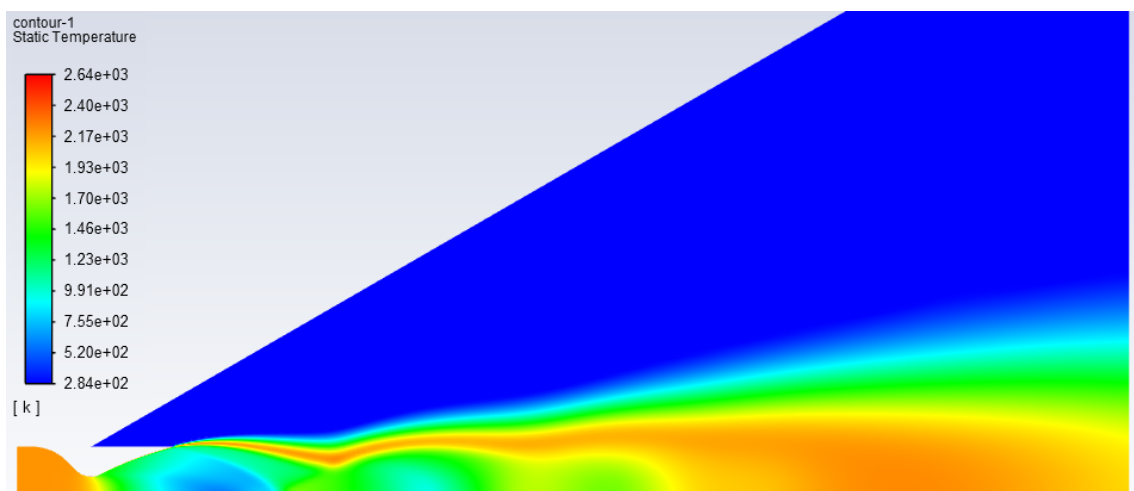


Figure 3.11: Static temperature contours of the rocket-only case with  $\frac{O}{F} = 4.5$

## 3.2. Geometry and mesh

The geometry of the considered RBCC engine was chosen through a survey of different designs as presented in section 2.4. Based on this, the geometry and mesh as presented in figure 3.12 was created. As in the test runs, that included only the rocket engine, the flow field was much larger than the engine to facilitate far-field boundary conditions. Those, for the majority of cases, were: velocity inlet on the left border, pressure far field on the top border and pressure outlet on the right border. Only for the static sea level conditions all of them were changed to pressure outlets. Values needed for the aforementioned boundary conditions were set according to the Standard Atmosphere [26]. Other boundary conditions can be easily seen in figure 3.13 and included the axis of the flow field (yellow) and the pressure inlet (blue) that was placed at the throat of the core rocket engine. The latter was changed compared to test runs in the hope of accelerating convergence of calculations. Additionally, for SPI cases, a mass flow inlet was defined in the core rocket engine nozzle to simulate a fuel injector.

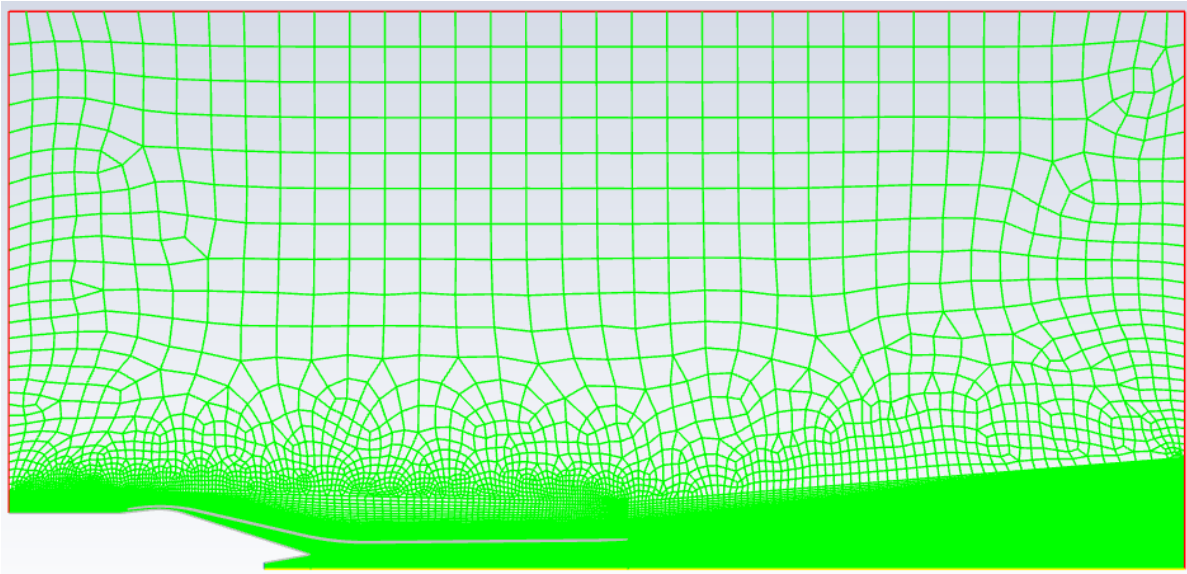


Figure 3.12: Mesh used for simulating RBCC cases



Figure 3.13: Zoomed-in view of the geometry used for simulating RBCC cases

Figures 3.14, 3.15 and 3.16 present in detail the most important parts of the geometry – the inlet, the mixing point and the nozzle respectively. They are naturally also characterized by a much denser mesh compared to the external parts of the flow field because larger pressure, temperature and velocity gradients were expected there.

The inlet design is relatively simple, with a place for a single oblique shock wave, which was calculated for flight Mach number of 2.4 – relatively small, to facilitate low speeds of the Mk-II *Aurora* but large enough to make sure that the inlet can be started at those conditions. Worth mentioning here is that there is a 500 mm tube in front of the inlet that simulates a part of the fuselage and allows for the buildup of the boundary layer. At later stages of the design, integration of the inlet with the existing airframe would have to be investigated in greater detail as this can significantly affect inlet performance.

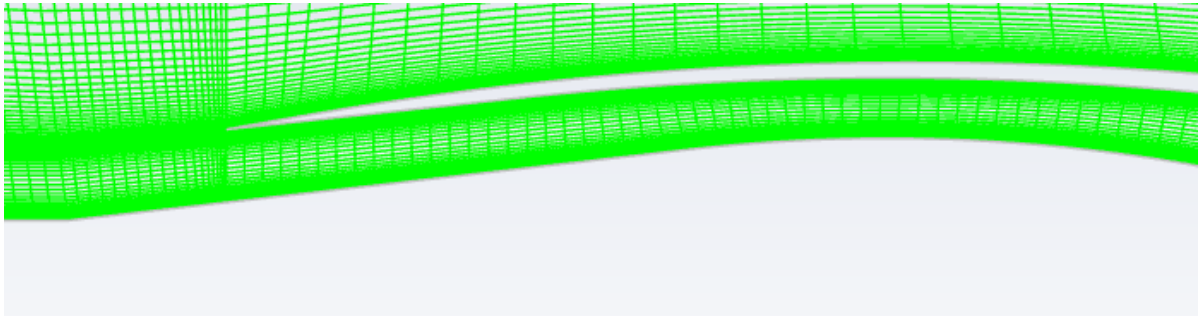


Figure 3.14: Mesh used for simulating RBCC cases — detailed view of the inlet

The mixing point area is also characterised by a relatively simple geometry. A decision was made to mostly use straight lines. A conical nozzle was assumed for the core rocket engine. Similarly, the inlet diffuser has straight walls and it is situated at an angle to the axis of the engine. This should add a radial component to inlet air velocity thus inducing better mixing. The mesh in this area is denser not only near the walls but also at a supposed mixing location as large temperature gradients were expected there.

Lastly, the RBCC engine has a low expansion ratio, short conical nozzle. The divergence half-angle was chosen to be  $2.5^\circ$  in order to minimize exit losses.

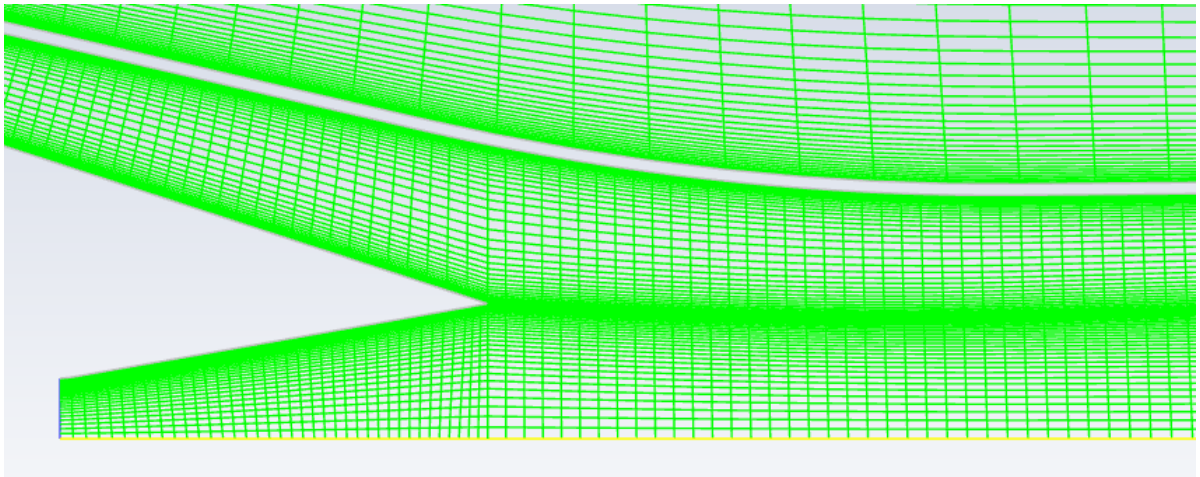


Figure 3.15: Mesh used for simulating RBCC cases — detailed view of the mixing point

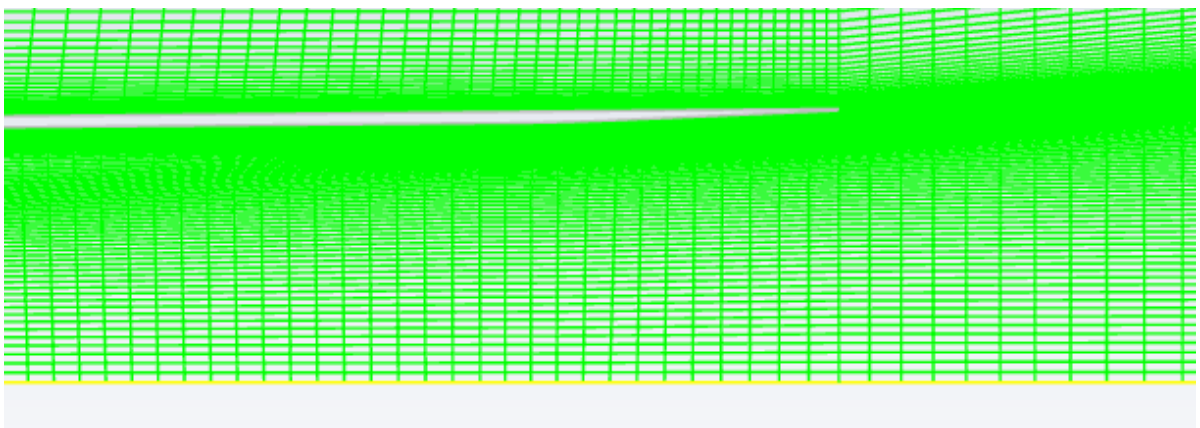


Figure 3.16: Mesh used for simulating RBCC cases — detailed view of the RBCC nozzle

Overall, the mesh used was adequate for the purpose of the simulation.  $Y^+$  values on the walls, presented in figure 3.17, confirm that at some places it could even be coarser and still reflect the boundary layer behaviour. However, due to shock waves requiring very dense mesh and appearing in many places in the flow, the number of elements was not reduced.

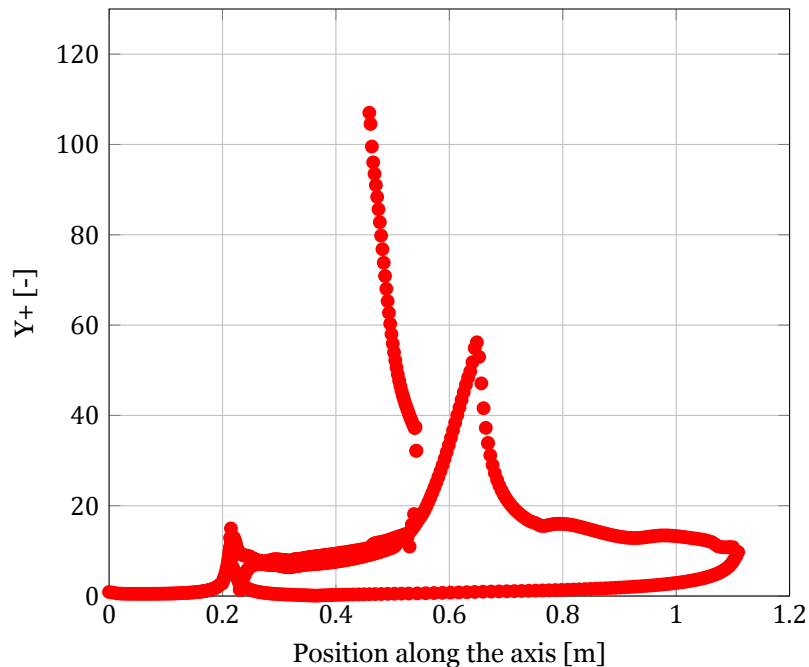


Figure 3.17: Plot of value of  $Y^+$  on the RBCC engine's walls against position along the axis for an exemplary case

### 3.3. Simulated cases matrix

Naturally, the CFD model could be used at any flight condition. However, due to its computational cost, the number of cases that could realistically be processed was rather small. That is why a case matrix was prepared. It is presented in table 3.1 and was constructed in a way to include realistic flight conditions in the lower atmosphere. Those cases are the most interesting from the perspective of checking the results of the quasi-1D model. In the upper atmosphere an RBCC engine operates practically as a rocket with a high expansion ratio nozzle. The Mach number range was also chosen to reflect achievable air speeds and to match cases calculated with a quasi-1D model beforehand.

The case matrix presents which oxidizer to fuel ratios of the core rocket were considered in given flight conditions. Additionally, for some cases the shielded primary injection concept was to be tested, that is indicated with '+ SPI' next to a given oxidizer to fuel ratio.

All in all, a total of 18 cases were evaluated. For cases where significant air flow was expected, they were tried for both  $\frac{O}{F} = 6.5$  and  $\frac{O}{F} = 4.5$  as according to results from section 2.4.3 the fuel-rich case could provide better performance than the standard one. Additionally, SPI was tested in 4 flight conditions, out of which 2 should have yielded significant gains in specific impulse compared to non-SPI cases. To further differentiate the sampled conditions,  $40 \frac{g}{s}$  fuel mass flow rate was used at 5 km and  $20 \frac{g}{s}$  at 10 km (see figures 2.22 and 2.23 for expected performance gains).

Table 3.1: Case matrix for the CFD model

		altitude			
		0 km	5 km	10 km	15 km
$M_\infty$	0	$\frac{O}{F} = 6.5$	X	X	X
	0,8	$\frac{O}{F} = 6.5/4.5$	$\frac{O}{F} = 6.5/4.5$	X	X
	1,6	X	$\frac{O}{F} = 6.5 + \text{SPI}/4.5$	$\frac{O}{F} = 6.5 + \text{SPI}/4.5$	X
	2,4	X	$\frac{O}{F} = 6.5 + \text{SPI}/4.5$	$\frac{O}{F} = 6.5 + \text{SPI}/4.5$	$\frac{O}{F} = 6.5$

### 3.4. Results

All cases within the case matrix did converge. The main convergence criterion was for the mass flow rates through control surfaces in the engine to match. Those control surfaces are presented in figure 3.18. Mass flow rates through surfaces of the same colour had to be the same. Additionally, mass flow rates through blue and red surfaces had to sum up to the one through the green surface. Practically, the solution was considered converged when those conditions were fulfilled with less than 5% error.

Such a criterion was necessary to ensure that the steady state solution was obtained. This, in turn, guaranteed that thrust equation could be used, as it takes as an input mass-averaged exhaust parameters of the flow and mass flow rate of the air coming through the inlet.

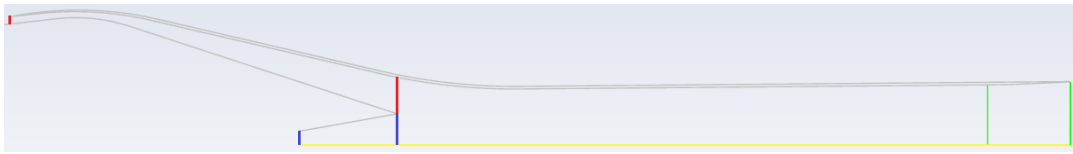


Figure 3.18: Control surfaces used for convergence checks

The following sections present the most important results of the CFD model that indicate further areas of research and development of this RBCC engine. Furthermore, section 3.4.5 summarises all cases and their results while comparing them to the outcomes of the quasi-1D model and section 3.4.6 discusses what the results mean for the development of the RBCC engine for Mk-II *Aurora*.

#### 3.4.1. Take-off conditions

The first results were obtained for static sea level conditions and they are also considered the most important. The quasi-1D model has shown a loss of performance in this case compared to the non-RBCC configuration. At the same time, the flow field in this case shows a lot of features that are also present in other conditions.

Figure 3.19 presents contours of Mach numbers within the afterburner. It shows that although some mixing does occur, the plume from the engine is clearly distinct from the air that surrounds it. This is understandable because the only mechanism of momentum exchange between those streams is viscous interaction in the shear layer between them. Worth noticing here is that the flow does not change significantly after reaching the middle of the afterburner. This hints towards the conclusion that further lengthening of the tube would not result in much better mixing. In this case the afterburner could even be shortened. However, this additional length proves to be useful when supersonic speeds are reached by the vehicle.

Another interesting fact to notice is that the flow does not separate in the RBCC nozzle, which is an accurate prediction made by the quasi-1D model. As expected, however, the exit pressure is lower than ambient causing the flow to compress right after exiting. The overall performance in this case was excellently predicted by the quasi-1D model with the estimation of thrust within 2.1% and the specific impulse within 0.7% of the value from the CFD simulation.

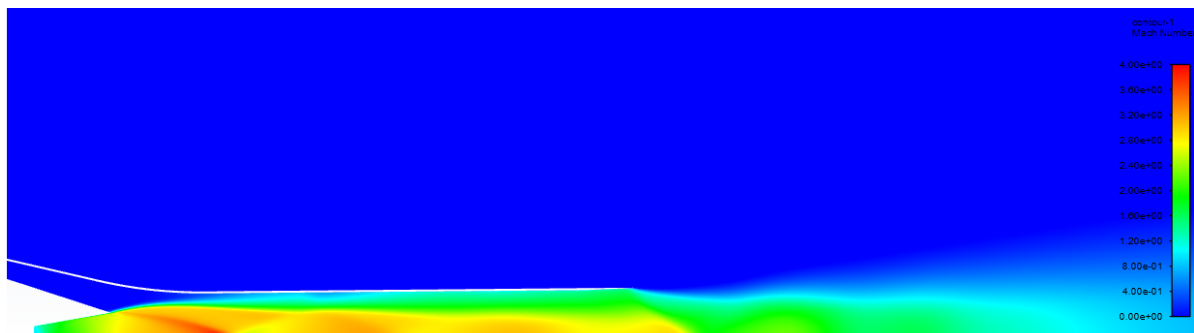


Figure 3.19: Mach number contours for static sea level conditions

Quantification of combustion taking place in the afterburner is also something that was looked into when evaluating results. This is best done looking at the mass fraction of combustible products present in the rocket plume, such as molecular hydrogen shown in figure 3.20. The amount of molecular hydrogen in the flow reduces within the afterburner and reaches almost 0 right outside of it. Of course, at oxidizer to fuel ratio of 6.5 there is not a lot of combustible products in the plume. However, from this contour map it can be concluded that noticeable combustion actually does happen within the afterburner and, as described in section 3.4.2, it does increase the temperature of the flow. This effect is comparable with the situation from the rocket-only case presented in figures 3.8 and 3.10. However, the flow field looks differently due to the afterburner constraining the airflow.

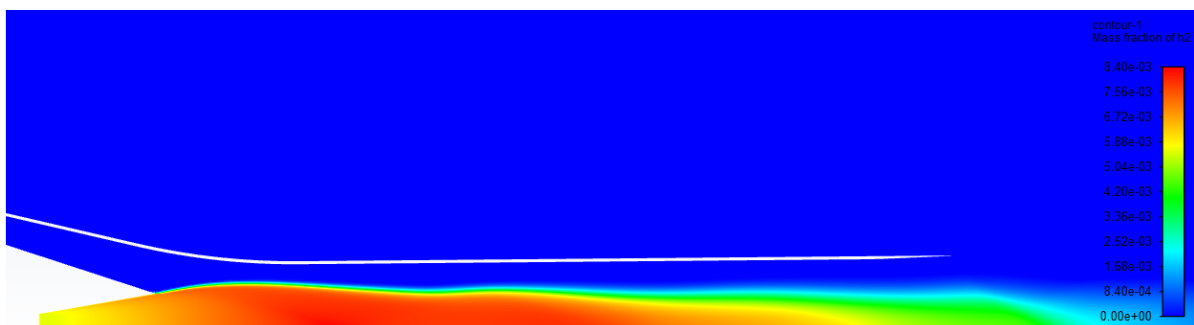


Figure 3.20: Molecular hydrogen mass fraction contours for static sea level conditions

### 3.4.2. Afterburner temperature distribution

The static temperature inside the afterburner is a good indicator of where and how intensive combustion takes place. However, it is also an important parameter for further thermal analysis of the engine. It was expected that the inlet air would act as a film coolant within the afterburner shielding walls from the highest temperatures in the flow. This proved to not be true for all cases. Specifically, when the air flow is limited such as at take-off conditions (see figure 3.21) the zone of high temperatures created by the afterburning process reaches the wall around the middle of the afterburner. This is a real issue as a combination of high temperatures (around 2000 K) and high velocity flow creates conditions for very high heat flow into the wall.

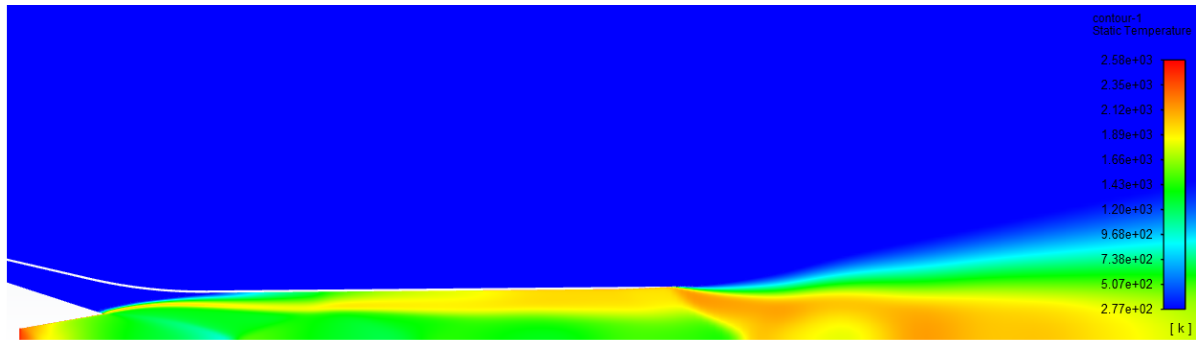


Figure 3.21: Static temperature contours for static sea level conditions

Figures 3.22 and 3.23, however, provide evidence that the inlet air can act as a film coolant in supersonic cases. This is because then the air mass flow rate is sufficient to actually shield the wall from high temperatures and keep the reaction zone at the shear layer between the rocket plume and inlet air.

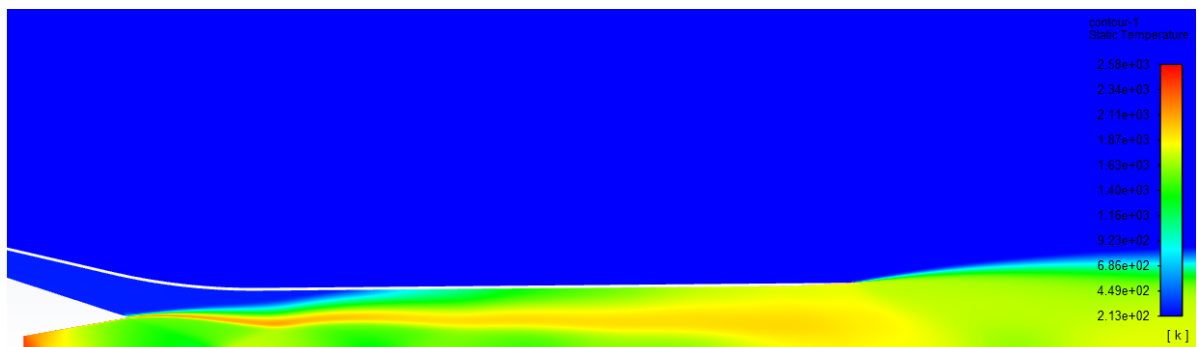


Figure 3.22: Static temperature contours for  $M_\infty = 1.6$  and altitude of 5 km

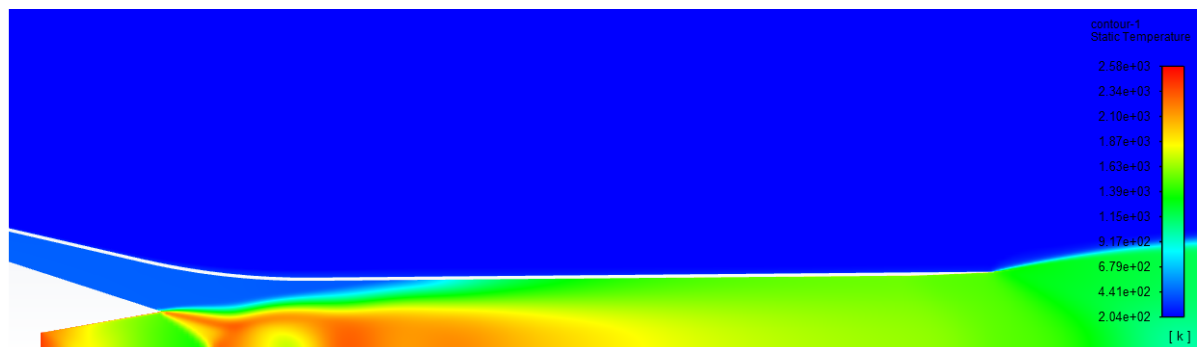


Figure 3.23: Static temperature contours for  $M_\infty = 2.4$  and altitude of 5 km

### 3.4.3. Inlet behaviour

Another important aspect for evaluating the RBCC performance is the inlet behaviour under different flight conditions and engine settings. For the designed engine, the driving regime for inlet design was the supersonic regime, specifically free stream Mach number 2.4. In those conditions the inlet should be started and a single oblique shock wave should be present in front of it. This was confirmed by the CFD analysis as presented in figure 3.24. However, when at these conditions SPI concept was tested, the inlet got to the verge of unstart as presented in figure 3.25. This is caused by the increased back pressure of the afterburner due to the added fuel. Behaviour like this needs to be further characterised in the next stages of the design to ensure that unstart does not occur.

What is worth mentioning here is that the designed inlet is relatively simple and unfortunately does show poor pressure recovery (presented in figure 2.13 and used in the quasi-1D model). At Mach 2.4

it only recovers a little more than 50% of total pressure of the free stream compared to expected 80%. In the next iterations this would have to be corrected with a more complicated inlet geometry that would create multiple oblique shock waves slowing down the flow more gradually. For the purpose of comparing results, however, pressure recovery calculated through CFD methods was used as an input to quasi-1D model.

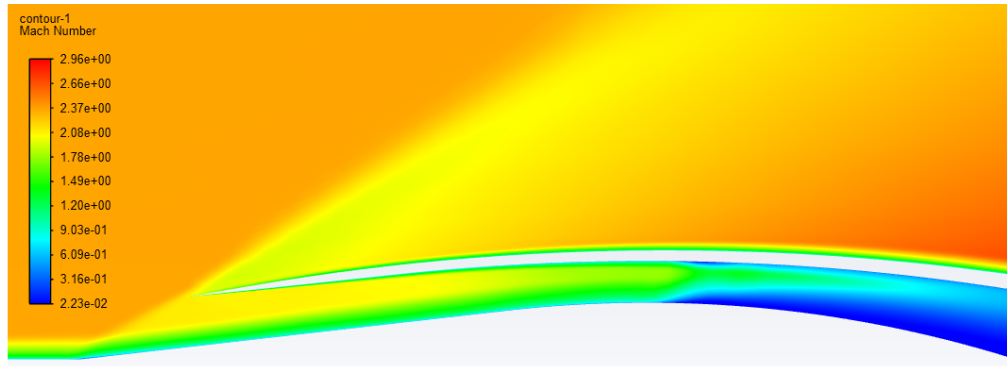


Figure 3.24: Inlet Mach number contours for  $M_\infty = 2.4$  and altitude of 5 km

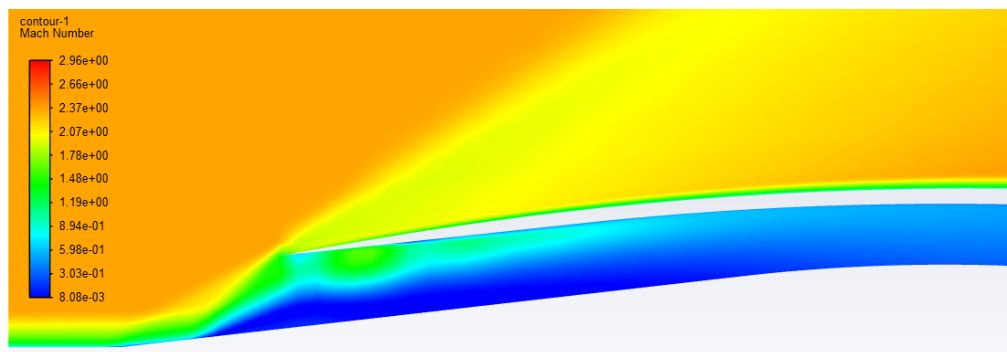


Figure 3.25: Inlet Mach number contours for  $M_\infty = 2.4$  and altitude of 5 km with shielded primary injection active

When it comes to off-design conditions, the inlet also behaved as expected. It can be seen in figure 3.26, for subsonic flight Mach number the inlet stays subsonic with supersonic speeds reached only above it. This leads to the situation where the mass flow rate through the inlet depends on back pressure of the afterburner. Similarly, at lower supersonic speeds like in figure 3.27 the inlet is typically unstarted meaning that the flow goes through one or more shock waves in front of the inlet and at its entry is subsonic.

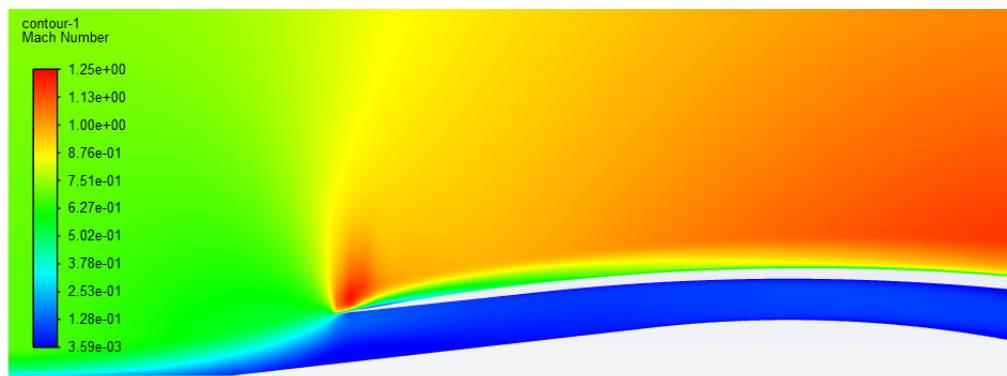


Figure 3.26: Inlet Mach number contours for  $M_\infty = 0.8$  and altitude of 5 km

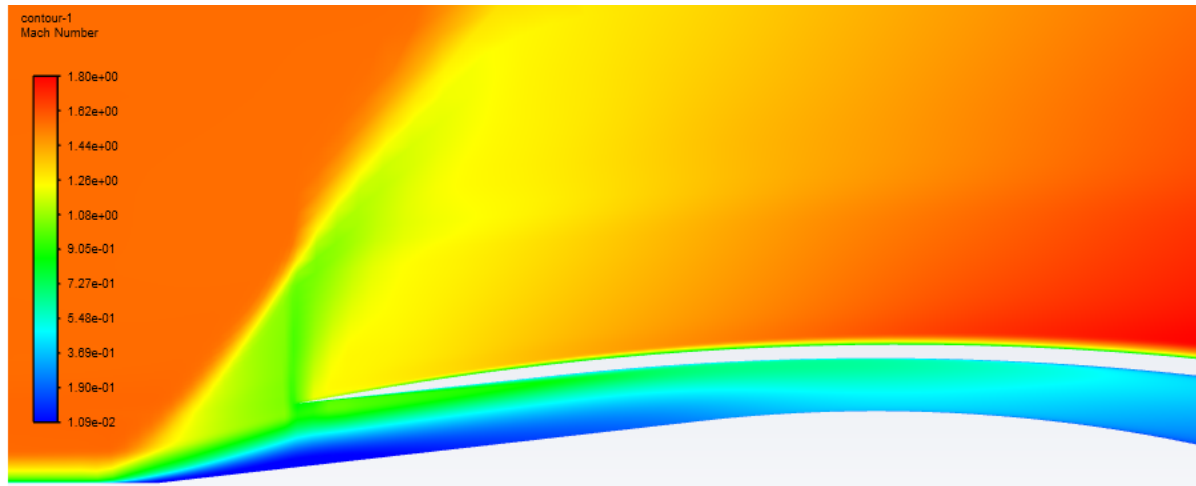


Figure 3.27: Inlet Mach number contours for  $M_\infty = 1.6$  and altitude of 5 km

### 3.4.4. Shielded Primary Injection

SPI was tested in 4 different flight conditions with 2 different mass flow rates of injected fuel. Overall, as described in section 2.4.4, gains in specific impulse were expected in 3 out of 4 of those cases compared to rocket-only propulsion. Quantitatively, those gains ranged from 11.4% to 41%. However, taking into account worse inlet efficiency it turned out that significant gains (around 21%) were only predicted for the case at 5 km altitude and a free stream Mach number 2.4. This turned out to be confirmed by the CFD analysis and the specific impulse predicted was within 0.47% of that calculated from the CFD. In other cases the prediction turned out to be less accurate but remained within between 2.5% to 6.4% of the CFD result. This can possibly be attributed to a lack of mixing effects taken into account because the case with the best prediction has very high airflow and, as a consequence, air to fuel ratio in the afterburner. This, in turn, causes fuel to burn easier, close to how it happens in the equilibrium chemistry model.

Worth mentioning here is also the way that fuel injection was introduced in the CFD analysis. This is best visible in figure 3.28, which shows contours of molecular hydrogen mass fraction near the fuel injector. This contour map visualises how fuel got spread in the afterburner. Molecular hydrogen is chosen over kerosene because the latter gets broken up into other species very quickly in given temperatures and thus does not give a clear picture of the injection. From this figure it is visible that the injector was placed near the end of the nozzle to achieve good conditions for mixing with inlet air. This location was chosen based on paper from Russell et al. [22], in which placement of the injector was investigated. However, since cases considered for testing SPI are supersonic, the pressure of the inlet air is quite large and causes fuel to be pushed towards the axis of the afterburner. This may cause some of the fuel to remain unburned. Further studies will be needed on this phenomenon if the SPI concept is to be implemented.

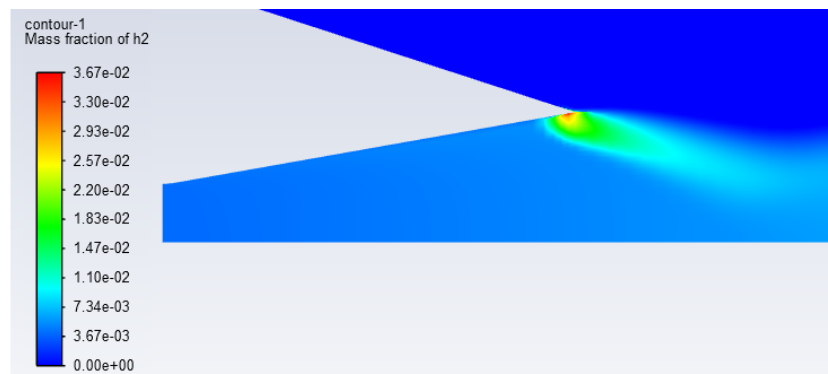


Figure 3.28: Molecular hydrogen mass fraction contours for  $M_\infty = 2.4$  and altitude of 5 km with shielded primary injection active

Lastly, a comparison of figures 3.23 and 3.29 can be made in order to show how SPI increases the afterburning intensity. The high temperature region spreads much further from the nozzle when SPI is active causing the average temperature at the end of the afterburner to be much higher than when fuel is not injected.

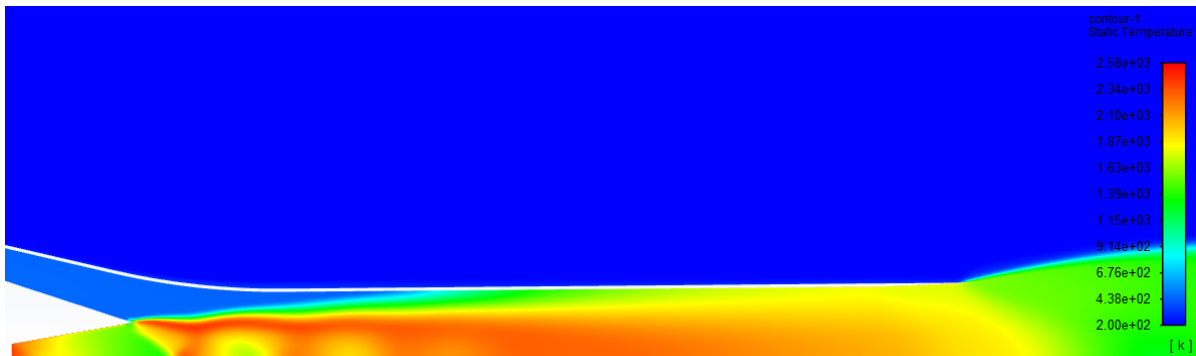


Figure 3.29: Static temperature contours for  $M_\infty = 2.4$  and altitude of 5 km with shielded primary injection active

### 3.4.5. Comparison with quasi-1D model

The primary goal of the CFD analysis is to verify whether the quasi-1D model's results were correct. This section presents the differences in obtained results and concludes with an assessment if the quasi-1D model is suitable as an initial design tool. Table 3.2 presents all evaluated cases with their numbers.

Table 3.2: List of cases with numbering

Case number	Altitude [km]	$M_\infty$ [-]	$\frac{O}{F}$ [-]	SPI — fuel mass flow rate [ $\frac{g}{s}$ ]
1	0	0	6.5	0
2	0	0.8	6.5	0
3	0	0.8	4.5	0
4	5	0.8	6.5	0
5	5	1.6	6.5	0
6	5	2.4	6.5	0
7	5	1.6	6.5	40
8	5	2.4	6.5	40
9	5	0.8	4.5	0
10	5	1.6	4.5	0
11	5	2.4	4.5	0
12	10	1.6	6.5	0
13	10	2.4	6.5	0
14	10	1.6	6.5	20
15	10	2.4	6.5	20
16	10	1.6	4.5	0
17	10	2.4	4.5	0
18	15	2.4	6.5	0

Firstly, the total temperatures and pressures at the end of the afterburner were compared. The results of this comparison are presented in figures 3.30 and 3.31. It is obvious that when it comes to predicting those values, the quasi-1D model performed poorly. However, as mentioned in section 2.3, accuracy of this prediction was not the main goal of this model but a mean to calculating thrust and specific impulse.

This large level of errors can be attributed to a lot of factors not taken into account in the quasi-1D model, such as mixing effects, wall friction or non-uniform distribution of parameters in sections. However, major outliers, such as case 12, are all supersonic, typically with  $M_\infty = 1.6$ . This, in turn, points to difficulties with accurately simulating the influence of shock wave effects on inlet air parameters.

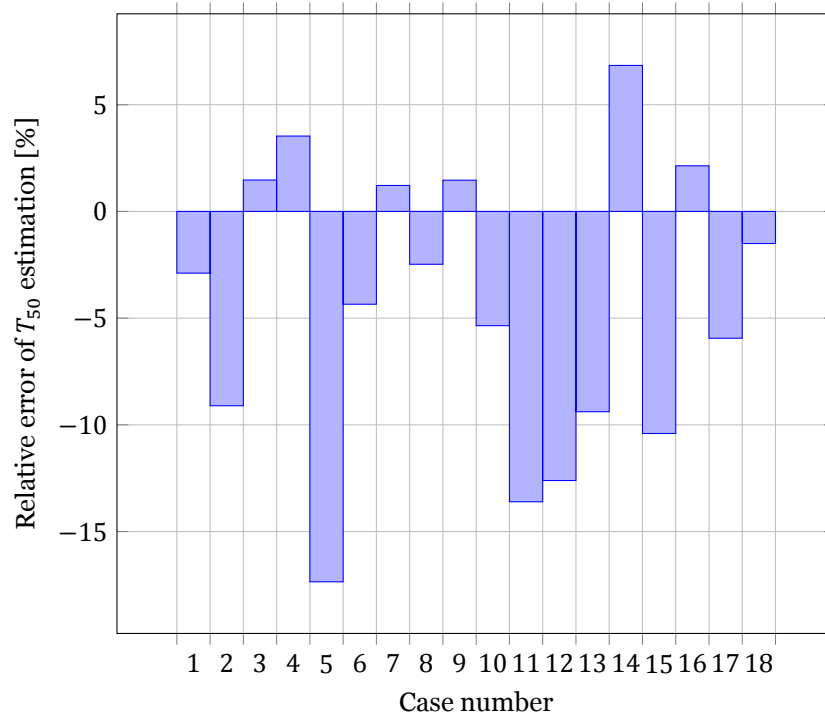


Figure 3.30: Bar graph of relative errors in estimation of afterburner exit total temperature by the quasi-1D model

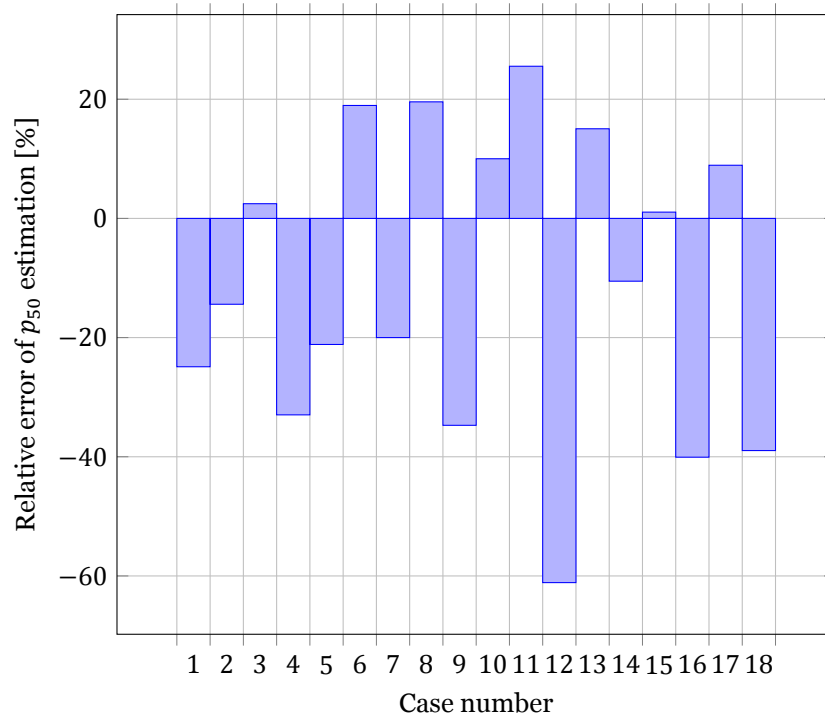


Figure 3.31: Bar graph of relative errors in estimation of afterburner exit total pressure by the quasi-1D model

As a second, more important comparison, thrust and specific impulse achieved in both models were compared. Results of this comparison are presented in figure 3.32. It can be observed that the relative errors of those predictions are much lower and generally stay within 5% of values from the CFD analysis. Higher spikes in cases 7, 9 and 10 are likely to be caused by not modelling mixing effects – they are all cases with either fuel-rich core rocket operation or active SPI while air mass flow rate is not as large as in other cases. The same situation is in cases 14, 15, 16 and 17, although those errors are not as high.

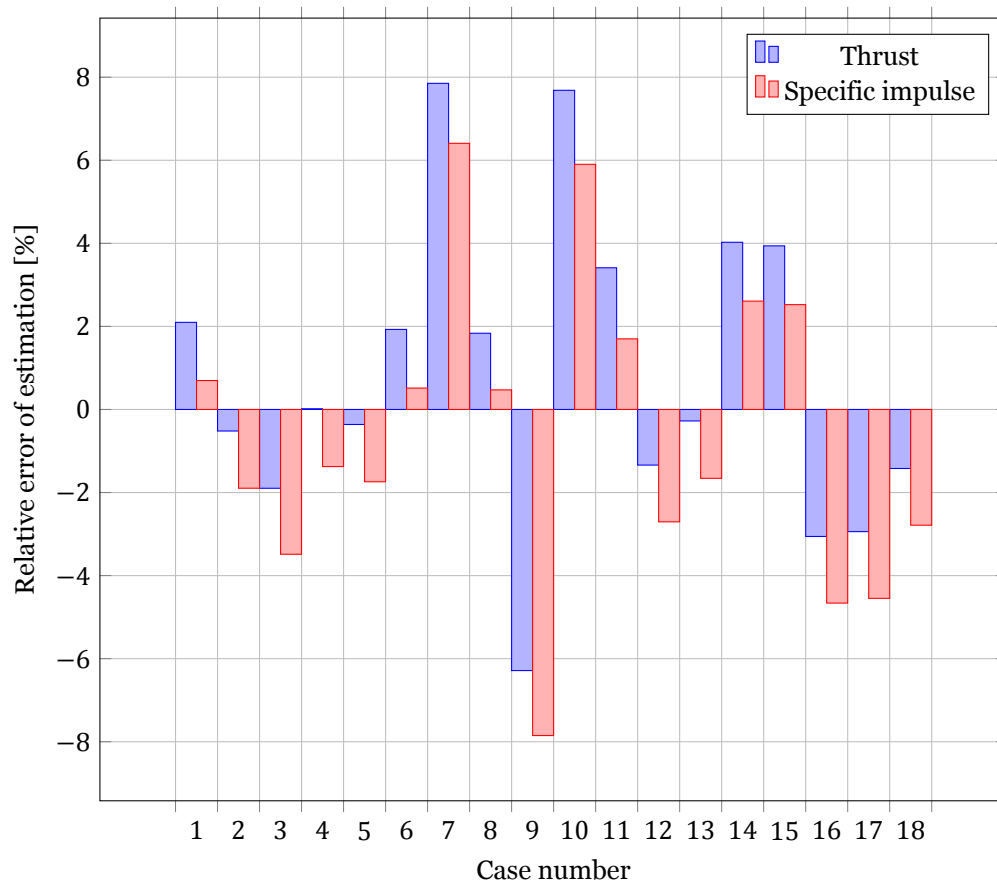


Figure 3.32: Bar graph of relative errors in estimation of thrust and specific impulse by the quasi-1D model

The last important comparison to make was to analyse how the performance changes with Mach number and engine settings in the different models. Only at altitude of 5 km a sufficient number of cases were evaluated to be able to draw conclusions. That is why figures 3.33 and 3.34 present thrust and specific impulse multiplier plotted against free stream Mach number at this altitude. It can be observed that the quasi-1D model over- or underpredicts both thrust and specific impulse but those results exhibit the same trends as the ones from the CFD model.

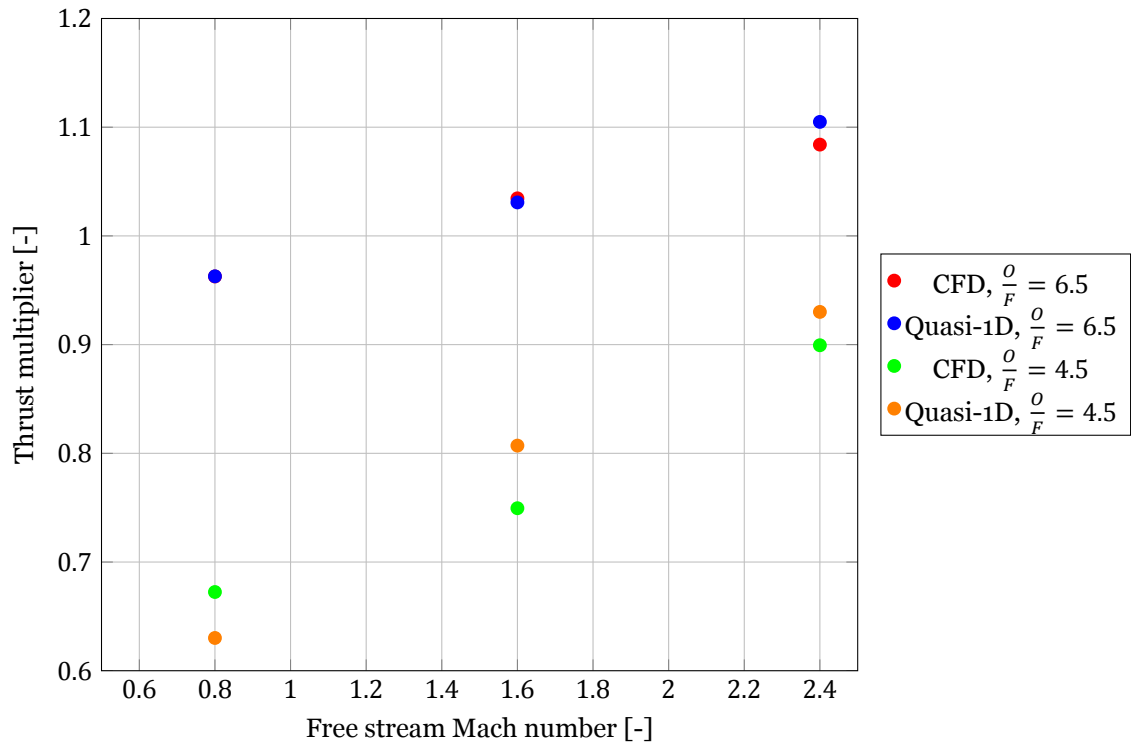


Figure 3.33: Plot of thrust multiplier (compared to rocket-only propulsion) against free stream Mach number at 5 km of altitude for different models and oxidizer to fuel ratios of the core rocket

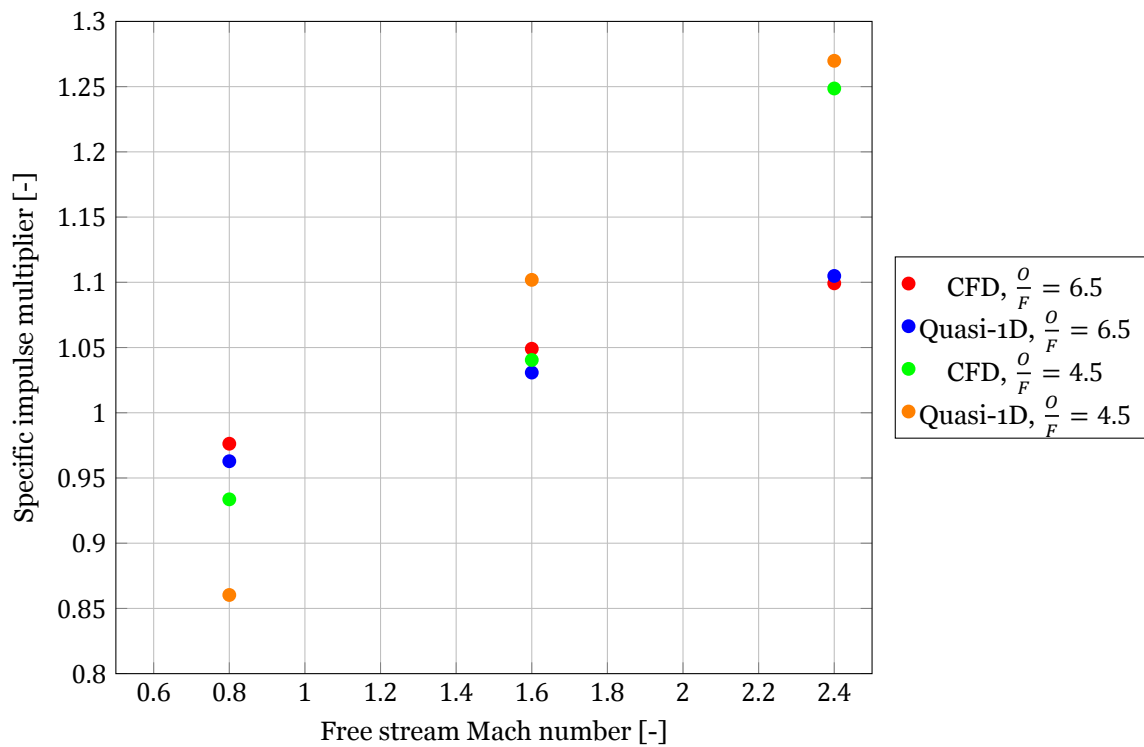


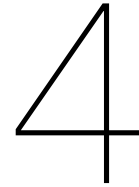
Figure 3.34: Plot of specific impulse multiplier (compared to rocket-only propulsion) against free stream Mach number at 5 km of altitude for different models and oxidizer to fuel ratios of the core rocket

### 3.4.6. Conclusion

The CFD model provided valuable results both for confirming accuracy of the quasi-1D model and identifying relevant areas for future work. The latter certainly includes a thermal design which was not covered at all in this study and which was shown to be problematic due to high temperatures and velocities occurring near afterburner walls. Another aspect is inlet design, as well as its integration with the airframe. The conducted analysis has shown that the low total pressure recovery can lead to significantly reduced performance. The same thing could happen if the inlet interacted negatively with other aerodynamic elements of the airframe. Lastly, shielded primary injection should also be studied further because although one case with noticeable gains in performance was confirmed, in three others only minor or no increase in specific impulse was noted. This is likely to be caused by inadequate combustion arrangement causing the fuel to remain unburned.

Regarding the quasi-1D model, it has been shown that it can predict thrust and specific impulse with accuracy better than 5% with just 3 minor outliers for the given sample. This means that the model could be used for initial stages of design. This is an important achievement since quasi-1D model is much simpler and faster than CFD methods. However, this accuracy does not concern all parameters, such as pressures and temperatures, which can be largely over- or underpredicted. Similarly, some degree of caution should be kept when applying the developed model to RBCC engines that stray far from the geometry that was used to verify the quasi-1D model.





# Trajectory optimisation

Having a validated and verified model to simulate RBCC engines and a candidate design, it was important to analyse how the change of propulsion from rocket-only to RBCC would impact the performance of the whole vehicle. A chosen indicator of it was the maximum achievable apogee. This is a better parameter for comparison than, for example,  $\Delta v$  because when comparing air-breathing to rocket engines it is necessary to optimise the trajectory for both propulsion types. Therefore, apogee is a parameter that is directly available in the optimisation process while  $\Delta v$  would have to be calculated along the optimal trajectory. The following sections present the assumptions and methodology used in optimising the trajectory, as well as its results.

## 4.1. Assumptions and implementation

The optimisation method used was a gradient-based method and required a design vector that would unambiguously represent a given trajectory. Therefore, section 4.1.1 presents a general trajectory that was used and the following sections describe in detail how all flight phases were modelled.

### 4.1.1. Trajectory profile

As the RBCC engine proved to be effective at high speeds in the lower atmosphere, it was considered best to choose a general trajectory that could facilitate such conditions. That is why the profile presented in figure 4.1 was chosen. It consists of 2 straight climb phases with a pitch-up manoeuvre in between and a coast phase after burnout. For this trajectory there are 3 design variables: two climb angles ( $\theta_1$  and  $\theta_2$ ) and a point in time when the pitch-up manoeuvre would be started. The last parameter was defined by the percentage of propellant left at the end of the 1<sup>st</sup> climb phase.

To avoid any singularities, the climb angles were restricted to a range of  $3^\circ$ – $89^\circ$  and the remaining propellant percentage to 5%–95%. Additionally,  $\theta_2$  was constrained to always be higher than  $\theta_1$  and the starting point was chosen to be after take-off at the altitude of 500 m and at the speed of  $50 \frac{\text{m}}{\text{s}}$ . The propellant needed for take-off was neglected.

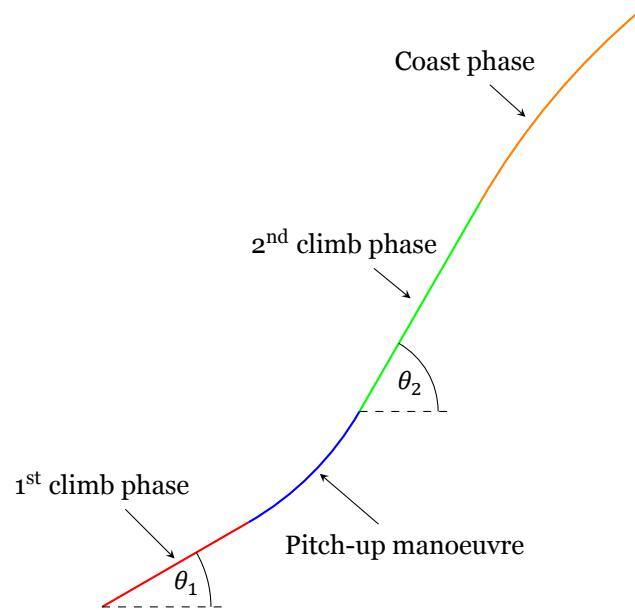


Figure 4.1: General trajectory considered in the trajectory optimiser

#### 4.1.2. Climb phase

Figure 4.2 presents forces acting on a spaceplane during the climb phase: lift  $\vec{L}$ , drag  $\vec{D}$ , thrust  $\vec{T}$  and gravity  $\vec{F}_g$ . To simplify calculations, it is assumed that angle of attack is small and therefore thrust is aligned with velocity.

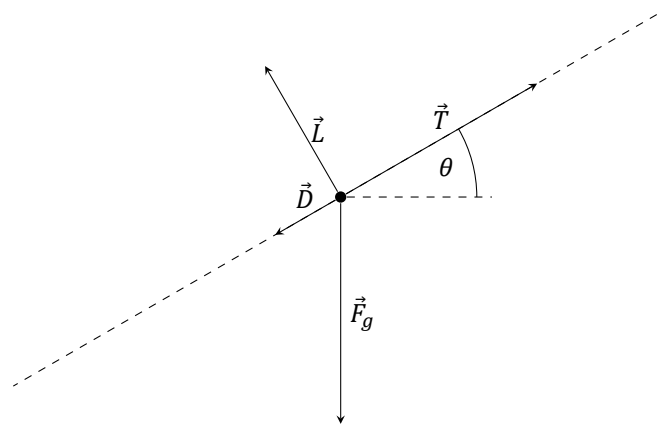


Figure 4.2: Forces acting on the spaceplane during the climb phase

For both climb phases the trajectory is assumed to be completely straight, thus forces perpendicular to the trajectory had to be balanced:

$$L = F_g \cos \theta \quad (4.1)$$

This equation is used to calculate the needed lift and, as a consequence, angle of attack and drag for given conditions using the aerodynamic model of the spaceplane. Knowing other forces based on flight conditions, a system of differential equations could be formed and integrated over time:

$$\begin{cases} \frac{dh}{dt} = v \sin \theta \\ \frac{dv}{dt} = \frac{T}{m} - \frac{D}{m} - g_0 \sin \theta \\ \frac{dm}{dt} = -\frac{T}{I_{sp} g_0} \end{cases} \quad (4.2)$$

In the above equations  $h$  is the altitude,  $v$  is the velocity,  $m$  is the instantaneous mass of the spaceplane and  $g_0$  is the Earth's gravitational acceleration, which was considered constant for the purpose of this model. This system of equations for both climb phases was integrated until the mass of the spaceplane reached the value equal to the dry mass or a value predefined by the trajectory.

### 4.1.3. Pitch-up manoeuvre

Figure 4.3 presents forces acting on a spaceplane during the pitch-up manoeuvre. The annotations are consistent with previous sections. Again, it is assumed that the angle of attack is small and therefore thrust is aligned with velocity.

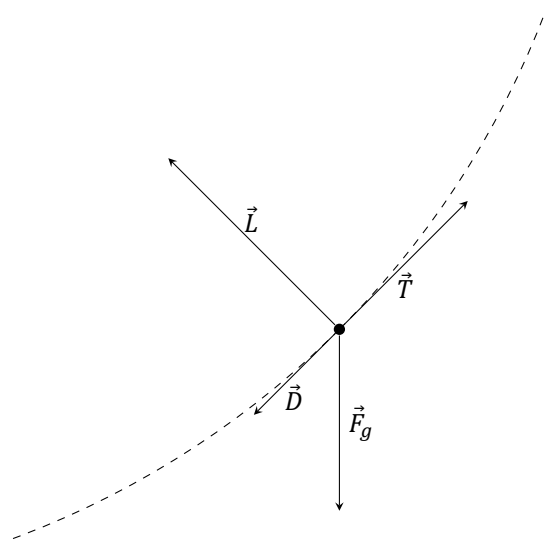


Figure 4.3: Forces acting on the spaceplane during the pitch-up manoeuvre

In this case the spaceplane is following a 2D trajectory and there is no equilibrium between any of the forces. Angle of attack in this case was chosen such that the load factor  $n$  during the manoeuvre would be constant and equal to 10. This value is relatively high, similar to maximal load factors for fighter aircraft, but since Mk-II *Aurora* is unmanned it is considered realistic. Therefore, lift force was simply calculated as:

$$L = nF_g \quad (4.3)$$

Based on the aforementioned conditions and the angle of attack, the drag force could be calculated as well. The following system of equations could be integrated:

$$\begin{cases} \frac{dh}{dt} = v_y \\ \frac{dv_x}{dt} = T \cos \theta - \frac{L \sin \theta}{m} - \frac{D \cos \theta}{m} \\ \frac{dv_y}{dt} = \frac{T \sin \theta}{m} + \frac{L \cos \theta}{m} - \frac{D \sin \theta}{m} - g_0 \\ \frac{dm}{dt} = -\frac{\dot{m}_T}{I_{sp} g_0} \end{cases} \quad (4.4)$$

In this set of equations  $h$  is the altitude,  $v_y$  is the vertical component of velocity,  $v_x$  is the horizontal component of velocity,  $m$  is the instantaneous mass of the spaceplane and  $g_0$  is the Earth's gravitational acceleration, again considered constant in the model.  $\theta$  in this case is the instantaneous climb angle and is defined as:

$$\theta = \arcsin \frac{v_y}{\sqrt{v_x^2 + v_y^2}} \quad (4.5)$$

The integration of the above equations was carried out until  $\theta$  reached the predefined value of the second climb angle. This is when another straight climb was started.

#### 4.1.4. Coast phase

The coast phase was realised after the burnout of the engine. It is a phase where the spaceplane flies at zero angle of attack and therefore no lift is generated. This phase lasts until the apogee is reached or the spaceplane escapes the atmosphere (at the altitude of 86 km according to the Standard Atmosphere [26]). In the latter case the apogee was calculated based on vertical velocity at the edge of the atmosphere by applying the energy conservation equation. In the former, it was a direct result of integrating differential equations described in this section.

Figure 4.4 presents the forces acting on a spaceplane during the coast phase: drag and gravity. Similarly to the pitch-up manoeuvre, in this case trajectory is fully 2D and a system of differential equations needed to be solved is almost identical, as seen below. As mentioned before, the integration of those equations was continued until the apogee was reached or the altitude reached 86 km.

$$\begin{cases} \frac{dh}{dt} = v_y \\ \frac{dv_x}{dt} = -\frac{D \cos \theta}{m} \\ \frac{dv_y}{dt} = -\frac{D \sin \theta}{m} - g_0 \\ \frac{dm}{dt} = -\frac{\dot{m}}{I_{sp} g_0} \end{cases} \quad (4.6)$$

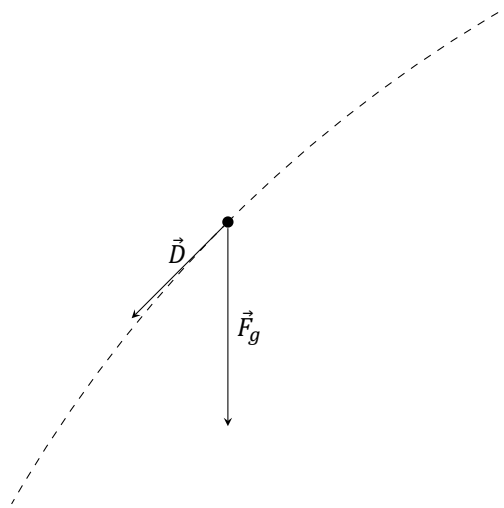


Figure 4.4: Forces acting on the spaceplane during the coast phase

#### 4.1.5. Propulsion look-up table

The most important part of the trajectory optimiser was of course the propulsion model. It had to accurately reflect results of the quasi-1D model, as well as the data for the reference rocket engine. At the same time, it could not be computationally costly because it would be called many times during each trajectory calculation. That is why look-up tables were created: for the rocket-only case using the Rocket Propulsion Analysis Program [21] and for the RBCC case using the developed quasi-1D model. For the latter, at each conditions different settings of the engine were tried (including different  $\frac{O}{F}$  ratios and mass flow rates of fuel in SPI) in order to obtain the maximum specific impulse in each conditions. In vacuum, where the model cannot obtain a converged solution, it was considered that the RBCC afterburner works as a high expansion ratio nozzle with a relatively low efficiency (92% was assumed). Cases with low air flow (at high altitude and low airspeed, resulting in air mass flow rates below 10% of that from the core rocket), which were also mostly not converging, were interpolated between the previously obtained values and vacuum conditions. The results of those calculations are presented in figure 4.5.

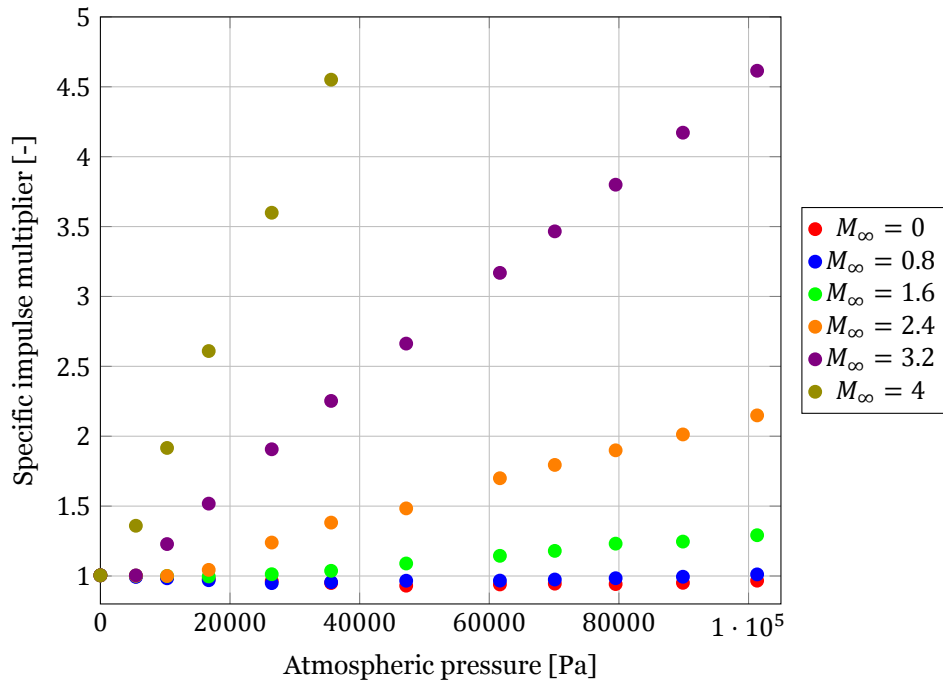


Figure 4.5: Plot of a look-up table of maximal specific impulse multiplier (compared to rocket-only propulsion) against atmospheric pressure for different free stream Mach numbers

## 4.2. Results

The following sections present the results of the trajectory optimisation obtained by running the optimiser multiple times with a different initial design vector (angles  $\theta_1$ ,  $\theta_2$  and left propellant percentage). This was done to have a better chance of obtaining a global maximum of the apogee.

Both of the propulsion cases considered in the analysis use the same aerodynamic and mass data for the vehicle, which makes the investigation favourable for the RBCC propulsion. This is because it is expected that RBCC propulsion will be heavier and will generate more drag than a traditional rocket engine.

### 4.2.1. Trajectory

The atmospheric phases of the obtained optimal trajectories are presented in figure 4.6. Corresponding apogees are the following: 126.35 km for rocket-only propulsion and 113.95 km for RBCC propulsion. This means that even in the most favourable analysis the RBCC engine is not providing any performance gains for the vehicle, making the design change undesired.

Worth noticing here is that optimal trajectories are visibly different but they both end up being very steep. This is to be expected as the target was to obtain the highest apogee. However, in the case of RBCC propulsion, it was expected that the shallow climb phase would be significantly longer for optimal performance. This is not the case because of the high atmospheric losses for such a trajectory, meaning that the optimiser quickly moved away to a much steeper one.

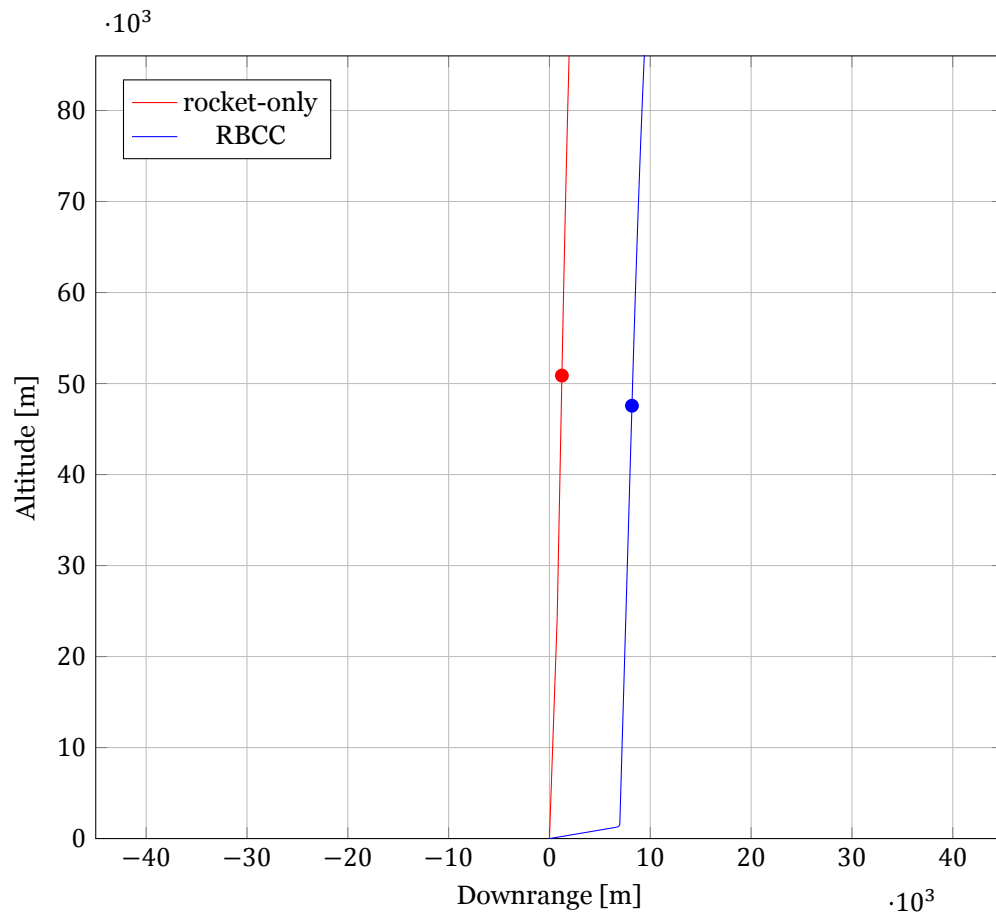


Figure 4.6: Atmospheric part of the optimal trajectories for rocket-only and RBCC propulsion (dots represent the burnout point)

#### 4.2.2. Specific impulse

To better understand why RBCC propulsion did not provide the hypothesized performance gains, the specific impulse was plotted for both rocket-only and RBCC propulsion along the optimal trajectory. Those plots are presented in figures 4.7 (as a function of altitude) and 4.8 (as a function of airspeed). It is clear that rocket engine's specific impulse is higher at the low speed regime. When the vehicle reaches higher speeds this happens in a relatively thin atmosphere, meaning that performance gains are modest.

It is worth noticing that the beginning of a pitch-up manoeuvre is clearly visible in those plots as a notch in the RBCC curve. This is when drag increases significantly causing speed and, consequently, specific impulse to drop. The latter then recovers very slowly because the airspeed is almost constant (as the vehicle is still heavy and the trajectory is almost vertical). All this causes the vehicle to stay in the subsonic speed regime for a long time, until reaching the altitude of more than 15 km. Therefore, in order to provide better performance, a solution is needed for increasing specific impulse and, ideally, thrust at low speeds. This would allow for staying longer in the dense atmosphere and also overcoming higher atmospheric losses.

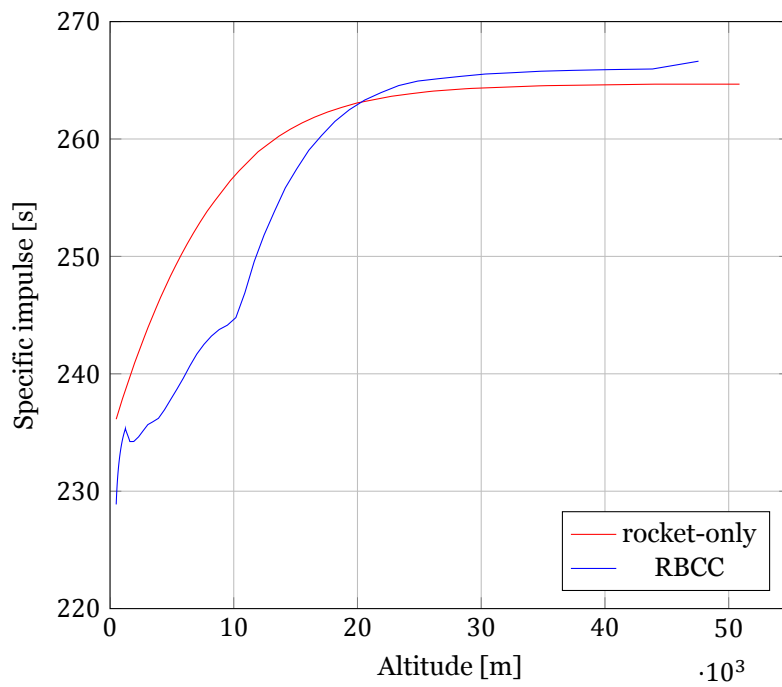


Figure 4.7: Plot of specific impulse against altitude along the optimal trajectories for rocket-only and RBCC propulsion

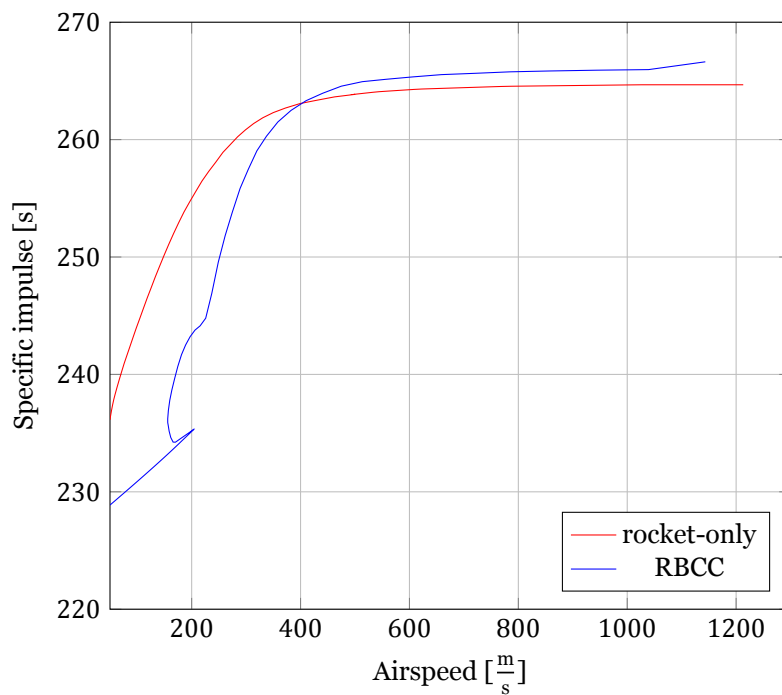


Figure 4.8: Plot of specific impulse against airspeed along the optimal trajectories for rocket-only and RBCC propulsion



# 5

## Alternative RBCC design

A typical solution for increasing the performance of an RBCC engine is including a compressor. This has been considered even in very early studies such as the one by Bendot et al. [2]. A compressor allows for both increasing the mass flow rate of air at low speeds and increasing the momentum of the flow. Those two effects, in turn, allow for achieving much greater thrust and specific impulse. The downside of using a compressor is, of course, added mass. This consists not only of the compressor itself but also its support structure, required equipment (control, power supply etc.) and a bypass mechanism for when the compressor cannot be operated. The last one is necessary as simple small compressors usually cannot be operated at supersonic speeds.

In this study, as a first approximation, the developed quasi-1D model was used under the assumption that the compressor is utilized at subsonic speeds and it has a constant and relatively small (according to exemplary characteristics presented by Howell and Bonham [12]) total pressure ratio of 2. This implies a usage of a compressor with rotational speed adjusted to conditions so that this pressure ratio is preserved. Practically, a compressor would likely be used differently with rotational speed maintained at a constant level and mass flow rate and total pressure ratio changing according to characteristics. Those characteristics are, however, hard to obtain and specific to a given compressor. The proposed approach was therefore deemed as a good first indicator of how effective a design with a compressor could be.

### 5.1. Design selection

Having a compressor installed at the inlet allowed for altering the design in order to optimise its performance. The major change that could be done was the enlargement of the afterburner because with the added compressor the separation of flow at static sea level conditions in the RBCC nozzle was not a big issue. Figure 5.1 presents the results that are supporting the choices made. The figure shows a large dependency of performance on the size of the afterburner but also expansion ratio of the core rocket nozzle. All cases considered are with fuel-rich operation of the core rocket because this offers the best performance given the increased mass flow of air provided by the compressor.

Summarising,  $A_5 = 0.012 \text{ m}^2$  was chosen along with the expansion ratio of 3. From all considered cases this configuration yielded the highest specific impulse. Those parameters were put together with a symmetric inlet of maximum area that allowed for the afterburner to have straight geometry, this was justified already in section 2.4.2. All parameters are summarised in table 5.1.

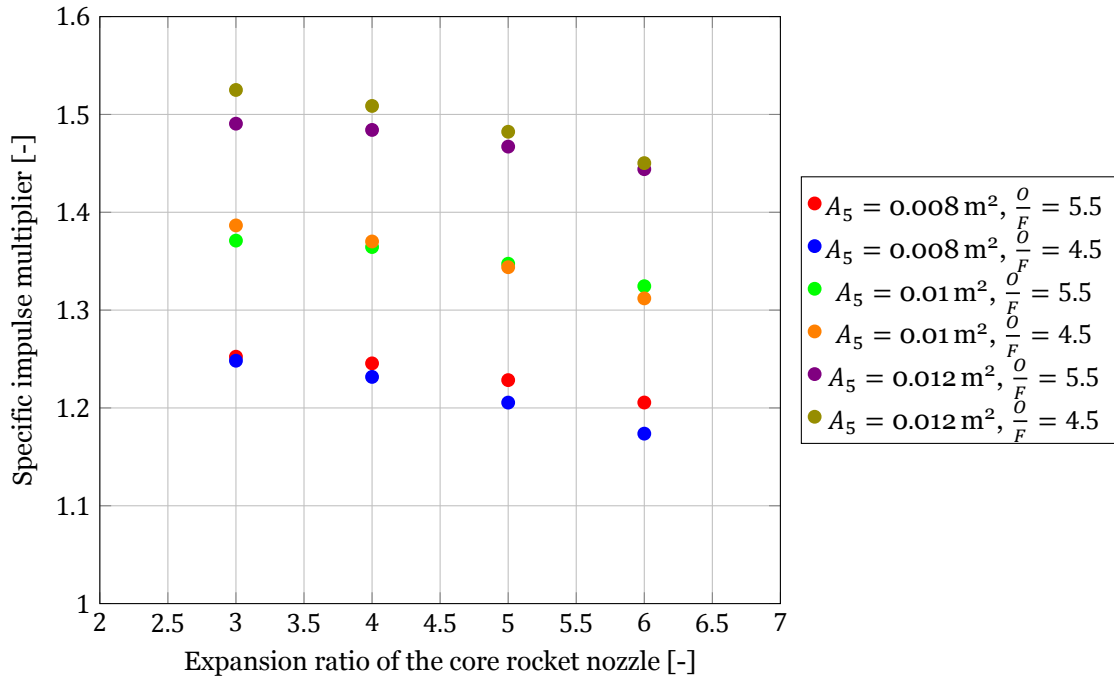


Figure 5.1: Plot of specific impulse multiplier (compared to rocket-only propulsion) against expansion ratio of the core rocket nozzle for different afterburner sizes and oxidizer to fuel ratios

Table 5.1: Parameters of the RBCC design with compressor

Design parameter	Final design value
$A_1$ [m <sup>2</sup> ]	0.0107
$A_2$ [m <sup>2</sup> ]	0.0075
$A_4$ [m <sup>2</sup> ]	0.0107
$A_5$ [m <sup>2</sup> ]	0.0120
$A_6$ [m <sup>2</sup> ]	0.0132
Afterburner length [m]	0.6
Core rocket nozzle expansion ratio	3

## 5.2. Alternative design performance

In order to assess the vehicle performance with a compressor, a new look-up table was created. Values from this table are plotted in figure 5.2. It can be seen that for subsonic cases, when the compressor is used, the specific impulse gains are substantial — over 50% at lower altitudes. When the compressor is turned off at Mach 1, they drop and then recover again with raising airspeed. Changes in performance when the atmospheric pressure decreases are, however, practically the same as without the compressor (see figure 4.5) — close to linear drop in specific impulse can be observed.

In this case, similarly to the previous RBCC design, vacuum performance was estimated using Rocket Propulsion Analysis Program [21]. For conditions with low airspeed at high altitudes, the specific impulse was interpolated because the developed model could not produce a solution with that little airflow.

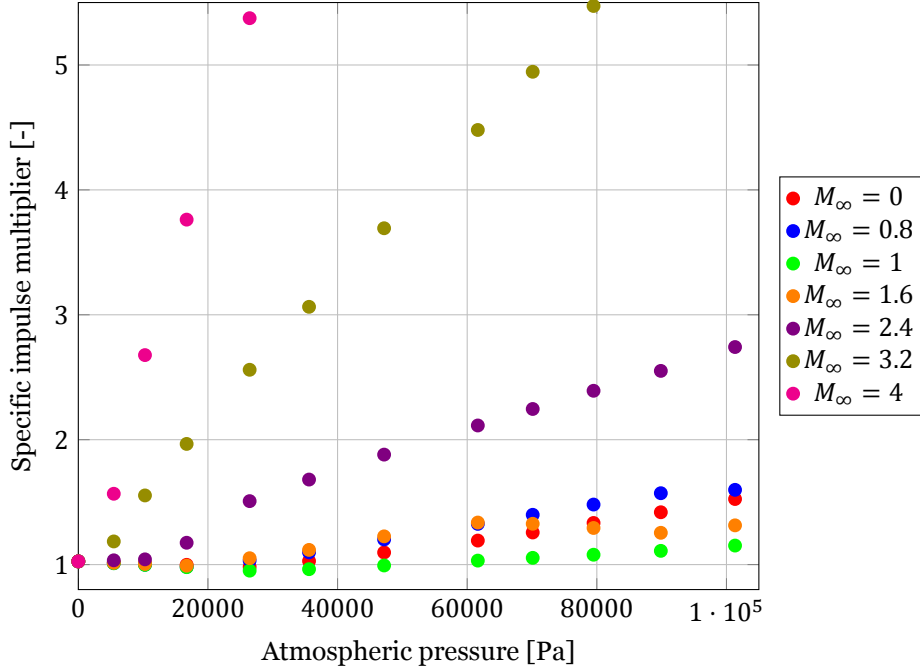


Figure 5.2: Plot of a look-up table of maximal specific impulse multiplier (compared to rocket-only propulsion) against atmospheric pressure for different free stream Mach numbers — RBCC with a compressor

### 5.3. Drag and mass estimation

Given the values of specific impulse obtained in the look-up table, it was obvious that the RBCC design with a compressor would provide a higher apogee altitude for the vehicle if no other parameters are changed. This, however, is not a very realistic situation. Practically, both dry mass and drag would increase if a concept of RBCC with compressor was implemented. That is why an estimation of those quantities was necessary.

It is important to mention that calculations presented in this section are very preliminary and are potentially subject to large errors. This problem was tackled by considering worst-case values to be 50% greater than the ones calculated.

To correctly estimate drag increase it was important to realise that the RBCC engine does not produce much of it as it does not significantly increase the frontal area of the fuselage. At the same time, inlet ram drag was already included as a negative term in the thrust equation. This means that besides parasitic or wave drag, which highly depends on the way RBCC engine would be integrated with the existing structure, the most important contributor is friction drag from increased wetted area. This can be estimated given that maximal afterburner diameter is equal to:

$$d = \sqrt{\frac{4A_6}{\pi}} \approx 0.13 \text{ m} \quad (5.1)$$

As the afterburner is cylindrically shaped, added wetted area is approximately:

$$\Delta A_{wet} = \pi d L \approx 0.244 \text{ m}^2 \quad (5.2)$$

If it is assumed that the flow around a flat plate at zero angle of attack can be used, because only friction drag is to be taken into account, the increase in drag coefficient of the whole vehicle can be estimated:

$$\Delta C_D = \frac{\Delta A_{wet} C_{D,plate}}{2 A_{ref}} \approx 0.00094 \quad (5.3)$$

This equation converts conservatively assumed (according to values presented by Spalding [25]) drag coefficient of a flat plate  $C_{D,plate} = 0.02$  into drag coefficient increase for the whole vehicle.

The mass increase calculation consisted of the summation of afterburner, inlet and compressor assembly mass. Firstly, the afterburner mass was estimated under the assumption of using Inconel as material due to its excellent heat resistance properties. Taking into account that the maximum pressure that could be achieved in the afterburner, according to simulations, is 20 bar, the design pressure was chosen to be  $p_{des} = 40$  bar. Therefore, minimum thickness, based on hoop stress that can appear in the structure, is the following:

$$t = \frac{p_{des}d}{2\sigma_y} \approx 1.04 \text{ mm} \quad (5.4)$$

The yield strength of Inconel was assumed to be relatively low  $\sigma_y = 250$  MPa (it corresponds to the temperature of 850 °C according to Oliveira et al. [19]). However, this value depends highly on the working temperature so possibly with a good cooling system it could be raised. Given density of Inconel  $\rho_{Inconel} = 8200 \frac{\text{kg}}{\text{m}^3}$  (according to Hosaeus et al. [11]), the mass of the afterburner could be estimated as:

$$m_{afterburner} = \Delta A_{wet} t \rho_{Inconel} \approx 2.08 \text{ kg} \quad (5.5)$$

A similar calculation could be done for the inlet but the loads in this case are harder to estimate correctly. Therefore, it was assumed that inlet is made of carbon fibre composite with a thickness of  $t_{inlet} = 0.5$  mm. The inlet shape is assumed to be a cylinder around the fuselage, meaning that its diameter would be equal to roughly  $d_{inlet} = 0.15$  m and the length is equal to  $L_{inlet} = 0.5$  m. Therefore, the mass of the inlet was estimated to be:

$$m_{inlet} = 2\pi d_{inlet} L_{inlet} t_{inlet} \rho_{composite} \approx 0.37 \text{ kg} \quad (5.6)$$

A factor of 2 in this equation was used to account for a deployment mechanism as this inlet would be used only at supersonic speeds to bypass the compressor. Composite density was conservatively assumed to be  $\rho_{composite} = 1550 \frac{\text{kg}}{\text{m}^3}$ , according to Dhakate and Bahl [7].

The compressor assembly mass was the most complicated to estimate. To simplify the process, it could be assumed that a COTS jet engine is used with a relatively high air to fuel ratio. This is likely one of the lightest possible solutions because a kerosene feed system is already in place meaning not many other parts apart from the engine are needed. A suitable choice could be PBS TJ40-G1 engine manufactured by PBS Aerospace [20] with mass of  $m_{engine} = 3.3$  kg. However, given its low thrust of 395 N, it is likely that 2 of those engines would be needed to provide mass flows similar to the ones obtained in the simulation. Adding an additional 10% mass per engine to account for its mounting and necessary equipment, the compressor assembly was estimated to weigh:

$$m_{compressor} = 2.2m_{engine} + m_{inlet} = 7.63 \text{ kg} \quad (5.7)$$

The mass  $m_{inlet}$  was used again in this equation as a mean to estimate mass of ducts leading air to the engine, as well as their deployment mechanisms.

Finally, the total mass of the RBCC engine with a compressor could be estimated as:

$$m_{RBCC} = m_{afterburner} + m_{inlet} + m_{compressor} = 10.07 \text{ kg} \quad (5.8)$$

## 5.4. Trajectory results

Using the aforementioned data, an assessment of the vehicle performance was possible. The optimisation was conducted for multiple different initial trajectories and best obtained results are presented here.

### 5.4.1. Trajectory

The ideal case of trajectory assumes no mass or drag increase. The realistic one uses values as presented in section 5.3. Finally, the worst-case adds the additional 50% margin on top of realistic values. Summary of this data is presented in table 5.2.

Table 5.2: Mass and drag increase for different considered cases

	Realistic	Worst-case
Mass increase	10.07 kg	15.11 kg
Drag increase	0.00094	0.00141

Figure 5.3 presents obtained trajectories for rocket-only propulsion (as reference) and for RBCC with compressor cases. Apogees for the trajectories presented are the following:

- rocket-only: 126.35 km
- RBCC — ideal: 169.32 km
- RBCC — realistic: 123.48 km
- RBCC — worst-case: 105.87 km

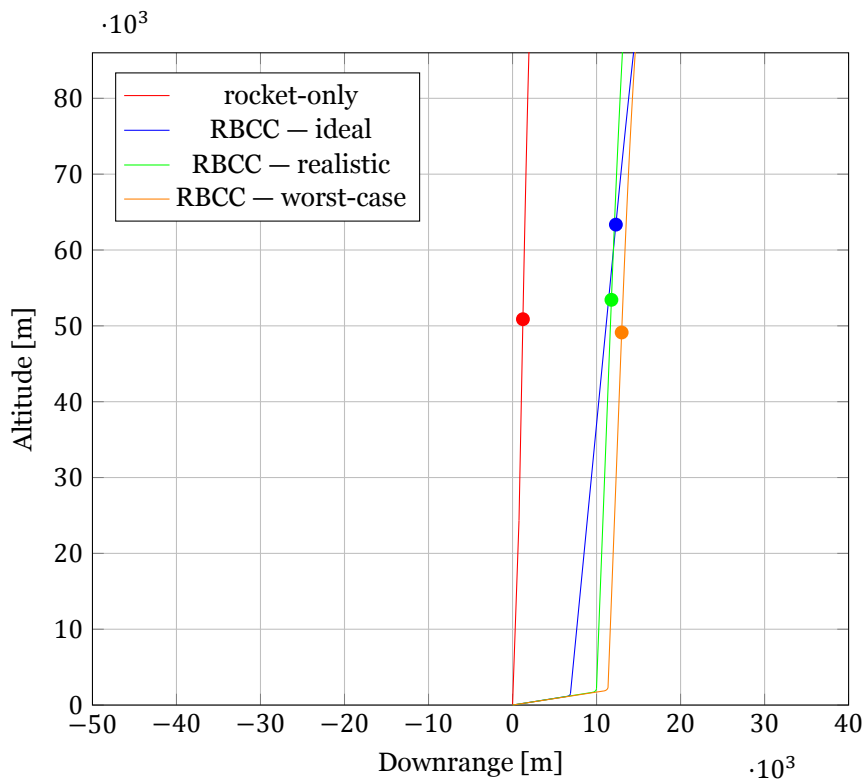


Figure 5.3: Atmospheric part of the optimal trajectories for rocket-only and RBCC propulsion with compressor (dots represent the burnout point)

Given the obtained apogees, it is clear that the performance gains are heavily dependent on how lightweight the RBCC engine can be and how small the imposed drag is. Assuming an added mass of 10.07 kg and increasing drag coefficient by 0.00094 already diminishes practically all specific impulse gains and decreases the apogee to within simulation accuracy of that with rocket-only propulsion.

One more interesting comment to make is that having a heavier vehicle means that the optimal trajectory is flatter due to the vehicle remaining at low speeds for longer. This is because drag is dependent on the square of velocity so even though the spaceplane stays in the atmosphere longer, aerodynamic losses are the same.

### 5.4.2. Specific impulse

Just as in the case without a compressor, the specific impulse was plotted along the trajectory against altitude (figure 5.4) and airspeed (figure 5.5). Those plots reveal that altitude is the most important variable for RBCC engines. The only point in time when performance gains are achieved is below 10 km, after that they are non-existent or relatively modest.

This is a fundamental problem for RBCC engines. When the goal is to reach space, the vehicle cannot stay in the dense atmosphere for very long due to aerodynamic losses, therefore it is hard to generate significant gains using heavy air-breathing engines. Concepts of complicated propulsion systems that would use inlet air in the main rocket engine chamber, such as the SABRE engine analysed by Zhang et al. [32], can also eventually run into the same problem as they provide more specific impulse in the dense atmosphere but also add more mass which they might not be able to compensate for.

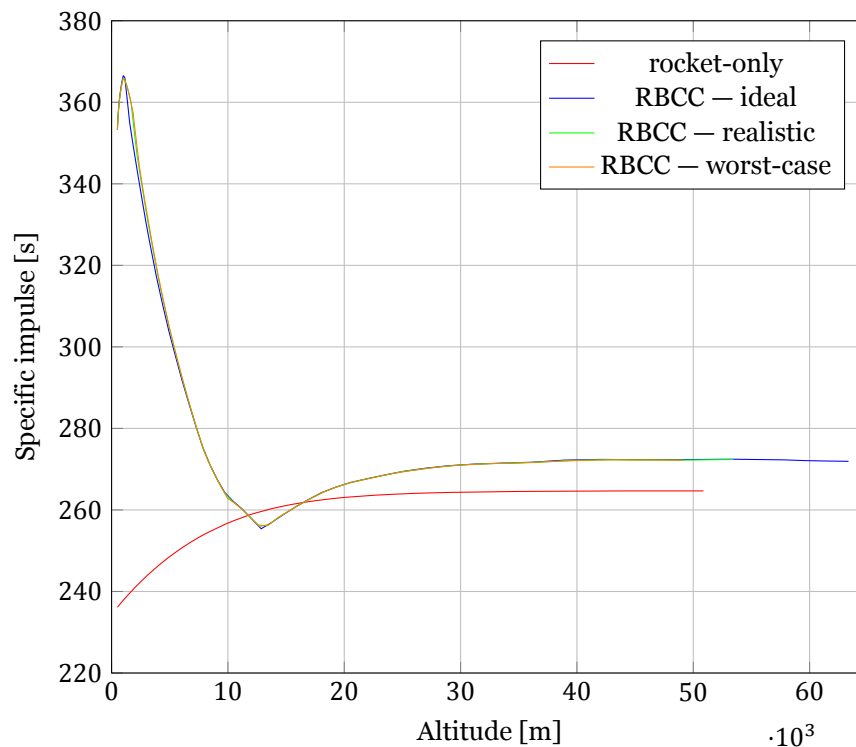


Figure 5.4: Plot of specific impulse against altitude along the optimal trajectories for rocket-only and RBCC propulsion with compressor

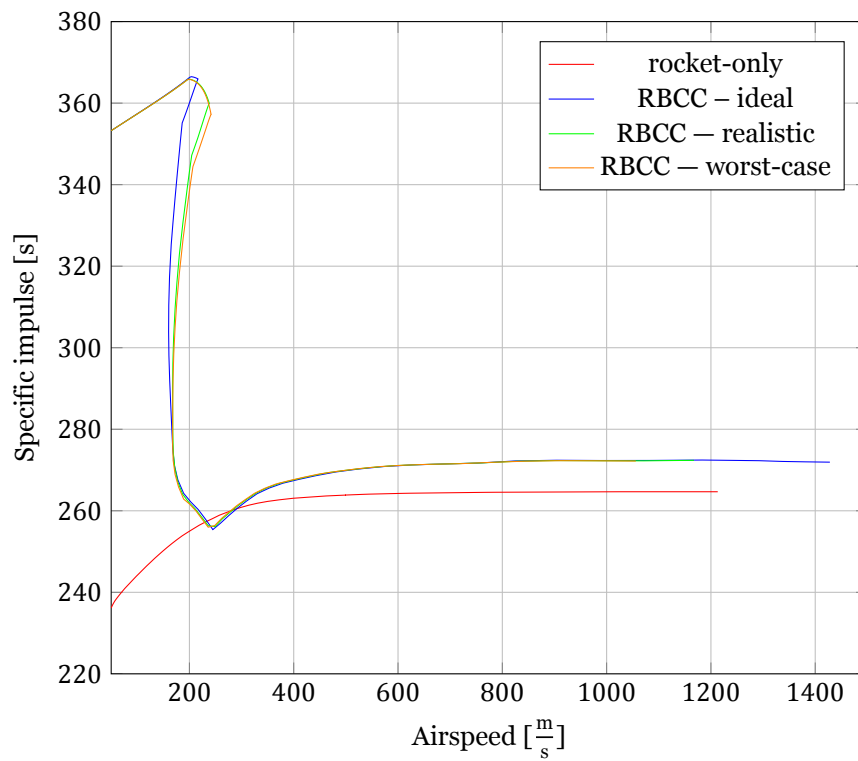


Figure 5.5: Plot of specific impulse against airspeed along the optimal trajectories for rocket-only and RBCC propulsion with compressor



# 6

## Conclusions

Having conducted the trajectory calculations both for the design with and without a compressor, it was possible to answer the research questions stated in the beginning of this study. This chapter presents those answers and provides recommendations for the future work.

### 6.1. Quasi-1D model

One of the major achievements of this research is a creation of a validated (with experimental data) and verified (with CFD methods) quasi-1D model of a RBCC engine. It is a tool that allows for a quick and easy estimation of performance given design parameters and conditions. Undoubtedly, any future work in this field can benefit from utilizing such a tool.

### 6.2. Final RBCC configuration

The initial design that was considered in the CFD model proved to not meet the expectations from literature. The most crucial identified drawback was that augmentation of thrust was only reached after Mach 0.8. That was also conditional on the altitude of flight at this point of time. In the literature this effect is rarely discussed. This may be caused by the fact that decrease in thrust at low airspeeds is minimal (only about 2–4%) and can be attributed to losses in the afterburner. These losses include: shear layer interaction of streams, friction against the walls, etc. If a given model does not correctly estimate nozzle and combustion efficiency at those conditions, the loss of thrust may be non-existent.

Despite the fact that the loss of thrust is small, it was sufficient to make the whole design impractical for space launch purposes. At higher altitudes the engine could not make up for the losses at low speeds. This caused the situation where even without mass or drag increase rocket-only propulsion proved to be better. This design was discarded and a different approach had to be found.

Bendot et al. [2] recommends the use of a compressor to significantly increase the performance at low velocities. This approach was adopted and analysed. Thanks to a few simplifications, the previously developed quasi-1D model could be applied to this design as well and the performance prediction could be made.

#### 6.2.1. Design parameters

The design with a compressor has the potential to significantly improve on the RBCC performance because it does not run into the same problems at take-off conditions, such as separation of flow in the nozzle. This allows for substantial specific impulse gains at almost all flight conditions. The final design parameters are repeated in table 6.1.

Table 6.1: Parameters of the RBCC design with compressor

Design parameter	Final design value
$A_1$ [m <sup>2</sup> ]	0.0107
$A_2$ [m <sup>2</sup> ]	0.0075
$A_4$ [m <sup>2</sup> ]	0.0107
$A_5$ [m <sup>2</sup> ]	0.0120
$A_6$ [m <sup>2</sup> ]	0.0132
Afterburner length [m]	0.6
Core rocket nozzle expansion ratio	3

### 6.2.2. Inlet and compressor assembly design

It is worth repeating here that the design of choice would have to feature a mechanism allowing to bypass the compressor at supersonic speeds. It is, however, believed that such a mechanism could be made lightweight. The inlet design could be optimized by using the incoming air as the actuator because it would only have to be used once during the whole mission.

To estimate the mass of the whole assembly it was assumed that two small jet engines would be used in this role. They can act as a very effective and lightweight compressor provided that they operate at a low equivalence ratio. This would mean that their exhaust contains very little combustion products. However, if such a solution proves to not be possible, alternatively an electric compressor powered by a fuel cell could be used. However, it is believed that this design would be substantially heavier.

### 6.2.3. Shielded Primary Injection

The addition of fuel in the rocket nozzle was analysed both in the quasi-1D and CFD model. The conclusion from this analysis is as follows: added fuel may increase specific impulse of the engine but only in specific conditions. That is when the amount of air flow in the afterburner is significant and when the combustion in the afterburner can be well organised. An even further improvement, however, can be made by operating the core rocket fuel-rich. The difference is that in the latter case thrust usually stayed the same or decreased slightly while for the first one it was increased.

The choice to go for utilizing SPI will be a trade-off as it likely would simplify the operation of the engine — no or very few switches between fuel-rich and standard operation would be needed. However, it also complicates the design of the engine and adds another possible point of failure.

## 6.3. RBCC implementation influence on Mk-II Aurora

The optimal trajectory had to be found for each considered case in order to assess RBCC implementation influence on the vehicle. The maximum apogee was chosen as an indicator but it can easily be traded for e.g. higher payload mass if desired.

A higher apogee could be achieved using an RBCC with a compressor given that the RBCC does not add significant mass or drag. It was found that with a compressor the maximum apogee could be increased with 45 km, a 50% increase compared to the rocket-only design. However, adding the expected mass and drag resulted in diminished gains. Nevertheless, this does not necessarily mean that RBCC implementation is not going to be beneficial. A further, more in-depth analysis, would have to be made to confirm this. That is because the current mass and drag estimation is very preliminary.

Additionally, it is important to mention that the implementation of the identified design could have other benefits. Relatively high specific impulse would allow for more aircraft-like operation of the spaceplane because the fuel consumption at low altitudes and speeds would be much lower than for rocket-only propulsion. For example, some cruise time could be allowed before climb phase or, given that some fuel would be saved, the spaceplane could have some limited loitering capability before having to land at the airfield of destination.

For the future two-stage orbital-capable version of the spaceplane, the RBCC engine with compressor can also be considered. In this case the most beneficial option would be to choose the staging point at low altitude (preferably 10–20 km) such that the RBCC engine can work in the best possible conditions.

## 6.4. Recommended future work

Although the presented research was extensive and covered large parts of the field of designing RBCC engines, it could not cover everything. The main part of possible future work could be a detailed design of the compressor version of the RBCC engine. Within this research, a compressor implementation would have to be chosen and new, more accurate performance characteristics could be obtained given the data about the said compressor. Then, a detailed design could be finished and manufactured in order to verify the results in static tests. This design could also serve as a reference point for mass and drag estimates of the final flight version.

Another area of further work is connected with thermal design. It is of great importance to analyse this early, because this is a very challenging aspect for the afterburner. Combination of high temperatures and velocities allows for high heat flux that would have to be handled by a cooling system or the chosen material itself.

Lastly, at some point a more detailed study of each of the RBCC engine's components and their integration with the airframe would have to be conducted. This would have to consider structural and aerodynamic aspects as well as mass balance and connection of important systems such as cooling and fuel feed lines. The largest area of work here is inlet design, which goal would be to obtain satisfying performance while keeping drag and mass increase minimal.



# Bibliography

- [1] ANSYS. *Fluent*. Version 2019 R3. URL: <https://www.ansys.com/>.
- [2] J. G. Bendot, P. N. Brown, and T. G. Piercy. *Composite engines for application to a single-stage-to-orbit vehicle*. 1975.
- [3] Mikhail Pavlovich Bulat and Pavel Victorovich Bulat. “Comparison of Turbulence Models in the Calculation of Supersonic Separated Flows”. In: *World Applied Sciences Journal* 27 (Dec. 2013), pp. 1263–1266. ISSN: 1818-4952. DOI: 10.5829/idosi.wasj.2013.27.10.13715.
- [4] Malcolm W. Chase. *NIST-JANAF Thermochemical Tables*. Vol. 14. 1985. ISBN: 1-56396-831-2.
- [5] Russell Daines and Corin Segal. “Combined Rocket and Airbreathing Propulsion Systems for Space-Launch Applications”. In: *Journal of Propulsion and Power* 14 (5 Sept. 1998), pp. 605–612. ISSN: 0748-4658. DOI: 10.2514/2.5352. URL: <https://arc.aiaa.org/doi/10.2514/2.5352>.
- [6] *Dawn Aerospace website*. URL: <https://www.dawnaerospace.com/>.
- [7] S.R. Dhakate and O.P. Bahl. “Effect of carbon fiber surface functional groups on the mechanical properties of carbon–carbon composites with HTT”. In: *Carbon* 41 (6 2003). ISSN: 00086223. DOI: 10.1016/S0008-6223(03)00051-4.
- [8] W.J.D. Escher, E.H. Hyde, and D.M. Anderson. “A user’s primer for comparative assessments of all-rocket and rocket-based combined-cycle propulsion systems for advanced earth-to-orbit space transport applications”. In: *31st Joint Propulsion Conference and Exhibit* 95 (2474 1995), pp. 22–22.
- [9] J. Etele, S. Hasegawa, and S. Ueda. “Experimental Investigation of an Alternative Rocket Configuration for Rocket-Based Combined Cycle Engines”. In: *Journal of Propulsion and Power* 30 (4 July 2014), pp. 944–951. ISSN: 0748-4658. DOI: 10.2514/1.B35080. URL: <http://arc.aiaa.org/doi/10.2514/1.B35080>.
- [10] Kevin W. Flaherty, Katherine M. Andrews, and Glenn W. Liston. “Operability Benefits of Airbreathing Hypersonic Propulsion for Flexible Access to Space”. In: *Journal of Spacecraft and Rockets* 47 (2 Mar. 2010), pp. 280–287. ISSN: 0022-4650. DOI: 10.2514/1.43750. URL: <https://arc.aiaa.org/doi/10.2514/1.43750>.
- [11] Herwig Hosaeus et al. “Thermophysical properties of solid and liquid Inconel 718 alloy”. In: *High Temperatures-High Pressures* 33 (4 2001). ISSN: 0018-1544. DOI: 10.1068/htwu340.
- [12] A. R. Howell and R. P. Bonham. “Overall and Stage Characteristics of Axial-flow Compressors”. In: *Proceedings of the Institution of Mechanical Engineers* 163 (1 June 1950). ISSN: 0020-3483. DOI: 10.1243/PIME\_PROC\_1950\_163\_026\_02.
- [13] Harry Jones. “The recent large reduction in space launch cost”. In: 48th International Conference on Environmental Systems. 2018.
- [14] M. Koupriyanov and J. Etele. “Equivalence ratio and constriction effects on RBCC thrust augmentation”. In: *Acta Astronautica* 68 (11-12 June 2011), pp. 1839–1846. ISSN: 00945765. DOI: 10.1016/j.actaastro.2011.01.007. URL: <https://linkinghub.elsevier.com/retrieve/pii/S009457651100018X>.
- [15] G. Masuya, N. Chinzei, and S. Ishii. “A study of air breathing rockets—Subsonic mode combustion”. In: *Acta Astronautica* 8 (5-6 May 1981), pp. 643–661. ISSN: 00945765. DOI: 10.1016/0094-5765(81)90110-7. URL: <https://linkinghub.elsevier.com/retrieve/pii/0094576581901107>.
- [16] The MathWorks. *MATLAB*. Version R2020a. URL: <https://nl.mathworks.com/>.
- [17] *NIST Chemistry WebBook*. DOI: 10.18434/T4D303. URL: <https://webbook.nist.gov/>.

- [18] John R. Olds and John E. Bradford. "SCCREAM: A Conceptual Rocket-Based Combined-Cycle Engine Performance Analysis Tool". In: *Journal of Propulsion and Power* 17 (2 Mar. 2001), pp. 333–339. ISSN: 0748-4658. DOI: 10.2514/2.5746. URL: <https://arc.aiaa.org/doi/10.2514/2.5746>.
- [19] Mauro de Oliveira et al. "Mechanical Behavior of Inconel 625 at Elevated Temperatures". In: *Metals* 9 (3 Mar. 2019). ISSN: 2075-4701. DOI: 10.3390/met9030301.
- [20] *PBS Aerospace website*. URL: <https://www.pbsaerospace.com/>.
- [21] Alexander Ponomarenko. *Rocket Propulsion Analysis*. Version 2.3.2. URL: <https://www.rocket-propulsion.com/>.
- [22] R. Russell, Douglas Brocco, and Russell Daines. "Modeling and validation of an ejector primary rocket for shielded afterburning fuel injection". In: June 1999. DOI: 10.2514/6.1999-2241. URL: <http://arc.aiaa.org/doi/10.2514/6.1999-2241>.
- [23] Lei Shi et al. "Research progress on ejector mode of rocket-based combined-cycle engines". In: *Progress in Aerospace Sciences* 107 (May 2019), pp. 30–62. ISSN: 03760421. DOI: 10.1016/j.paerosci.2019.03.003. URL: <https://linkinghub.elsevier.com/retrieve/pii/S0376042118301921>.
- [24] A Siebenhaar and M Bulman. "The Strutjet engine - The overlooked option for space launch". In: July 1995. DOI: 10.2514/6.1995-3124. URL: <http://arc.aiaa.org/doi/10.2514/6.1995-3124>.
- [25] D.B. Spalding. "A new analytical expression for the drag of a flat plate valid for both the turbulent and laminar regimes". In: *International Journal of Heat and Mass Transfer* 5 (12 Dec. 1962). ISSN: 00179310. DOI: 10.1016/0017-9310(62)90189-8.
- [26] *Standard Atmosphere*. International Organization for Standardization, 1975. URL: <https://www.iso.org/standard/7472.html>.
- [27] Ralf Stark. "Flow Separation in Rocket Nozzles, a Simple Criteria". In: American Institute of Aeronautics and Astronautics, July 2005. ISBN: 978-1-62410-063-5. DOI: 10.2514/6.2005-3940.
- [28] Hai Wang et al. "A physics-based approach to modeling real-fuel combustion chemistry - I. Evidence from experiments, and thermodynamic, chemical kinetic and statistical considerations". In: *Combustion and Flame* 193 (July 2018). ISSN: 00102180. DOI: 10.1016/j.combustflame.2018.03.019.
- [29] George S. K. Wong and Tony F. W. Embleton. "Variation of specific heats and of specific heat ratio in air with humidity". In: *The Journal of the Acoustical Society of America* 76 (2 Aug. 1984). ISSN: 0001-4966. DOI: 10.1121/1.391597.
- [30] Rui Xue et al. "Experimental study on combustion modes of a liquid kerosene fueled RBCC combustor". In: *Fuel* 197 (June 2017), pp. 433–444. ISSN: 00162361. DOI: 10.1016/j.fuel.2017.02.044. URL: <https://linkinghub.elsevier.com/retrieve/pii/S0016236117301886>.
- [31] Qingchun Yang et al. "Maximum thrust for the rocket-ejector mode of the hydrogen fueled rocket-based combined cycle engine". In: *International Journal of Hydrogen Energy* 40 (9 Mar. 2015), pp. 3771–3776. ISSN: 03603199. DOI: 10.1016/j.ijhydene.2015.01.033. URL: <https://linkinghub.elsevier.com/retrieve/pii/S0360319915000701>.
- [32] Jianqiang Zhang, Zhenguo Wang, and Qinglian Li. "Thermodynamic efficiency analysis and cycle optimization of deeply precooled combined cycle engine in the air-breathing mode". In: *Acta Astronautica* 138 (Sept. 2017), pp. 394–406. ISSN: 00945765. DOI: 10.1016/j.actaastro.2017.06.011.